A Needle Positioning System for Percutaneous Procedures

by

Bryan Garth-Davis

Thesis presented in fulfilment of the requirements for the degree of Master of Science in the Faculty of Engineering at Stellenbosch University

Supervisors: Prof Cornie Scheffer
Prof Kristiaan Schreve

December 2012

Declaration

By submitting this thesis electronically, I declare that the entirety of the work contained therein is my own, original work, that I am the sole author thereof (save to the extent explicitly otherwise stated), that reproduction and publication thereof by Stellenbosch University will not infringe any third party rights and that I have not previously in its entirety or in part submitted it for obtaining any qualification.

Date: ....

Abstract

A Needle Positioning System for Percutaneous Procedures

B. Garth-Davis

Department of Mechanical and Mechatronics Engineering,
University of Stellenbosch,
Private Bag X1, Matieland 7602, South Africa.

Thesis: MScEng (Mechatronic)

December 2012

In percutaneous procedures, where the surgeon inserts a needle into a target in the patient, it is challenging to access the target at the first attempt. Repeated needle insertion attempts are highly undesirable, as they lead to increased theatre time, patient haemorrhage and radiation exposure. The proposal of this thesis was to develop a low-cost system to aid surgeons with the process of positioning and orientating the needle prior to insertion. The proposed system uses a stereo pair of images produced by a standard C-arm fluoroscope. By applying computer vision techniques, such as triangulation, the desired needle position and orientation are determined from the set of images. An articulated manipulator is used to position and orientate the needle. The surgeon makes selections on the images, via a graphical user interface (GUI), to indicate the desired position and orientation of the needle. Following these selections, an algorithm determines the necessary angles for the manipulator. The surgeon then positions the manipulator accordingly.

Results from tests on a phantom showed the system to be repeatable and accurate to 2 mm. This is less accurate than similar, existing systems which, reported accuracies of 0.25 and 1.21 mm. However, 2 mm accuracy is considered adequate as it allows a range of percutaneous procedures to be performed such as needle biopsy, regional anaesthesia, brachytherapy and percutaneous nephrolithotomy (PCNL). Tests on both a phantom kidney and a porcine kidney indicated that the system can function in a real percutaneous procedure and with an anatomical target. The total cost to develop the prototype system was R15 000.

The accuracy of the proposed system and the time to gain access to the target indicate that the system can be a beneficial aid to surgeons when performing percutaneous procedures. As minimal X-ray imaging is required, patients will also be spared excessive radiation exposure and theatre time.

Uittreksel

’n Naald Posisiebepalingstelsel vir Percutane Prosedures

(“A Needle Positioning System for Percutaneous Procedures”)

B. Garth-Davis
Departement Meganiese en Megatroniese Ingenieurswese,
Universiteit van Stellenbosch,
Privaatsak X1, Matieland 7602, Suid Afrika.

Tesis: MScIng (Megatroniese)
Desember 2012

In perkutane prosedures, waar die chirurg ’n naald in ’n teiken op die pasiënt invoeg, is dit moeilik om met die eerste probeerslag toegang tot die teiken te bekom. Herhaalde pogings om die naald in te voeg is hoogs ongewens, aangesien dit tot verlengde teatertyd, bloeding by pasinte sowel as stralingsblootstelling lei. ’n Laekostestelsel is ontwikkel om chirurge by te staan met die proses om die naald voor invoeging te plaas en te oriënteer. Die stelsel gebruik ’n paar stereobeelde wat deur ’n standaard-C-arm-fluoroskoop voortgebring word. Met behulp van rekenaarsigtegnieke, soos triangulasie, word die gewenste naaldposisie en -oriëntasie uit die stel beelde bepaal. ’n Geartikuleerde manipuleerder word gebruik om die naald te plaas en te oriënteer. Die chirurg voer die vereiste invoerdata deur middel van ’n grafiese gebruikerskoppelvlak (GGK) in, waarna ’n algoritme die vereiste hoeke vir die manipuleerder bepaal. Die chirurg plaas dan die manipuleerder dienooreenkomstig.

Die resultate van toetse op ’n fantoom toon dat die stelsel herhaalbaar en tot op 2 mm akkuraat is. Dit is minder akkuraat as soortgelyke, bestaande stelsels, wat ’n akkuraatheid van 0.25 mm en 1.21 mm onderskeidelik aangemeld het. Tog kan akkuraatheid van 2 mm as voldoende beskou word, aangesien dit ’n verskeidenheid perkutane prosedures moontlik maak, soos naaldbiopsies, regionale anestesie, bragiterapie en perkutane nefrolitotomie (PCNL). Toetse op ’n fantoomnier dui daarop dat die stelsel wél in ’n werklike perkutane prosedure kan funksioneer. Toetse op ’n varknier toon dat die stelsel wél ook met ’n anatomiese teiken kan werk. Die totale koste om die prototipe te ontwikkel was R15 000.

Die akkuraatheid van die voorgestelde stelsel en die tydsduur om toegang tot die teiken te bekom, dui daarop dat die stelsel ’n nuttige hulpmiddel kan wees vir chirurge wat perkutane prosedures uitvoer. Aangesien minimale X-straalbeelding vereis word, sal dit pasiënte ook oormatige stralingsblootstelling en verlengde teatertyd spaar.

Dedications

This thesis is dedicated to my parents, Cheryl and Clive.

Acknowledgements

I would like to express my sincere gratitude to the following people:

- My parents, Cheryl and Clive Garth-Davis, for all their love and encouragement over the course of my studies.
- Robyn Garth-Davis, my sister, for all her support through the tough times.
- Prof. Cornie Scheffer, my supervisor, for his calm demeanour, patience and guidance throughout the thesis.
- Prof. Kristiaan Schreve, my co-supervisor, for all his sound advice, insights and guidance throughout the thesis.
- Dr. Amir Zarrabi of Tygerberg Hospital's Urology Department for his valuable input and help in particular during the testing process.
- Ferdi Zietsman and Graham Hamerse of the Mechanical & Mechatronics Department's workshop for all their advice and for manufacturing the mechanical parts.
- Cobus Zietsman of the Mechanical & Mechatronics Department's workshop for all his insights.
- Welma Liebenberg and Marilie Oberholzer of the Mechanical & Mechatronics Department for their incredible patience with all things admin related.
- My fellow BERG colleagues, it has been so much fun and I could not have made it through without all the office banter.

Contents

Declaration **i**

Abstract **ii**

Uittreksel **iv**

Dedications **vi**

Acknowledgements **vii**

Contents **viii**

List of Figures **x**

List of Tables **xiii**

Nomenclature **xiv**

1 Introduction **1**
- 1.1 Background 1
- 1.2 Objectives 1
- 1.3 Motivation 2
- 1.4 Thesis Overview 2

2 Literature Review **4**
- 2.1 Percutaneous Procedures 4
- 2.2 Imaging Devices 9
- 2.3 Targeting and Needle Guidance 12
- 2.4 Robotics in Minimally Invasive Procedures 12
- 2.5 Concluding Remarks 19

3 Multiple View Geometry and Image Processing **20**
- 3.1 Computer Vision Theory 20
- 3.2 Camera Model and the Camera Projection Matrix 24
- 3.3 Multiple View Geometry 29

4 System Design 32
4.1 Overview and Operating Process 32
4.2 Specifications 34
4.3 Subsystems 35

5 Needle Position and Orientation Computations 48
5.1 Defining a Target 48
5.2 Coordinate Systems 49
5.3 Determining Needle-Positioning Device Angles 53

6 Software: Vision Application 58
6.1 Calibration Procedure 58
6.2 Targeting Procedure 63

7 Testing and Results 66
7.1 Theatre Room Setup and Testing Procedure 66
7.2 Phantom Tests 67
7.3 Porcine Kidney Tests 74
7.4 Error Propagation 75

8 Conclusions and Recommendations 79
8.1 Thesis Objective and Outcomes 79
8.2 Recommendations 80
8.3 Conclusions 81

Appendices 82

A Singular Value Decomposition (SVD) 83

B Design Calculations 84
B.1 Link Lengths and Angle Ranges 84
B.2 Bending Calculation 86
B.3 Denavit-Hartenberg Convention 88

C Electronics 91

D Complete Results Tables 93

List of References 97

List of Figures

2.1 Surgeon inserting the needle (left) and inserted the guide-wire through the needle (right). 6
2.2 Drawing of a kidney showing stone positions. 6
2.3 The balloon dilator inserted (left) and the sheath inserted over the dilator (right). 7
2.4 Cryoablation procedure for prostate cancer. 8
2.5 Fluoroscopy images showing the needle inserted in the vertebral body (A) and then the deposition of the PMMA cement (B,C). . . 8
2.6 Modern C-arm fluoroscopy device, with viewing screen on the left, and C-arm fluoroscope consisting of X-ray source and receiving screen on the right. 10
2.7 A fluoroscopic image taken prior to needle insertion, showing a virtual needle (pink) whose position is updated in real time with accordance to the actual needle's position as the procedure continues. 13
2.8 The Da Vinci master-slave robotic surgery system. Clockwise from top left: Robotic arms, surgeons console with viewing booth, end-effectors, surgeon's hand controls. 14
2.9 Three DLR MIRO arms with a model used to mimic heart surgery procedures. 15
2.10 MARS (MiniAture Robot for Surgical procedures) positioned next to a pen, *left*, and mounted onto a femur bone, *right*. 15
2.11 A graphic showing the intersection of the two laser planes in a line, used to orientate the needle. 16
2.12 CAD model of the TRUS and parallel robot needle guide. 17
2.13 Photograph of the parallel needle guidance robot inserting a needle into a phantom. 17
2.14 Operator controlling the robotic arms, with images from the endoscope and MR unit as guidance. 18
2.15 MR images on the master control screen. 18

3.1 Pinhole camera model geometry, showing the camera centre (C), image plane and principal axis. 25
3.2 An example of S-curve distortion, where a grid of points forms a distinctive "S" shape. 27

3.3 An image of a square with no radial distortion (left), an image of the same square with pincushion distortion (centre) and with fishbowl distortion (right). 28
3.4 Epipolar Geometry 30

4.1 A schematic showing the calibration process 33
4.2 A schematic showing the targeting process 33
4.3 Photo of the *Philips BV Pulsera* showing the X-ray tank (XT) and the image intensifier (II) 36
4.4 The degrees-of-freedom of the *BV Pulsera* 37
4.5 Schematic used to determine the overall dimensions of the calibration object 38
4.6 Computer Aided Design (CAD) model of the calibration object showing the three levels, metal markers and dowel pins 38
4.7 CAD model of the calibration object showing the distinct lines formed by the metallic markers, 0° position left, 20° position right . 39
4.8 Photograph of the calibration object 39
4.9 Schematic showing the concept of the cartesian manipulator 40
4.10 Photograph of the needle-positioning device developed by *Conradie* which was based on the cartesian manipulator concept 41
4.11 Schematic showing the concept of the articulated manipulator . . . 41
4.12 CAD model of the needle-positioning device showing the essential components 44
4.13 Two views of a CAD model of the base and its associated components 44
4.14 Exploded view of a link and its associated components (left) and assembled view (right) with the succeeding link included 45
4.15 CAD model of the wrist and its associated components 46
4.16 Photograph of the assembled needle-positioning device attached to a typical operating theatre bed 46

5.1 0° (left) and 20° (right) C-arm fluoroscopy images of test target object, two metal washers, with operator's selection points 49
5.2 The world coordinate system, derived from the calibration object . 50
5.3 The wrist coordinate system, attached to the wrist 50
5.4 Lines formed from the two pairs of metal spheres, the intersection of the lines is the wrist gyro-centre 51
5.5 CAD model showing vertical offset (v) of one pair of metal spheres and the rotation necessary to align x' with the x axis of the wrist . 51
5.6 Base coordinate system 52
5.7 Diagram illustrating the extra rotation, θ_6, about the x^d_{wrist} axis . . 53
5.8 Projection of the gyro-center onto the x_{base}-y_{base} plane 54
5.9 Projection of the gyro-center onto the x_{base}-y_{base} plane 55

6.1 Screen shot of the GUI following the selection of the calibration object images . . . 59
6.2 Procedures for locating the metal sphere centres . . . 61
6.3 Plot showing the original markers and the corrected markers . . . 62
6.4 Screen shot of the GUI after a successful calibration . . . 63
6.5 GUI screen shot of the targeting procedure once the user has opened the target images and made the necessary selections . . . 64
6.6 GUI screen shot of the targeting procedure once the user has entered and submitted the initial angles of the gantry . . . 65
6.7 GUI screen shot of the targeting procedure displaying the target joint angles . . . 65

7.1 Photograph of the theatre room testing setup showing the essential components . . . 67
7.2 Operating process map . . . 68
7.3 CAD model (left) and photograph of phantom 1 used as a test object 69
7.4 Bar charts showing the average calibration errors (top) and average triangulation errors (bottom) for cameras 1 and 2 . . . 71
7.5 The five different phantom positions with respect to the calibration object (border shown) . . . 72
7.6 Photographs of phantom 2 (left) and the analogue kidney (right) showing the three calyces . . . 74
7.7 Photograph of a successful needle insertion in phantom 2 . . . 75
7.8 Photograph the porcine kidney inside the phantom abdomen . . . 75
7.9 C-arm produced image of the porcine kidney and wrist with labels added . . . 76
7.10 C-arm produced image showing the needle inserting the target calyx 76
7.11 Photograph of the needle inserting the porcine kidney . . . 77

B.1 A schematic showing the error in needle position resulting from an error in the potentiometer reading of joint 3 . . . 84
B.2 A schematic showing the error in needle position resulting from an error in the potentiometer reading in joint 2 . . . 85
B.3 A plot of the work-volume of the needle-positioning device (the first three arms shown in red), with the first joint held still. The work volume is shown in black whilst the desired volume is blue. . . . 86
B.4 Coordinate frames attached to the needle positioning-device . . . 88

C.1 A schematic of the components making up the electronics of the system . . . 91
C.2 Photograph of the LCD displaying the joint angles . . . 92

List of Tables

2.1 Comparisons of the common imaging modalities. 11

4.1 List of initial needs and the corresponding specification(s) resulting from their assessment 34
4.2 Comparison of cartesian and articulated manipulators. 42
4.3 Link lengths and joint ranges of the final design 43

5.1 DH parameters of the needle-positioning device 56

7.1 Results of the first repeatability test 69
7.2 Results of the second repeatability test 70
7.3 Results of the third repeatability test 70
7.4 Results of the second set of repeatability tests 72
7.5 Results of the accuracy tests 73

B.1 Link lengths and joint ranges of the final design 86
B.2 Values used for the bending calculations 87
B.3 Boundary conditions for link 2, $x = 0$ 87
B.4 DH parameters of the needle-positioning device 90

D.1 Results of the first repeatability test 93
D.2 Results of the second repeatability test 94
D.3 Results of the third repeatability test 94
D.4 Results of the second set of repeatability tests 95
D.5 Results of the accuracy tests 95

Nomenclature

Symbols

$\mathbf{C}$	World coordinate origin in Pinhole Camera model
d_i	Link i offset (mm)
E	Modulus of elasticity
e	Epipole point
F	Fundamental matrix
f	Camera focal length (Pinhole Camera model)
H	Projective transformation matrix (2D to 2D case)
I	Second moment of area (m^4)
k_1	First distortion coefficient of distortion model
k_2	Second distortion coefficient of distortion model
K	Matrix containing the intrinsic parameters of the camera
l_1	Link 1 length (mm)
l_2	Link 2 length (mm)
l_3	Link 3 length (mm)
p	Principle point on the image plane (Pinhole Camera model)
P	Projective transformation matrix (3D to 2D case)
$\mathbb{P}^2$	2-Dimensional projective space
$\mathbb{P}^3$	3-Dimensional projective space
$\mathbb{P}^n$	n-Dimensional projective space
R	Matrix representing orientation of camera frame in world frame
$\mathbb{R}^2$	2-Dimensional Euclidean space
$\mathbb{R}^n$	n-Dimensional Euclidean space
α_i	Link i twist (°)
θ_1	Joint 1 angle (°)
θ_2	Joint 2 angle (°)
θ_3	Joint 3 angle (°)
θ_4	Joint 4 angle (°)
θ_5	Joint 5 angle (°)

π	Epipolar plane

Acronyms

CAD	Computer Aided Design
CCD	Charge-coupled Device
CT	computed tomography
DLT	Direct Linear Transformation
GUI	Graphical User Interface
LCD	Liquid Crystal Display
MARS	MiniAture Robot for Surgical procedures
MRI	magnetic resonance imaging
PAKY	percutaneous access to the kidney
PCNL	percutaneous nephrolithotomy
SVD	Singular Value Decomposition
TRUS	transrectal ultrasound

Glossary

Angiographic X-ray examination of blood vessels following injection of a radiopaque substance.

Lithotriptor A device used to break down kidney stones to a size able to be passed out in the urine.

Patency In medicine, the condition of not being blocked or obstructed.

Percutaneous Through the unbroken skin.

Radiolucent Almost entirely invisible in x-ray photographs and under fluoroscopy.

Chapter 1

Introduction

1.1 Background

An increasing number of medical ailments are being treated in a minimally invasive manner. Many of the procedures involved may be categorised as percutaneous, whereby a needle is inserted through the patient's skin to the target area. The surgeon then has access to the target area following which various tools and techniques may be introduced depending on the operation. Examples are needle biopsy, regional anaesthesia, brachytherapy, percutaneous nephrolithotomy (PCNL), cryoablation and vertebroplasty. Medical imaging techniques are essential to minimally invasive procedures as they are the means by which the surgeon sees the target area and inside the patient whilst operating. Many of these procedures require expensive imaging systems and in some cases additional surgical navigation equipment. Current techniques for reaching the target area with the needle often lead to haemorrhage and increased theatre time due to too many unsuccessful attempts.

1.2 Objectives

The main objective of this thesis is to develop a system to aid surgeons in performing percutaneous procedures, in particular, the initial step of positioning and orientating the needle in the desired manner such that it will reach the target area. The system must use a standard C-arm fluoroscopy imaging device, which is relatively inexpensive and readily available in the operating room. The system developed is thus limited to procedures able to be undertaken using fluoroscopic imaging. A device capable of positioning and orientating a needle in three dimensional space is to be developed, allowing the surgeon to accurately insert the needle. Stereo vision theory is to be applied to a set of stereo fluoroscopy images so as to determine the required needle position and orientation.

The device is to be tested by performing PCNL, a kidney stone removal technique. PCNL is widely considered the best technique for eradicating large, staghorn or other complex renal stones. The needle is to be positioned and orientated as desired by the surgeon when observing the stereo image pair. As the target, the kidney calyx containing the stone, is typically of 10 mm in diameter or larger, a needle placement accuracy of 5 mm is considered sufficient for a successful operation. Needle deflection and kidney movement whilst the needle is inserted are not considered.

1.3 Motivation

There is currently no inexpensive system to aid surgeons in percutaneous procedures. There is a need for such a system in South Africa as the only options available are highly sophisticated and very expensive equipment. A more elementary, low cost system, whilst still having a high success rate of the needle reaching the target, is desired [1]. With each new needle insertion attempt, the patient suffers further haemorrhage to the tissue and blood vessels in the vicinity of the target area. In some cases, the haemorrhage can reach such an extent that the surgeon is forced to abort the procedure. The success of the techniques used by surgeons when performing percutaneous procedures by fluoroscopic imaging, are highly dependent on the experience of the surgeon. New insertion attempts are most likely accompanied by further imaging, resulting in increased radiation exposure to the patient and the rest of the operating team. Repeated needle insertions ultimately detract from the characteristics of minimally invasive procedures which make them so favourable. Increased operating time leads to more patient expense and recovery time. A means by which surgeons can accurately and efficiently gain access to the target is thus highly desirable.

1.4 Thesis Overview

Chapter 2 presents a review of the literature with an emphasis on percutaneous procedures and robotics in surgery. Chapter 3 discusses the computer vision theory implemented in the thesis and the camera model used to describe the C-arm fluoroscope. This is followed by Chapter 4 which details the system design, such as the operating process, C-arm fluoroscope and mechanical components. The computations necessary to determine the parameters of the needle-positioning device, to position and orientate the needle as desired, are discussed in Chapter 5. Chapter 6 presents the software system and how the Graphical User Interface (GUI) in particular is used to provide inputs such as the raw C-arm images and surgeon target selections. The results of the system testing are detailed in Chapter 7. Finally, the thesis conclusions and recommendations are given in Chapter 8.

Chapter 2

Literature Review

A review of the literature was performed with attention to common minimally invasive procedures in medicine, modern imaging modalities and robotics in surgery. With regard to the minimally invasive procedures, the focus was on procedures involving the positioning and insertion of a needle into the patient, known as percutaneous procedures. The four most common modern imaging modalities, namely fluoroscopy, computed tomography, magnetic resonance imaging and ultrasound were reviewed, with particular attention to fluoroscopy and ultrasound as these two are considered most relevant to this thesis. Robotics in surgery involving the positioning of a needle, were of most concern.

2.1 Percutaneous Procedures

There are currently many medical procedures that are percutaneous in nature. Minimally invasive procedures are preferred over invasive or "open" surgeries. The small incision made to gain access to the desired internal region, results in reduced trauma, improved prognosis and considerably less patient recovery time [2]. With the rapid increase in medical imaging technologies and surgical instrumentation, an increasing amount of ailments previously operated on in an invasive manner may be treated by a minimally invasive technique.

Some common percutaneous procedures are discussed here, including a brief summary of the steps involved in the procedure. As this thesis is concerned with needle positioning, the discussion will not consider in great detail what occurs in the procedure after the needle has been placed. Some remarks and conclusions follow the various percutaneous procedures reviewed.

2.1.1 Needle Biopsy

Needle biopsy is a percutaneous procedure whereby a needle is inserted into the patient's body and tissue or cells are withdrawn for examination, after which a diagnosis may be made. Such a procedure is commonplace in medicine and is a valuable technique of diagnosis. A needle biopsy is frequently performed in the diagnosing and staging of various forms of cancer [3–6]. In recent years it has also become an important procedure in the investigation of muscle morphology, physiology and pathology [7]. In general, these procedures involve a form of pre-operative imaging, whereby the doctor may decide upon an entry point and needle entry angle so as to reach the desired region of diagnosis. Most of the procedures are also performed under image guidance whilst the needle is being inserted. For cancer diagnosis, the co-axial technique is preferred by radiologists. This technique comprises of the radiologist firstly inserting a thin-walled guide needle, through which a needle may be inserted multiple times to extract samples of the desired tissue [3].

2.1.2 Regional Anaesthesia

Regional anaesthesia is the anaesthetising of a region of the body such as an organ. Performing regional anaesthesia involves firstly identifying the target nerve using an imaging technique, inserting the needle under image guidance as close to the nerve as possible without making contact, and then surrounding the nerve with anaesthetic [8]. Administering regional anaesthesia is an important procedure as in many cases it is preferred over general anaesthesia. This is particularly true in the case of trauma patients, because the patient is awake and protective airway reflexes are unimpaired, there is less hospital time, a reduction in postoperative bleeding and reduction in postoperative pain scores [9].

2.1.3 Brachytherapy

Brachytherapy is a type of radiation therapy whereby a radioactive source (commonly referred to as a “seed”) is placed in or near the tumour to be eradicated. It is most commonly used to treat breast, cervical, prostate and skin cancers [10–13]. For cancer in certain areas, notably the prostate, imaging is essential to locate the target area and determine a safe route to reach this area so the seeds may be successfully placed [14]. Once the target area has been located, a needle is positioned and inserted into the patient up until this area. This part of the procedure is also usually performed under image guidance. The seeds are then deposited to the target area via the needle [12].

An advantage of brachytherapy is the structures close to the tumour are not subjected to high radiation. This is due to the rapid decline of radiation strength around the seeds. Another advantage is the reduction of tumour re-population as a result of the short overall treatment duration [15].

2.1.4 Percutaneous Nephrolithotomy (PCNL)

PCNL is a commonly performed minimally-invasive technique used to remove renal calculi, more commonly known as kidney stones. The procedure, as described by *Miller* et al., is summarised as follows [16]: Imaging techniques are used to locate the kidney stone and determine a suitable route from the skin to the stone. A needle is inserted and advanced into the patient with the aid of image guidance. A guide-wire is then inserted down the needle and a fascial dilator is inserted (see Figure 2.1) into the calyx (opening which collects urine, were the kidney stone resides (see Figure 2.2)).

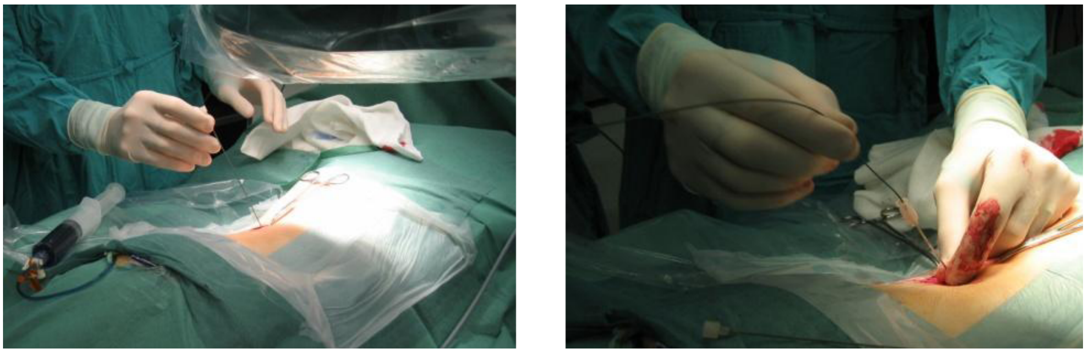

Figure 2.1: Surgeon inserting the needle (left) and inserted the guide-wire through the needle (right) [17].

Following this, an angiographic catheter is inserted to help direct the guide-wire down the ureter (the tube leading from the kidney to the bladder, see Figure 2.2). A small incision is now made in the skin at the entry point to allow for a balloon dilator to be inserted and dilated.

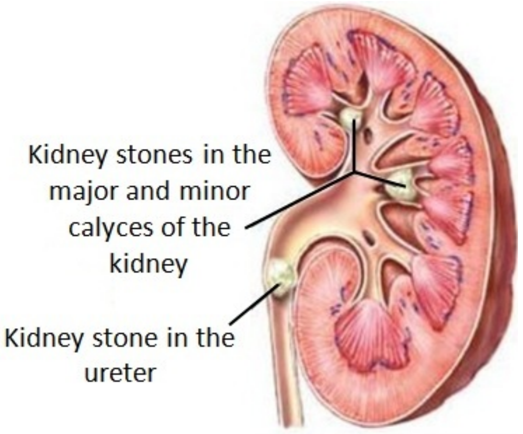

Figure 2.2: Drawing of a kidney showing stone positions [17].

Finally a sheath is advanced over the dilated balloon and the balloon is removed, leaving the surgeon with a clear route to the kidney and renal calculi (see Figure 2.3). The surgeon may then use any of the various types of lithotripters that exist to break the calculi into small fragments which may be removed.

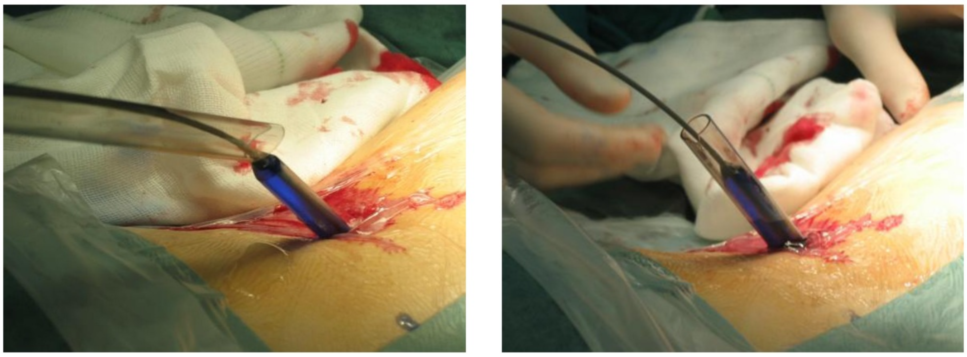

Figure 2.3: The balloon dilator inserted (left) and the sheath inserted over the dilator (right) [17].

2.1.5 Cryoablation

Cryoablation is a method of destroying tissue by freezing. It is used to treat a wide variety of cancers, most commonly in the liver, kidney, lung, prostate and breast [18]. Other ablation techniques exist that are also percutaneous in nature, such as chemical ablation and using heat instead of cold to ablate the tumour [19], however only cryoablation will be discussed here as the other ablation techniques are in principle the same.

Once the tumour has been targeted using one of the many imaging modalities available, a thin hollow needle called a cryoprobe is inserted through the patient's skin into the tumour. The cryoprobe is a specially designed needle that is closed at the end with a small chamber at the tip where the cooling takes place. Argon gas is then forced through the cryoprobe at high pressure. The gas passes through a throttle near the end of the needle and upon exit into the chamber rapidly expands to atmospheric pressure. This rapid expansion of the gas causes a decrease in temperature of the gas and consequently heat is removed from the tissue at the tip of the needle [18; 19]. Occasionally multiple needles are used for larger tumours (see Figure 2.4).

2.1.6 Vertebroplasty

Also known as cementoplasty, vertebroplasty is the procedure whereby acrylic bone cement is injected via a needle into a vertebral body. This procedure is typically done to relieve the pain caused by vertebral compression fractures.

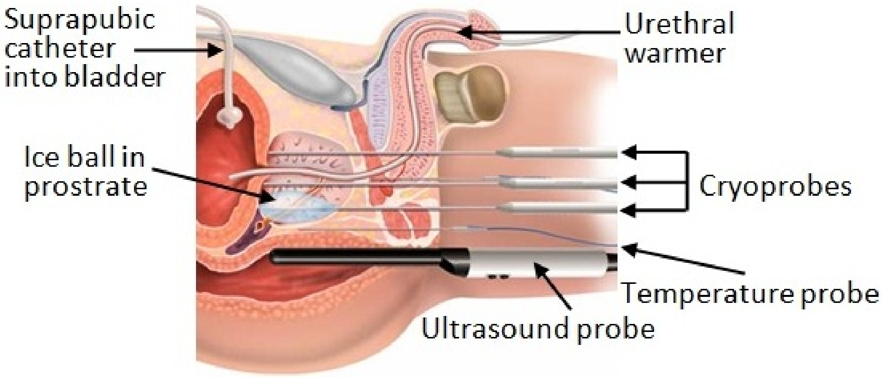

Figure 2.4: Cryoablation procedure for prostate cancer. Here ultrasound is used to monitor the ice ball formation. The urethral warming catheter warms the urethra to minimize injury, whilst the suprapubic tube drains the bladder as the prostate swells after the procedure [20].

Eckel and Olan describe the vertebroplasty procedure with the use of a C-arm fluoroscopy imaging modality, which may be summarised as follows [21]: The C-arm fluoroscopy imaging device is used to determine a suitable approach to the target area for the deposition of the cement via a needle (usually 10-, 11-, and 13-gauge bone access needles are used). The approach is determined so as to allow the needle tip to end as close as possible to the target site whilst avoiding critical structures (nerve roots, blood vessels, arteries). After a local anaesthetic and concious sedation agents are administered to the patient, the needle may be inserted into the patient under the guidance of the fluoroscopy device.

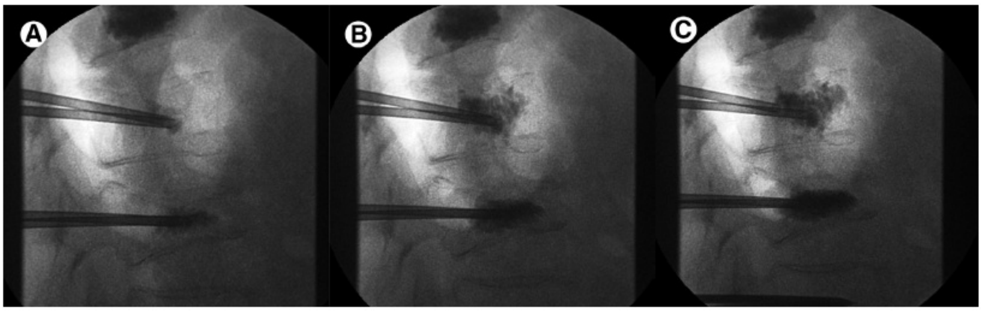

Figure 2.5: Fluoroscopy images showing the needle inserted in the vertebral body (A) and then the deposition of the PMMA cement (B,C) [21].

The target site is the anterior third and center of the vertebral body in the weight-bearing portion. This is where the cement (usually polymethylmethacrylate, PMMA) may be deposited (see Figure 2.5), which upon hardening within one to two hours, will relieve the patient of pain in a successful procedure.

2.1.7 Remarks

It is not within the scope of this literature review to describe in great detail the many percutaneous procedures in medicine. Hence, only a few of the more common minimally invasive procedures have been discussed. It is observed that whilst these procedures may differ considerably in the ailments intended to be treated by the procedure and also the region of the body operated on, there are common steps in the operations which are of most concern to this thesis. These commonalities in particular are the initial imaging of the target region, so as to determine a suitable route for the needle to pass from the surface of the patient to the target region, and the subsequent positioning and inserting of the needle, usually under image guidance.

Whilst some procedures use real time image-guidance while the needle is being inserted, image guidance prior to needle insertion is essential to all the procedures. Many imaging modalities exist to allow a route to the target region to be determined. Some are more suitable than others to a specific procedure whilst for some procedures any imaging modality may be used, usually decided by availability.

The various medical imaging modalities are now discussed.

2.2 Imaging Devices

Minimally invasive surgery developed slowly, until the advent of new technology, most notably imaging modalities, allowed an increasing number of procedures to be performed with minimal invasiveness [22]. Each imaging modality such as, fluoroscopy, magnetic resonance imaging (MRI), computed tomography (CT) and ultrasound, has its strengths which will dictate which procedure it is more suited to. Fluoroscopy and ultrasound are discussed in more detail while a general discussion is made regarding the remaining two modalities.

2.2.1 Fluoroscopy

Most percutaneous procedures are performed using fluoroscopy [23], whether it be used pre-operatively or intra-operatively. A fluoroscope consists of an X-ray source and a fluorescent screen between which the patient is placed. Most modern fluoroscopes are of the C-arm type, where the X-ray source is at the one end of the "C" and the detecting screen on the other (see Figure 2.6).

Photons originating from the X-ray source are of higher energy than visible light and are thus able to pass through the body. Some of the photons are absorbed by tissue in varying amounts, whilst the rest pass through the patient and react with the fluorescent screen to form an image. Some photons deviate from their original path, known as scattering, which blurs the image [25]. Fluoroscopy differs from conventional X-ray radiography in that it allows real-time imaging, so video can be recorded.

Figure 2.6: Modern C-arm fluoroscopy device, with viewing screen on the left, and C-arm fluoroscope consisting of X-ray source and receiving screen on the right [24].

Some of the advantages of fluoroscopy have been listed as high spatial resolution, good penetration of all tissues, low cost and its ability to guide procedures in real-time. Disadvantages have been cited as poor differentiation between soft tissue structures, two-dimensional imaging and most significantly radiation exposure to the patient [25]. When fluoroscopy is used pre-operatively, radiation exposure is low as two photos are taken of the target region and not videos. The two photos are taken from different positions to allow stereo vision principles to be used so three-dimensional data of the target region may be formed. Fluoroscopy is used in needle biopsies, such as diagnosing and staging of bone lesions [3], regional anaesthesia, although the inability to differentiate soft tissue structures can cause difficulties [26], PCNL, cryoablation [19] and vertebroplasty [21].

2.2.2 Ultrasound

As the name implies, ultrasound operates by high frequency acoustic waves. When the acoustic waves travel through the patient's body, they are partially reflected as they encounter a change in resistance to their travel, for example at the boundary between tissue structures. The waves are generated and received at the same location and thus waves that reflect may be detected. It is these changes in reflection that are interpreted as changes in internal structure and translated into images [25].

Ultrasound is the only modality that provides three-dimensional real-time images. Other advantages are: no radiation exposure, portability, low cost and wide availability. Some disadvantages are limited penetration (cannot image deep structures), needle visualisation difficulty and portable equipment usually lacks in resolution [26].

Ultrasound is used in needle biopsies for operations involving many different regions such as the liver, kidney, pancreas and spleen [3]. It is used for guidance in regional anaesthesia or nerve blocks [9]. Ultrasound has been cited as having limited roles in PCNL due to difficulties in gaining access to undilated collecting systems [27]. Ultrasound is often used intra-operatively for real-time guidance as it does not result in long time exposure of radiation to the patient. However ultrasound's limited field of view can cause the surgeon to become disorientated if anatomical details are unfamiliar or unrecognisable. When used intra-operatively to guide a procedure, visualization of the needle being inserted can be very difficult especially at deep locations in tissue [28]. This is because the needle behaves as a "perfect reflector" of the ultrasound waves, reflecting them parallel to the receiver, and so disperses the waves away from the receiving probe.

2.2.3 Magnetic Resonance Imaging (MRI) and Computed Tomography (CT)

Many of the procedures listed in Section 2.1 may use any of these two imaging modalities. However, MRI has been cited as having a limited role in PCNL due to unreliability at identifying renal calculi [29]. Some advantages of MRI are no radiation exposure, high resolution images, very good soft tissue images and the possibility of three-dimensional reconstruction. The main disadvantages are that real time imaging is not possible, no portability, high cost and it is a magnetic field hazard (no metallic objects) [26].

The advantages of CT are high resolution images, high detail of bone, solid tissue and air filled spaces, and three-dimensional reconstruction is possible. The disadvantages are high radiation exposure, no real time imaging, lower detail of soft tissue, no portability and high cost [26].

Table 2.1 summarises the comparisons between the common imaging modalities discussed.

Table 2.1: Comparisons of the common imaging modalities [25].

Modality	Spatial Resolution	Tissue penetration	Differentiate tissue boundaries
Fluoroscopy	++	++++ (complete)	++
CT	+++	++++ (complete)	+++
MRI	+++	++++ (complete)	++++
Ultrasound	+	+++ (no bone)	+++

2.3 Targeting and Needle Guidance

By imaging the target region multiple times from different angles, the surgeon can decide upon the needle entry trajectory. In general, the imaging device is set-up to look down the needle whilst it is being inserted. By moving the imaging device to show a view oblique to this one (e.g. rotating the C-arm fluoroscope), the surgeon can observe the depth of the needle. Case examples are given by [30] and [16] which discuss the PCNL procedure, in detail, under C-arm fluoroscopy guidance. Ultrasound may be used in a similar manner to guide percutaneous procedures, however there are set-backs to using ultrasound as discussed in Section 2.2.2.

Many devices have been developed to aid the surgeon in needle positioning and insertion. These devices are intended to help the surgeon reach the desired target region on the first attempt and in minimum time, thus reducing patient haemorrhage and radiation exposure. These devices are discussed in the following section.

2.4 Robotics in Minimally Invasive Procedures

Tools such as robots have been developed to help the surgeon with positioning the needle precisely before insertion. These tools also aid during needle insertion by performing functions such as determining the required insertion depth, providing haptic feedback and enhancing visual feedback so the surgeon can visualize the needle better during insertion (such as virtual reality technology). Examples of such systems incorporating these features and more are discussed in the following section.

2.4.1 Virtual Reality and Needle Position Feedback

Much can be found in the literature on means of aiding or improving image-guided needle insertion. *Glossop* et al. discuss a magnetic microsensor which is located at the tip of the needle and thus the position of the needle may be monitored on the imaging screen [31]. Upon reaching the target, the sensor can be removed so that the needle may be used for drug delivery or tissue sampling. Drawbacks of this device is that specialized needles are needed and sensor withdrawal adds steps to the procedure [32]. *Howard* et al. describe a similar device which is made up of electromagnetic sensors on both the probe and the needle [33]. Their system also provides an animation on the ultrasound image showing the expected needle trajectory.

These devices discussed may be described as virtual reality aided techniques in that the needle on the screen is presented as a graphic or animation. In some cases this may be used to highlight the needle already visible on the screen (for example in the case where needle visibility is difficult, such as when ultrasound is used as the imaging modality) or to display a graphic needle on a static image that was taken before the procedure began (e.g. the *FluoroNav*) (see Figure 2.7, where navigation software was used to aid a percutaneous spine procedure) [34].

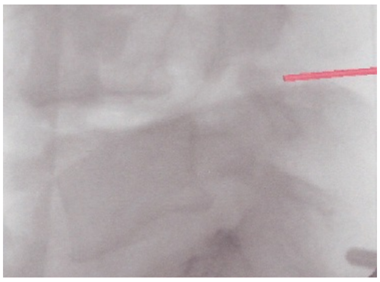

Figure 2.7: A fluoroscopic image taken prior to needle insertion, showing a virtual needle (pink) whose position is updated in real time with accordance to the actual needle's position as the procedure continues [34].

2.4.2 Robotic Devices

A review of the literature was performed for robotic devices in surgery, with a focus on those with applications in minimally invasive surgery.

Research and development into surgical robots began with the belief that higher speed and accuracy could be achieved in surgical procedures. This belief stemmed from the large success of industrial robots [35]. The first recorded surgical procedure to make use of a robot was a CT-guided brain biopsy at the Memorial Medical Center, CA, USA [35]. The procedure adapted an industrial robot, the *Unimation PUMA 200*, and was used to place a probe for the biopsy.

Robotics in surgery can generally be placed into two categories: *Telemanipulators*, also known as *master-slave* systems, and *image-guided* robotics [36]. Master-slave systems are completely controlled by the surgeon who operates the device by a set of controllers, e.g. joysticks, buttons, etc. The surgeon's movements are then mimicked by the robot. Image-guided systems are largely automated, in that following imaging and image processing of the target area, a computer determines relative coordinates and orientation for the robot's end-effector. The end-effector is then moved into this position either manually by the surgeon or by an automated control system.

A master-slave robotic system which is well established in percutaneous procedures is the *Da Vinci* system. The system consists of four robotic arms (possessing six degrees of freedom) with various end-effectors available, a single or double surgeon's console and a visualization system [36]. The surgeon's movements are translated into scaled down movements of the robotic arms and end-effectors, with tremors in the surgeon's hand filtered. The surgeon operates seated at the console with a viewing screen providing a three-dimensional image of the operating area (see Figure 2.8).

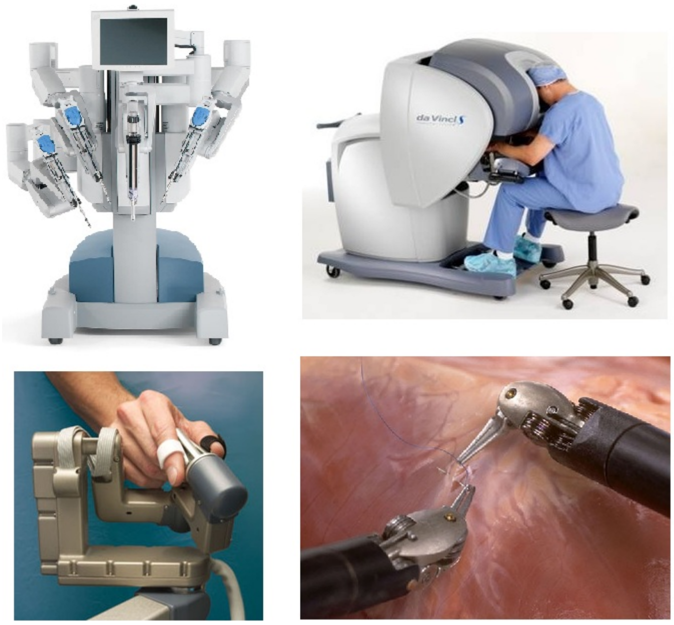

Figure 2.8: The Da Vinci master-slave robotic surgery system. Clockwise from top left: Robotic arms, surgeon's console with viewing booth, end-effectors, surgeon's hand controls [37].

Mohr et al. performed clinical studies with the *Da Vinci* system in 148 patients to minimize access to cardiac surgical procedures [38]. Different procedures were performed on fractions of the patients namely minimally invasive coronary bypass and total endoscopic coronary bypass, with postoperative patency rates of 96.3% and 95.4% respectively. Overall mortality in the group was recorded as 2.0% and was considered not related to the robotic system. *Mohr* et al. were generally satisfied with the *Da Vinci* but commented that tactile feedback would be very useful.

Hagn et al. developed a highly versatile robotic arm, the *DLR MIRO*, for surgical applications [39]. Their priorities in the design were that the device be compact, lightweight and versatile. The seven degrees of freedom device, has all the necessary electronics integrated into the arm (see Figure 2.9). In terms of versatility, the robotic arm can be adapted to different surgical procedures by adding specialized instruments or choosing between two robot control modes. The robot can either be controlled by the surgeon using a controller, or the robot can follow a preprogrammed trajectory to a specific point, such as that determined by image processing of the target region. However, no studies of the *DLR MIRO* in actual clinical procedures could be found.

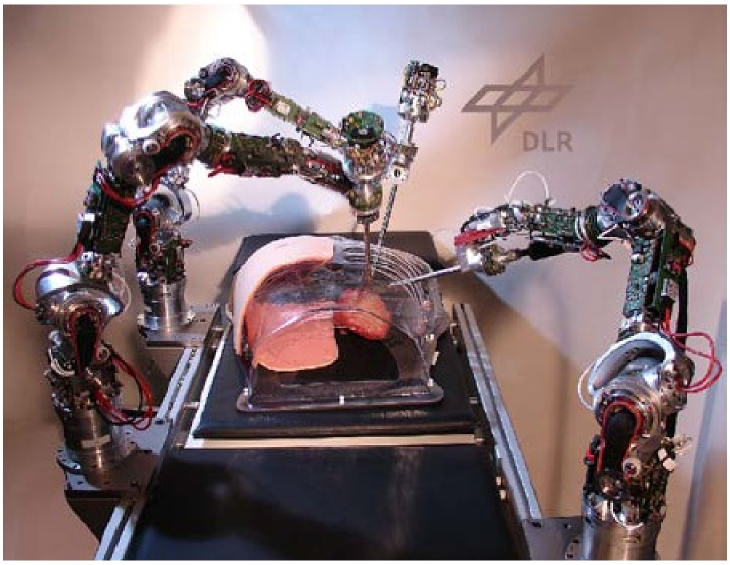

Figure 2.9: Three DLR MIRO arms with a model used to mimic heart surgery procedures [39].

An innovative device was introduced by *Shoham* et al. named *MARS* [40]. MARS is an acronym for MiniAture Robot for Surgical procedures, and is novel in that it mounts directly onto the patient's bony structure near the surgical site and provides support for drilling or needle targeting procedures. The device is essentially a miniature parallel manipulator of size $5 \times 5 \times 7$ cm^3, 200 g, with six degrees of freedom (see Figure 2.10). MARS makes use of C-arm fluoroscopy imaging and stereo vision principles of the target area to position the manipulator. The device is intended to support a variety of spinal procedures such as pedicle screw insertion and vertebroplasty.

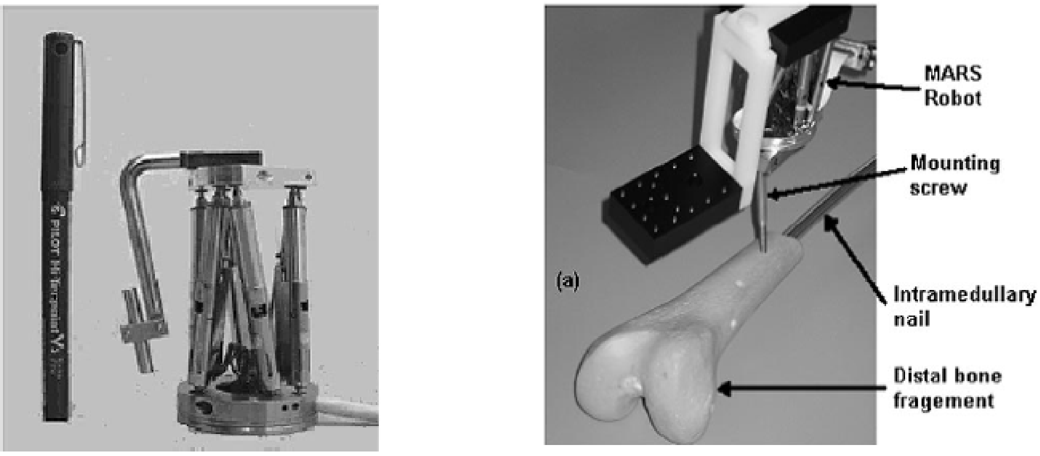

Figure 2.10: MARS (MiniAture Robot for Surgical procedures) positioned next to a pen, *left*, and mounted onto a femur bone, *right* [40].

A needle positioning device guided by lasers is described by *Liao* et al. [41]. An aspect of their system of particular interest is the means by which they align the needle in the correct orientation. Two lasers project laser planes onto mirrors which then reflect the laser planes onto the surgical area. Both the orientation of the laser emitters and the mirrors can be adjusted with motors. The two laser planes intersect as a line in space. A navigation system using information from stereoscopic images of the target area, adjusts the angles of the laser planes and mirrors such that the line in space goes through the target area from outside the patient in the desired orientation (see Figure 2.11). The needle is then aligned with this line and inserted into the patient.

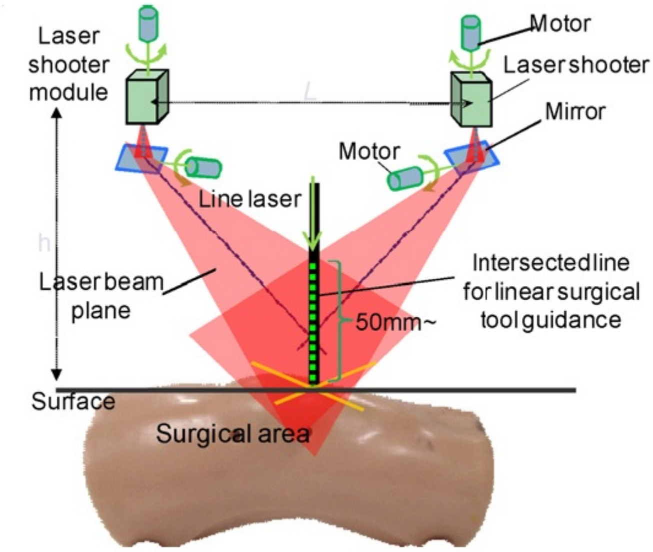

Figure 2.11: A graphic showing the intersection of the two laser planes in a line, used to orientate the needle [41].

Fichtinger et al. describe an ultrasound-guided robot for prostate brachytherapy [42]. The system, which is comprised of a transrectal ultrasound (TRUS) and a spatially co-registered robot (see Figure 2.12), and the associated treatment plan have been approved by the FDA. The robot is a parallel needle guidance robot which receives coordinates of the desired needle location from a PC, which has computed these coordinates from the TRUS. The surgeon then manually inserts the needle whilst observing its depth on the live TRUS.

The pre-insertion orientation of the needle was measured for transverse and rotational errors. *Fichtinger* et al. reported errors of 0.25 mm (standard deviation of 0.17 mm) and 0.75° (standard deviation of 0.37°) respectively. Needle tip placement errors in TRUS of 1.04 mm (standard deviation of 0.50 mm) were recorded in tests on phantoms. Figure 2.13 shows an example of a needle being inserted into a brachytherapy training phantom. Clinical tests were per-

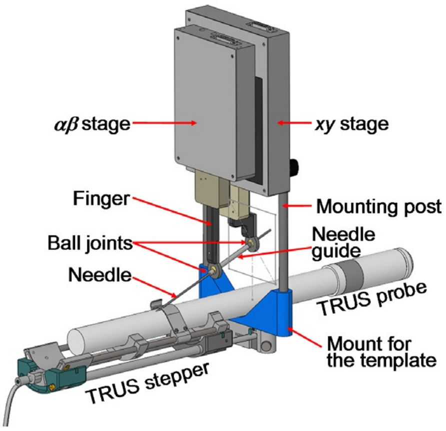

Figure 2.12: CAD model of the TRUS and parallel robot needle guide [42].

formed where needle tip positioning errors of a magnitude greater than 4 mm were found in only 2 of 179 guided needles.

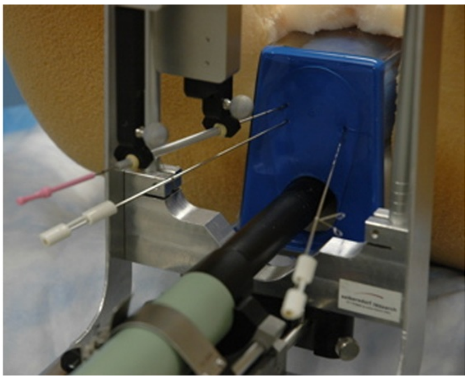

Figure 2.13: Photograph of the parallel needle guidance robot inserting a needle into a phantom [42].

Over the last decade there has been an increase in the development of MRI-compatible robots [43]. Researchers have desired to make use of the advantages of MRI technology in robot-assisted percutaneous procedures. The two main challenges in such devices are that they must be comprised of non-ferromagnetic materials only and be small enough to fit within the MR unit. *Hashizume* et al. have developed an MRI-compatible robot for minimally invasive surgery [44]. Their device is a master-slave type robotic system (see Figure 2.14) with seven degrees of freedom and is comprised of four arms; one holds the endoscope and the other three hold grips for surgical instruments. The slave manipulator system is fixed to a specialised MR-compatible operating table. The need for a specialised table is considered a drawback of the system.

Figure 2.14: Operator controlling the robotic arms, with images from the endoscope and MR unit as guidance [44].

The operator views both the images from the endoscope and those from the MR-unit to perform the procedure (see Figure 2.15). Tests were done on a phantom with a 2 cm diameter target, which was successfully punctured on all attempts.

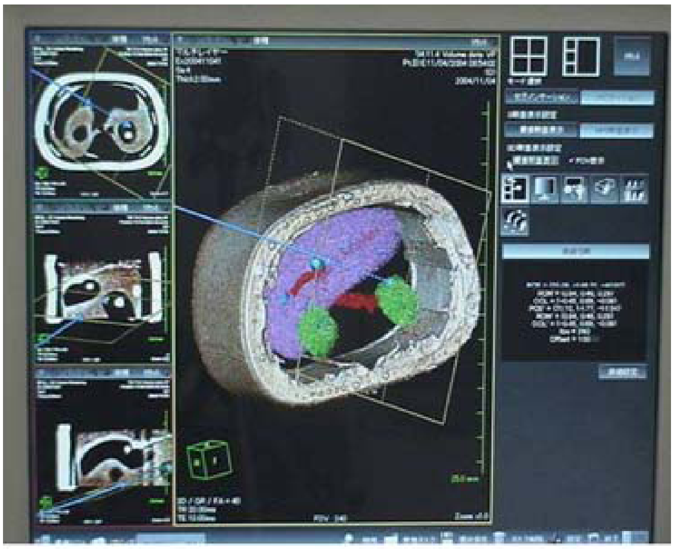

Figure 2.15: MR images on the master control screen [44].

Corral et al. developed an algorithm for automatic needle placement using a six degrees of freedom robot during minimally invasive spine procedures [45]. The algorithm is intended to be used with a C-arm fluoroscope and is based on stereo vision principles. Results show an average distance error of 1.21 ± 0.66 mm from the target point from 20 trials. Comparisons were made between alignment of the needle under joystick control and automatic needle alignment from the algorithm and fluoroscopy images. An error of 1.39 ± 1.02 mm was found in the operator controlled tests, slightly higher than that of the automatic trials.

The final example is the *PAKY* (percutaneous access to the kidney), developed by *Cadeddu* et al. [46]. The PAKY is intended for assistance in PCNL procedures. It is comprised of a seven degrees of freedom passive manipulator and an active injector system. The operating of the device mimics that of the standard PCNL techniques (see Section 2.1.4). Using a C-arm fluoroscope, the needle is aligned over the target calyx. The PAKY arm is locked in place and the C-arm rotated such that the surgeon may gauge the depth of the needle. The needle is advanced into the patient by a DC motor controlled by the surgeon.

2.5 Concluding Remarks

As stated in Section 2.1.7, there are many percutaneous procedures in medicine today that may vary in the specifics of the treatment plan and in the ailment treated, but involve a common step in the procedure: orientating a needle such as to reach the target area along the desired trajectory. It is thus believed that a general purpose needle positioning device could be of much use to surgeons for the initial step of positioning and inserting a needle. This initial stage of the procedure is vital and the success of the entire procedure can be dependent on the accuracy of the initial needle insertion [47]. In procedures like biopsy missing the target anatomy will result in faulty diagnosis, whilst in ablation incorrect needle placement has been recognized as the most significant cause of failure [47]. In PCNL, urologists have much difficulty in gaining access to the desired calyx and often this stage is performed by a radiologist, creating the need for two specialists [48]. Hence using imaging and computing technology to accurately orientate the needle by manipulation of a robotic guide will greatly improve the success of these minimally invasive procedures. The relatively low cost and availability of fluoroscopy and ultrasound imaging modalities is considered to out-weigh the disadvantages of using these devices.

The systems discussed in Section 2.4.2 to aid surgeons in minimally invasive procedures, are highly sophisticated and consequently carry high price tags. There is thus a need for a novel, low-cost device. This device may still greatly assist surgeons without expensive materials and components such as high-tech sensors and state of the art actuators.

Chapter 3

Multiple View Geometry and Image Processing

As stated in the objectives for this thesis, the system uses a standard C-arm fluoroscope as the imaging modality. It is the images from this device that are to be processed and analysed. This chapter begins by discussing the computer vision theory implemented on the fluoroscope images. Following this, the camera model used to model the projection of the three-dimensional scene onto an image is described. Finally, multiple view geometry, used to re-create the three-dimensional scene from the images, is elaborated on. Much of the theory discussed in this chapter is derived from *Hartley and Zisserman* [49].

3.1 Computer Vision Theory

The aspects of computer vision theory which are important to this thesis are homographies and projective transformation. Before these can be discussed, the projective space must be introduced.

3.1.1 The Projective Space

In two-dimensional Euclidean Geometry ($\mathbb{R}^2$), two lines always meet in a point, except for the case where the two lines are parallel (sometimes said to "meet at infinity"). Projective space, an extension of Euclidean space, avoids having to make this exception.

A point in $\mathbb{R}^2$ is represented by an ordered pair of real numbers, (x, y). The corresponding point in projective space ($\mathbb{P}^2$) is denoted as $(x, y, 1)$. Thus, a 1 is simply appended to the pair of real numbers to transform the point to projective space. A more general form of the point in $\mathbb{P}^2$ may be written as (kx, ky, k), for any non-zero k. This is known as the homogeneous coordinates of the point (x, y). Whilst this has been shown for $\mathbb{R}^2$ and $\mathbb{P}^2$, this concept can be extended to $\mathbb{R}^n$ and $\mathbb{P}^n$.

3.1.2 Homographies and Projective Transformation

A projective transformation, in $\mathbb{P}^n$, is a mapping of the homogeneous coordinates representing a point, by multiplying the coordinate vector (an $(n+1)$ vector) by a non-singular matrix (an $(n+1) \times (n+1)$ matrix). This can be expressed mathematically as:

$$X' = HX \tag{3.1}$$

where X, X' and H are the original points, the mapped points and the projective transformation respectively. As H may be multiplied by a non-zero scale factor without altering the projective transformation, H is also known as a "homogeneous matrix" or an "homography". A common problem is, given the points X and X', to compute H. Here two common cases are discussed, namely transformations from 2D to 2D ($\mathbb{P}^2$ to $\mathbb{P}^2$) and from 3D to 2D ($\mathbb{P}^3$ to $\mathbb{P}^2$).

2D to 2D Case

A transformation from $\mathbb{P}^2$ to $\mathbb{P}^2$ is very common, such as the transformation of an image. Examples include changing the scale, straightening or rotating an image. *Hartley and Zisserman* [49] describe the problem as follows: "Given a set of points $\mathbf{x}_i$ and a corresponding set of points $\mathbf{x}'_i$ both in $\mathbb{P}^2$, compute the projective transformation that takes each $\mathbf{x}_i$ to $\mathbf{x}'_i$." Here the projective transformation is the homography, H, in equation (3.1).

First one must consider how many point-to-point correspondences are required to constrain H. Whilst the matrix H contains 9 entries, it is defined only up to scale and thus the total number of degrees of freedom in such a transformation is eight. A point in $\mathbb{P}^2$ has two degrees of freedom corresponding to the x and y components only, since the scale is arbitrary. As each point-to-point correspondence accounts for two constraints, a total of four point matches are required to constrain H fully.

The Direct Linear Transformation (DLT) Algorithm

The Direct Linear Transformation (DLT) is a simple linear algorithm for finding H when given a set of four point-to-point correspondences, in $\mathbb{P}^2$. Prior to implementing the DLT algorithm on the set of points, *Hartley and Zisserman* [49] emphasise the importance of data normalisation: It improves accuracy and makes the algorithm invariant when choosing scale and coordinate origin. The normalisation method is performed by executing the following steps:

1. The image point coordinates are translated so that their centroids coincide with the origin.

2. The points are then scaled so that the average distance from the origin is $\sqrt{2}$.

These steps are applied to the images independently. The equation $\mathbf{x}'_i = H\mathbf{x}_i$ may be expressed as the vector cross product $\mathbf{x}'_i \times H\mathbf{x}_i = 0$. If the j-th row of the matrix H is denoted by $\mathbf{h}^{jT}$, then

$$H\mathbf{x}_i = \begin{pmatrix} \mathbf{h}^{1T}\mathbf{x}_i \\ \mathbf{h}^{2T}\mathbf{x}_i \\ \mathbf{h}^{3T}\mathbf{x}_i \end{pmatrix}.$$

Writing $\mathbf{x}'_i = (x'_i, y'_i, w'_i)$, the cross product above may be expressed as

$$\mathbf{x}'_i \times H\mathbf{x}_i = \begin{pmatrix} y'_i\mathbf{h}^{3T}\mathbf{x}_i - w'_i\mathbf{h}^{2T}\mathbf{x}_i \\ w'_i\mathbf{h}^{1T}\mathbf{x}_i - x'_i\mathbf{h}^{3T}\mathbf{x}_i \\ x'_i\mathbf{h}^{2T}\mathbf{x}_i - y'_i\mathbf{h}^{1T}\mathbf{x}_i \end{pmatrix}$$

As a result of $\mathbf{h}^{jT}\mathbf{x}_i = \mathbf{x}_i^T\mathbf{h}^j$ for $j = 1, 2, 3$, a set of three equations in the entries of H may be written in the form

$$\begin{bmatrix} \mathbf{0}^T & -w'_i\mathbf{x}_i^T & y'_i\mathbf{x}_i^T \\ w'_i\mathbf{x}_i^T & \mathbf{0}^T & -x'_i\mathbf{x}_i^T \\ -y'_i\mathbf{x}_i^T & x'_i\mathbf{x}_i^T & \mathbf{0}^T \end{bmatrix} \begin{pmatrix} \mathbf{h}^1 \\ \mathbf{h}^2 \\ \mathbf{h}^3 \end{pmatrix} = \mathbf{0} \tag{3.2}$$

Equations (3.2) have the form $\mathbf{A}_i\mathbf{h} = 0$, where $\mathbf{A}_i$ is a 3×9 matrix, and $\mathbf{h}$ is a 9-vector made up of the entries of the matrix H, shown as

$$\mathbf{A}_i = \begin{bmatrix} \mathbf{0}^T & -w'_i\mathbf{x}_i^T & y'_i\mathbf{x}_i^T \\ w'_i\mathbf{x}_i^T & \mathbf{0}^T & -x'_i\mathbf{x}_i^T \\ -y'_i\mathbf{x}_i^T & x'_i\mathbf{x}_i^T & \mathbf{0}^T \end{bmatrix}, \mathbf{h} = \begin{pmatrix} \mathbf{h}^1 \\ \mathbf{h}^2 \\ \mathbf{h}^3 \end{pmatrix}, H = \begin{bmatrix} h_1 & h_2 & h_3 \\ h_4 & h_5 & h_6 \\ h_7 & h_8 & h_9 \end{bmatrix} \tag{3.3}$$

Although there are three equations (one for each row of $\mathbf{h}$) in equation (3.2), only two are linearly independent. The third row is obtained, up to scale, by a linear combination of the first two rows (with x'_i times the first row and y'_i times the second). Each point correspondence gives two equations in the entries of H. Equation (3.2) can thus be written as shown in equation (3.4), with row three omitted.

$$\begin{bmatrix} \mathbf{0}^T & -w'_i\mathbf{x}_i^T & y'_i\mathbf{x}_i^T \\ w'_i\mathbf{x}_i^T & \mathbf{0}^T & -x'_i\mathbf{x}_i^T \end{bmatrix} \begin{pmatrix} \mathbf{h}^1 \\ \mathbf{h}^2 \\ \mathbf{h}^3 \end{pmatrix} = \mathbf{0} \tag{3.4}$$

Equation (3.4) can now be written in the form $\mathbf{A}_i\mathbf{h} = 0$, where $\mathbf{A}_i$ is a 2×9 matrix.

Given a set of four point correspondences, a set of equations $\mathbf{A}\mathbf{h} = 0$ is obtained. Here, $\mathbf{A}$ is the matrix of equation coefficients created from the matrix rows $\mathbf{A}_i$ which arise from each correspondence, $\mathbf{h}$ is the vector of unknown entries of H. The matrix $\mathbf{A}$ has rank 8 and thus a solution for $\mathbf{h}$ can be found by determining the one-dimensional null-space of $\mathbf{A}$. This solution, $\mathbf{h}$, can only be determined up to a non-zero scale factor. H, however, is usually only determined up to scale, so the solution $\mathbf{h}$ is acceptable in that it gives the required H.

If more than four point correspondences are given, then the set of equations arising from equation (3.4) is over-determined. This is not an issue if the image coordinates ($\mathbf{x}'_i$, $\mathbf{x}_i$) are known exactly; the equation can be solved as before by finding the one-dimensional null-space of $\mathbf{A}$. However, when working with images, the measurement of the desired coordinate is not known exactly as a result of noise present in the image. An exact, non-trivial solution will not exist for the over-determined system. An approximate solution can be found, however, by finding a vector $\mathbf{h}$ that minimizes a suitable cost function. This may be done by a technique known as Singular Value Decomposition (SVD). The technique is elaborated on in Appendix A.

3D to 2D Case

For the 2D to 2D case, the example used was that of finding an homography, H, from one image to another. Now consider the case when the homography is mapping 3D, or world points, onto a 2D image. The same theory shown for the 2D to 2D case can be applied for this scenario. The normalisation steps in Section 3.1.2 are applied, but with the points scaled and rotated such that the average distance from the origin is now $\sqrt{3}$. A matrix P exists, such that

$$x = PX \tag{3.5}$$

where x is a matrix of point coordinates in an image and X is a matrix of the corresponding points in the world scene. P is the homography mapping X to x. P is now a 3×4 matrix, unlike H, which was 3×3. For each world point to image point correspondence the following equation can be constructed:

$$\begin{bmatrix} \mathbf{0}^T & -w'_i\mathbf{x}_i^T & y'_i\mathbf{x}_i^T \\ w'_i\mathbf{x}_i^T & \mathbf{0}^T & -x'_i\mathbf{x}_i^T \\ -y'_i\mathbf{x}_i^T & x'_i\mathbf{x}_i^T & \mathbf{0}^T \end{bmatrix} \begin{pmatrix} \mathbf{P}^1 \\ \mathbf{P}^2 \\ \mathbf{P}^3 \end{pmatrix} = \mathbf{0} \tag{3.6}$$

where each $\mathbf{P}^{iT}$ is a 4-vector, the i-th row of $\mathbf{P}$. As before, due to linear dependence, the third row may be eliminated leaving the following equation to be solved

$$\begin{bmatrix} \mathbf{0}^T & -w'_i\mathbf{x}_i^T & y'_i\mathbf{x}_i^T \\ w'_i\mathbf{x}_i^T & \mathbf{0}^T & -x'_i\mathbf{x}_i^T \end{bmatrix} \begin{pmatrix} \mathbf{P}^1 \\ \mathbf{P}^2 \\ \mathbf{P}^3 \end{pmatrix} = \mathbf{0} \tag{3.7}$$

which may be written in the form $\mathbf{A}_i\mathbf{P} = 0$. If the matrix $\mathbf{A}_i$ is stacked up to form a matrix $\mathbf{A}$, a $2n \times 12$ matrix is obtained, where n is the number of correspondences. In this case, the minimum number of point correspondences needed to solve the equation $\mathbf{A}P = 0$ is $5\frac{1}{2}$ (≈ 6) as P has 11 degrees of freedom, two equations obtained per correspondence. Similar to the 2D to 2D case, the matrix P is determined using the SVD technique.

As this matrix P takes world points and transforms them to image points, it is essentially performing the same functions as a camera, which also is a mapping between the 3D world and a 2D image. It is thus known as the *Camera Projection Matrix*. The following section takes a more detailed look into this matrix and the entries comprising it.

3.2 Camera Model and the Camera Projection Matrix

The Camera Projection Matrix is an homography which transforms points from $\mathbb{P}^3$ to $\mathbb{P}^2$. Three-dimensional world points are transformed or mapped onto a two-dimensional image. Whilst the previous section showed how such an homography may be found when both sets of corresponding points are known, this section will detail how the format of the matrix is derived from a model of the camera. It will also be shown that cameras do not perform this transformation perfectly and that some distortion due to the lens is involved. The section will conclude with how a camera may be calibrated, an important and necessary task of this thesis.

3.2.1 Camera Model

The camera model used to derive the camera projection matrix is known as the pinhole camera model. An illustration of the pinhole camera geometry is shown in Figure 3.1.

In Figure 3.1, the world point $\mathbf{X} = (X, Y, Z)^T$, in the world coordinate system with $\mathbf{C}$ as the origin, is mapped to the image point $\mathbf{x} = (x, y)^T$ on the image plane, with $\mathbf{p}$ (the principle point) as the origin. The point $\mathbf{x}$ is found on the image plane where a line drawn from $\mathbf{C}$ to $\mathbf{X}$ intersects the plane. $\mathbf{C}$ is the camera centre and all points in space are projected onto the image plane by a line drawn from the point to the camera centre.

Let f denote the focal length of the camera, the distance between $\mathbf{C}$ and $\mathbf{p}$. Then it can be shown, by similar triangles, that $\mathbf{X}$ is mapped to the point $(fX/Z, fY/Z, f)$. This mapping can be expressed in the following manner, where only the image plane is of concern and thus the final coordinate is ignored:

$$(X, Y, Z)^T \mapsto (fX/Z, fY/Z)^T. \tag{3.8}$$

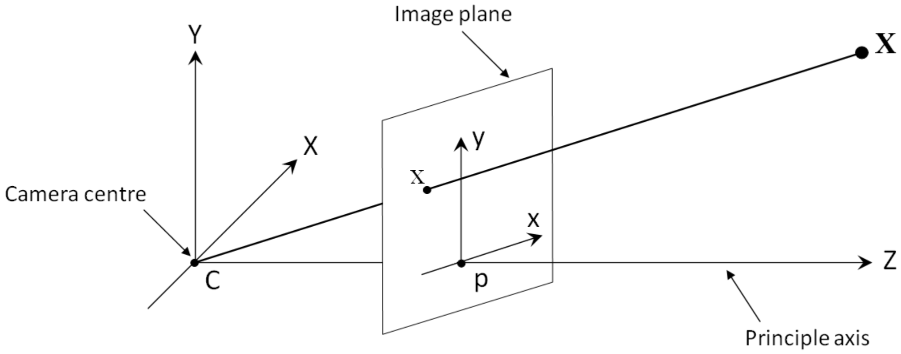

Figure 3.1: Pinhole camera model geometry, showing the camera centre (C), image plane and principal axis.

If the world and image points are expressed in projective space as homogeneous coordinates, then equation (3.8) may be re-written as:

$$\begin{pmatrix} X \\ Y \\ Z \\ 1 \end{pmatrix} \mapsto \begin{pmatrix} fX \\ fY \\ Z \end{pmatrix} = \begin{bmatrix} f & & & 0 \\ & f & & 0 \\ & & 1 & 0 \end{bmatrix} \begin{pmatrix} X \\ Y \\ Z \\ 1 \end{pmatrix}. \tag{3.9}$$

The equation (3.8) assumed that the origin of the image plane is at the principle point, **p**. In practice, this is not always true. An offset in the x and y directions must be taken into account as follows,

$$(X, Y, Z)^T \mapsto (fX/Z + p_x, fY/Z + p_y)^T \tag{3.10}$$

and so equation (3.9) may now be written as

$$\begin{pmatrix} X \\ Y \\ Z \\ 1 \end{pmatrix} \mapsto \begin{pmatrix} fX + Zp_x \\ fY + Zp_y \\ Z \end{pmatrix} = \begin{bmatrix} f & & p_x & 0 \\ & f & p_y & 0 \\ & & 1 & 0 \end{bmatrix} \begin{pmatrix} X \\ Y \\ Z \\ 1 \end{pmatrix}. \tag{3.11}$$

Letting

$$K = \begin{bmatrix} f & & p_x \\ & f & p_y \\ & & 1 \end{bmatrix},$$

equation (3.10) can now be written in a concise form as,

$$\mathbf{x} = K[I \mid 0]\mathbf{X}_{cam}. \tag{3.12}$$

The notation $\mathbf{X}_{cam}$ is used to show that the world point is described with the camera centre as the origin, called the *camera coordinate frame*. Often the world point is described with respect to a different coordinate system, known as the *world coordinate frame*. These two coordinate frames are related by a translation and rotation, expressed as

$$\mathbf{X}_{cam} = \begin{bmatrix} R & -RC \\ 0 & 1 \end{bmatrix} \mathbf{X} \tag{3.13}$$

where R is a 3×3 rotation matrix representing the orientation of the camera coordinate frame in the world coordinate frame and C the camera centre. Combining equations (3.13) and (3.12) gives

$$\mathbf{x} = KR[I \mid -C]\mathbf{X}_{cam}. \tag{3.14}$$

3.2.2 CCD Camera Model

As described in Section 1.2, the imaging device to be used in this system is a C-arm fluoroscopy X-ray device. For images taken by this device, it cannot be assumed that the pixel height and width of the image produced are equal. This is true for all Charge-coupled Device (CCD) camera types. There is thus some uneven scaling in the x and y directions. The CCD camera model takes this into account by making a slight change to the matrix K of the pinhole camera model,

$$K = \begin{bmatrix} \alpha_x & & p_x \\ & \alpha_y & p_y \\ & & 1 \end{bmatrix} \tag{3.15}$$

where $\alpha_x = fm_x$ and $\alpha_y = fm_y$, m_x and m_y are scaling factors in the x and y directions respectively. One may continue and add x_0 and y_0; the principle point in terms of pixel dimensions, with $x_0 = m_x p_x$ and $y_0 = m_y p_y$. Finally, to complete the CCD model, a skew parameter s is introduced. The axes of a pixel may not align at 90° and this parameter realigns the axes correctly. So the elements of K are now

$$K = \begin{bmatrix} \alpha_x & s & x_0 \\ & \alpha_y & y_0 \\ & & 1 \end{bmatrix}. \tag{3.16}$$

The matrix K contains the intrinsic or internal parameters of the camera.

3.2.3 Camera Projection Matrix

As stated in Section 3.2, the camera projection matrix is the matrix which maps the 3D world scene to a 2D image. This mapping may be written as $\mathbf{x} = \mathbf{PX}$. From the pinhole camera model and the additions from the CCD model, the 3×4 matrix P is thus expressed as

$$P = KR[I \mid -C], \tag{3.17}$$

with

$$K = \begin{bmatrix} \alpha_x & s & x_0 \\ & \alpha_y & y_0 \\ & & 1 \end{bmatrix} \tag{3.18}$$

and R and C the rotation and translation respectively of the camera centre expressed in the world coordinate frame. The camera projection matrix is thus a product of the intrinsic parameters matrix (K) and the external parameters ($R[I \mid -C]$) of the camera.

3.2.4 Lens Distortion Model

The camera model described in the previous section made the assumption that the world point, image point and camera centre are collinear. This camera model may thus be referred to as a linear model. However, for real cameras, including a C-arm fluoroscope, this assumption does not hold. This is as a result of the lens causing distortion. For accurate camera calibration, the image points must be undistorted.

Two types of distortions are common; radial, a result of the concave shape of the lens, and tangential, caused by inaccurate lens component centring. *Chintalapani* et al. analysed C-arm distortion in [50]. They discuss a third kind of distortion known as *S-curve* distortion. A grid of points will appear in a distinctive “S” shape when imaged by a device subjected to this distortion. An example, from [50], is shown in Figure 3.2. The authors also highlight that C-arm distortion, of any kind, is dependent on the pose of the C-arm.

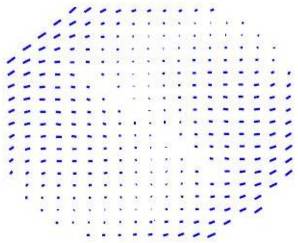

Figure 3.2: An example of S-curve distortion from [50], where a grid of points forms a distinctive “S” shape.

From the images acquired by the C-arm device used for this thesis, it could not be ascertained whether the images were subject to S-curve distortion. A statistical analysis of the distortion was considered not within the scope of the thesis. What was clear from all images taken was the prominence of radial distortion. Radial distortion is far more pronounced then tangential and thus most distortion models only take into account that of the radial type. Radial distortion occurs in two different forms; *fishbowl* (also known as *barrel*) and *pincushion*. These types of distortions are best explained by the following images, see Figure 3.3.

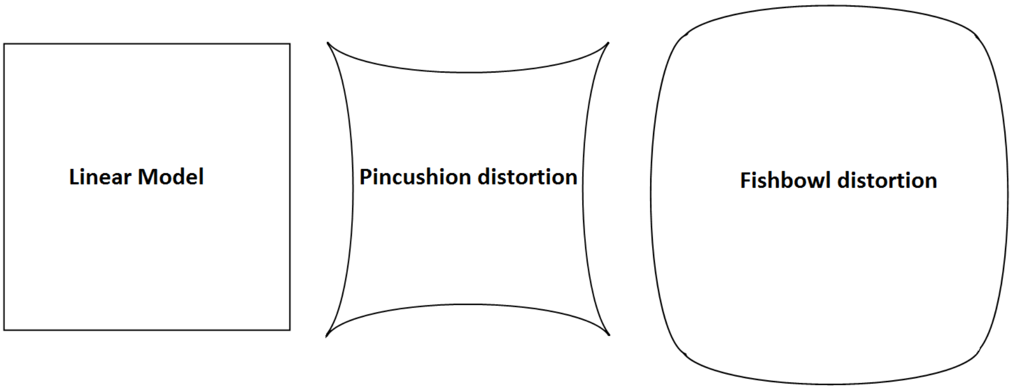

Figure 3.3: An image of a square with no radial distortion (left), an image of the same square with pincushion distortion (centre) and with fishbowl distortion (right).

The distortions shown in Figure 3.3 are exaggerated to show their effects. The images produced by the C-arm fluoroscope used in this thesis, the *Philips BV Pulsera*, are subjected to pincushion distortion. The image points must thus be corrected or undistorted. *Hartley and Zisserman* [49] describe a model for radial distortion as follows:

$$\hat{x} = x_c + L(r)(x - x_c),\ \hat{y} = y_c + L(r)(y - y_c)$$

where (x, y) are the measured coordinates (subjected to distortion), $(\hat{x}, \hat{y})$ are the corrected coordinates, (x_c, y_c) is the centre of radial distortion and finally $r^2 = (x - x_c)^2 + (y - y_c)^2$. The function $L(r)$ is a distortion factor and is given as $L(r) = 1 + k_1 r + k_2 r^2$. Whilst *Hartley and Zisserman* [49] describe $L(r)$ to higher order coefficients, in this thesis the function is only taken up to the second order. A third degree polynomial was experimented with, but did not yield significantly better results.

The objective is to determine $\{k_1, k_2, x_c, y_c\}$. Here, the centre of radial distortion, (x_c, y_c), was assumed to coincide with the image centre. The determination of the distortion coefficients, $\{k_1, k_2\}$, is done in an iterative manner in conjunction with the computing of the camera projection matrix and is discussed in the next section.

3.2.5 Camera Calibration

A calibration object is used to aid the calibration process. This object is discussed in detail in the following chapter. For now, all that is of concern is that it is an object whose dimensions are known exactly. Thus, for images of this object, the image coordinates will be known and so will the world coordinates. With this information, the camera projection matrix can be determined using the theory presented in Section 3.1.2.

The success of the calibration process can be tested by back-projecting the world points onto the image plane, using the camera projection matrix computed, and observing how well these points coincide with the original image points. In practice, these points rarely coincide. The difference between the original points and the back-projected points is known as the back-projection error. *Van der Merwe* [51] implemented an algorithm to minimise this error whilst at the same time determining the distortion coefficients discussed in the previous section. With the back-projection error minimised, the resulting camera projection matrix will be satisfactory. The algorithm implemented by *Van der Merwe* [51] works as follows:

1. Select starting values for the distortion coefficients.
2. Make a copy of the image coordinates and compute the new coordinates using the distortion coefficients.
3. Compute the camera projection matrix using the new coordinates.
4. Back-project the world points using the camera projection matrix.
5. Compute the back projection error.
6. Compute the sum of the mean and standard deviation of the error-set. If these values do not converge, adjust the distortion coefficients and return to (2). If there is convergence, return the optimised camera projection matrix and distortion coefficients.

The results of the above algorithm can be seen in Chapter 6. Step (6) used the *SciPy* module's optimisation package in *Python*, using the *Least Squares* optimization algorithm. The distortion factor, $L(r)$, may now be used with the distortion coefficients returned by the above algorithm to correct the image points. With a set of images, corrected for distortion, and the camera projection matrix known for each image, an arbitrary real world scene can be reconstructed from the set of images. This process is the subject of the following section.

3.3 Multiple View Geometry

When planning a surgical procedure, the exact dimensions of the internal structure of interest are not known. Medical imaging modalities allow images of the internal structure to be obtained. Multiple view geometry involves reconstructing a world scene, of which the dimensional details are not known, from multiple images of the scene. This can only be performed if for each image, the camera has been calibrated, i.e. the internal and external parameters are known and hence the camera projection matrix is known.

The next section discusses the geometry involved to perform such a real world scene reconstruction, with two images of the same scene.

3.3.1 Epipolar Geometry

Hartley and Zisserman [49] describe epipolar geometry as the "intrinsic projective geometry between two views". Figure 3.4 shows two images taken by cameras with centres at C and C'. The images are of the same world point, X, which is then mapped onto the two image planes as x and x'. The plane formed by the three points C, C' and X is known as the epipolar plane (π). The line from C to C' intersects the image planes at e and e'. These points e and e' are known as epipoles.

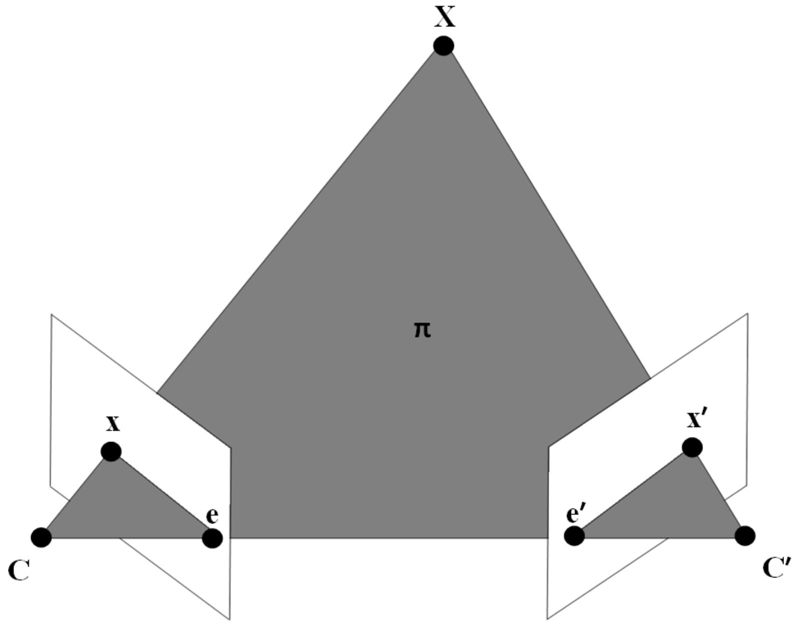

Figure 3.4: Epipolar Geometry

A common problem is, given only x, how is x' constrained. The plane π is confined by the line from C to C' and the line from x to e. Now, the unknown point x' must lie in π and hence must lie on the line from x' to e'. The lines joining x to e and x' to e' are known as epipolar lines, and one may speak of the "epipolar line corresponding to x". These lines are very useful in stereo vision (two images of the same scene) algorithms, as if a point in one of the images is known, locating the corresponding point in the other image is simplified to just finding that point on a line, instead of looking in the entire image plane.

A matrix, known as the *Fundamental Matrix*, relates a point in one image to its corresponding point in the other, stereo image. This matrix is discussed in the following section.

3.3.2 Fundamental Matrix

The fundamental matrix, F, maps points in one image to their corresponding points in the other image. This may be expressed mathematically as

$$x' = Fx$$

.

This section will present the derivation of F as described in [49]. Firstly, let the epipolar lines corresponding to x and x' be denoted as l and l' respectively. An assumption is made that the camera projection matrices, P and P', for C and C' respectively are known, as this is the case for this thesis. The ray back-projected from x to X by P is found by solving $PX = x$. The one-parameter family of solutions is shown as

$$X(\lambda) = P^{+}x + \lambda C$$

where P^{+} is the pseudo-inverse of P (i.e. $PP^{+} = I$, the identity matrix), C the camera centre, is the null-vector of P (i.e. $PC = 0$), and λ the parameter variable.

Two points, $P^{+}x$ at $\lambda = 0$ and C at $\lambda = \infty$, are imaged by the second camera P' at $P'P^{+}x$ and $P'C$ respectively in the second view. The epipolar line l' is the line joining these two projected points and is given by $l' = (P'C) \times (P'P^{+}x)$. The epipole e' is given by $P'C$. Thus, $l' = [e'] \times (P'P^{+})x = Fx$ and so F is is given as follows:

$$F = [e'] \times P'P^{+}.$$

The matrix F computed by this method also satisfies the following equation, for corresponding points x and x',

$$x'Fx = 0.$$

3.3.3 Triangulation

Of particular interest to this thesis, is the determination of a world point using two stereo images of that point. It is assumed that the camera projection matrix for each image is known. This process is known as triangulation. In practice, the lines from each image pair do not intersect (in theory they intersect at X, when coming from x and x'). This is a result of imperfect camera calibration. *Hartley and Zisserman* [49] describe linear and non-linear techniques for overcoming this issue. One method they present involves the DLT method to compute X, and was the one implemented in this thesis.

Chapter 4

System Design

As discussed in Chapter 1, the primary objective was to design a system to aid surgeons in performing percutaneous procedures. This chapter discusses the system designed to adhere to this and the other objectives of the thesis. An overview of the system and its operating principle is presented followed by a list of the initial needs and needs assessment specifications. As in the case of the thesis objectives, the system must comply with these specifications. The remainder of the chapter describes in detail the sub-systems comprising the final design.

4.1 Overview and Operating Process

The system is comprised of four components: The imaging modality, calibration object, software and the needle-positioning device. The imaging modality is the device to capture the images upon which much of the theory discussed in Chapter 3 is applied. The software component is the means by which this theory is applied; by computer code written in *Python*. The function of the calibration object was introduced in Section 3.2.5 and is essential for calibrating the camera views and determining the calibration matrix. Finally, the needle-positioning device is the device to position the needle in three-dimensional space and to orientate it in the manner desired by the surgeon.

The operating process is best explained by the two steps which make up the process: Calibration and targeting. The calibration process is the first step and is shown schematically in Figure 4.1. The calibration object is placed on the operating bed in a position where the surgeon predicts the patient's target area will lie when the patient is supine on the bed. Two images are then taken of the calibration object, by the imaging device, from two different angles. The surgeon opens these images and passes them to the software component via a GUI. These images are used as inputs for the calibration algorithm. The algorithm finally determines the calibration matrix for each image. Calibration error reports are produced and if these are satisfactory, this step is considered complete.

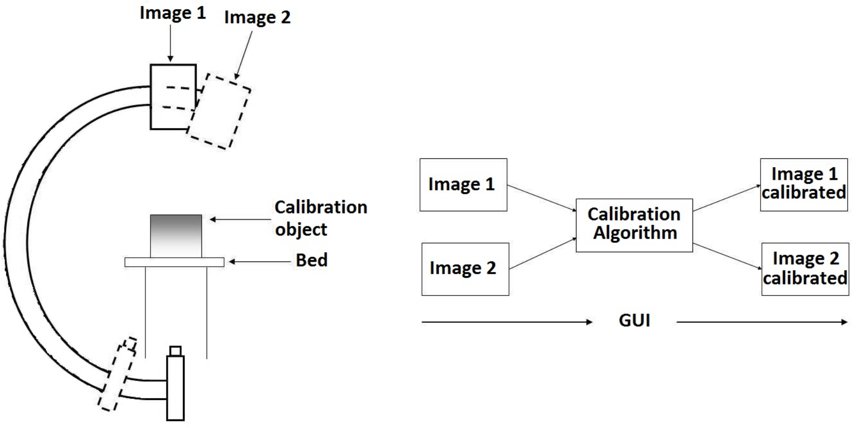

Figure 4.1: A schematic showing the calibration process

With the patient in a supine position on the bed and the needle-positioning device placed above the target area, the targeting process may begin. The process is shown graphically in Figure 4.2. Two images are acquired from positions identical to those used in the calibration process. The surgeon uses the GUI to provide these images as inputs for the targeting algorithm. Also via the GUI, the surgeon provides other inputs relevant to the desired needle position and orientation. The targeting algorithm returns a series of parameters to which the needle-positioning device must be adjusted to. The surgeon manually adjusts the device according to these parameters and may then insert the needle to the target.

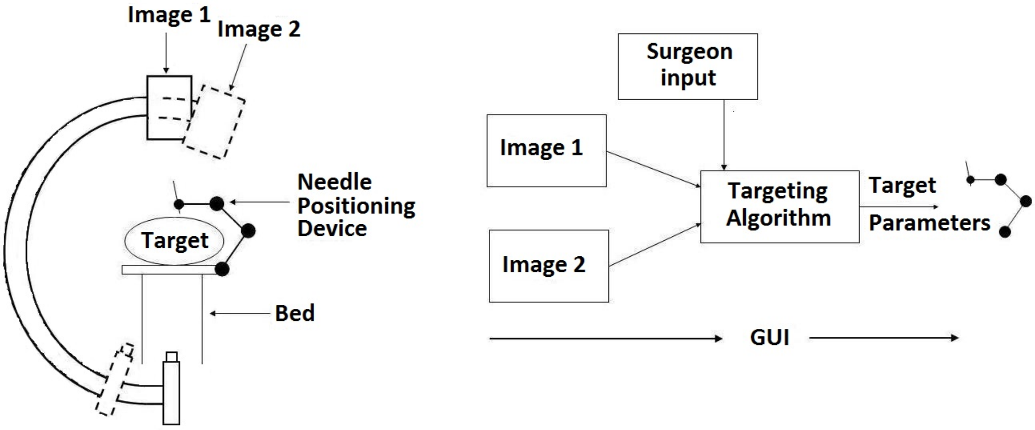

Figure 4.2: A schematic showing the targeting process

While a higher number of images would increase the accuracy of the system, the increase in operating time, due to the more intensive computation required and further C-arm positioning, do not justify a higher number of images. Furthermore, an amount of accuracy is lost with every new C-arm position, as discussed in Section 7.4, Chapter 7.

4.2 Specifications

The following table presents the initial needs requirements and their corresponding needs assessment specifications:

Table 4.1: List of initial needs and the corresponding specification(s) resulting from their assessment

	Initial Needs		**Needs Assessment**
1	Orientate and position needle in manner desired by surgeon	i	Surgeon to select points on X-ray image pair via GUI to indicate desired needle orientation
		ii	Surgeon to specify needle position via GUI
		iii	Needle-positioning device to have at least 5 degrees-of-freedom
2	Operating process must be rapid and 95 % repeatable	i	Digital display of needle-positioning device parameters
3	Access target in first attempt		
4	Safe for patient, surgeon and theatre staff	i	Surgeon manually operates needle-positioning device
5	To be used with a C-arm fluoroscopy imaging modality	i	Software algorithms to be written for images from such an imaging device
		ii	Needle-positioning device must not effect the operation of the C-arm
		iii	Needle-positioning device must not obstruct target in images
		iv	Needle-positioning device markers and calibration object markers must be visible in the images, which have a viewing circle of diameter 244 mm
6	Easily moved from one operating theatre to another	i	Total device weight must be under 15 kg
7	Rapid setup of device in operating theatre	i	Two fasteners in total needed to fix device to operating bed

8	Able to operate on a large range of patient sizes	i	150 × 150 × 150 mm minimum calibrated volume
		ii	Target within calibrated volume space
		iii	Work volume to cover a 300 mm radius half sphere
9	Accurate enough to use in a range of percutaneous procedures	i	5 mm target accuracy
10	At most 15 minutes training required to use system	i	User friendly GUI
11	Cost effective and suitable for the South African medical environment	i	Designed to attach to standard operating beds found in South African theatres
		ii	Standard materials and off-the-shelf parts
		iii	Pasts made using standard workshop equipment
		iv	Manually operated needle-positioning device

4.3 Subsystems

The following sections describe the subsystems which adhere to the needs assessment specifications listed in Section 4.2.

4.3.1 Imaging Device

As per the user defined requirements, a C-arm fluoroscopy X-ray imaging device is to be used. This is due to these devices being relatively inexpensive in comparison to other medical imagers (see Table 2.1, Section 2.2.3) and hence readily available in most operating theatres, in particular in South African hospitals. The specific C-arm fluoroscopy device used in this thesis is the *Philips BV Pulsera*. A photo of this imaging device is shown in Figure 4.3. The fundamental components of the C-arm are the X-ray tank (XT), which emits the X-rays, and the Image Intensifier (II), which receives the emitted X-rays and produces the image.

The C-arm is highly suited towards the application of stereo vision principles due to its many degrees-of-freedom. These may be seen in Figure 4.4. Of particular interest are the movements denoted “A” and “E”. With these two parameters set to their zero positions, the first image is taken. To ensure the

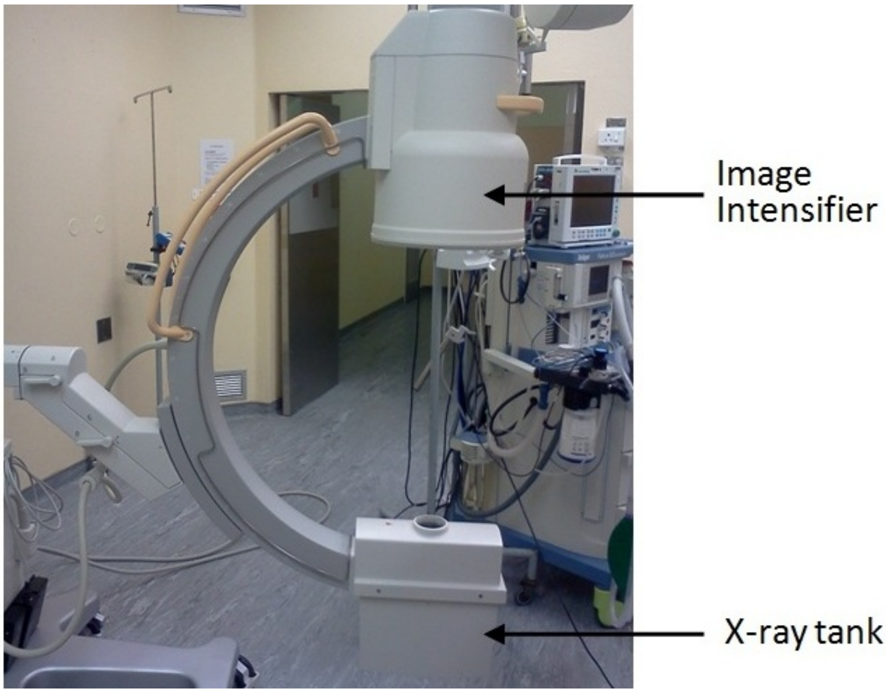

Figure 4.3: Photo of the *Philips BV Pulsera* showing the X-ray tank (XT) and the image intensifier (II)

high accuracy of the triangulation algorithm parameter “E” should ideally be set to 90° for the second image. In practice this was not possible due to the obstruction of the operating bed for angles greater than 45°. For the second image, “E” was set to 20° and “A” was moved by 40 mm to ensure that the object being imaged appeared in its entirety. These two positions are used throughout the operating procedure.

The *BV Pulsera* model used produces a 305 mm diameter viewing circle and images of 1024×1280 pixel resolution. The viewing circle diameter and the angle parameter “E” are imperative to determining the size of the calibration object, the subject of the next section.

4.3.2 Calibration Object

The function of the calibration object was discussed in Section 3.2.5 and this section will describe its design.

Whilst two-dimensional calibration objects are popular due to their low cost and ease of manufacture, the decision was made to take advantage of the C-arm’s ability to “see through” objects. Thus a three-dimensional calibration object was built. *Conradie* [17] used a three-dimensional object to calibrate a C-arm fluoroscope with success.

With parameter “E”, shown in Figure 4.4, for image 2 equal to 20°, the diagram shown in Figure 4.5 can be used to determine the overall dimensions

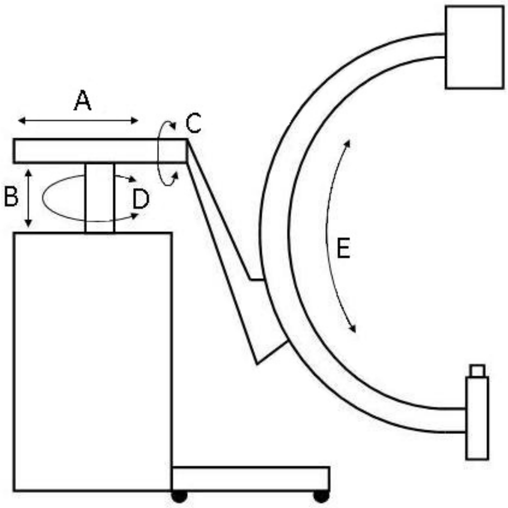

Figure 4.4: The degrees-of-freedom of the *BV Pulsera*

of the calibration object. For these calculations, the 40 mm movement of the parameter “A” was ignored. The overlapped area in Figure 4.5 is formed by the two areas made by the lines drawn from the X-ray tanks to the image intensifiers for each image position. The width (along the width of the bed) and the height of the calibration object must fit into this overlapping area. The length of the calibration object was chosen to be the same as the determined width. The overall dimensions of the calibration object were determined to be 160 × 160 × 160 mm, and this is in accordance with the needs assessment specification 8.i in Table 4.1.

Figure 4.6 shows a Computer Aided Design (CAD) model of the calibration object. The calibration object markers can be seen on three levels. Metal spheres of radius 5 mm were used as markers so they may appear in the X-ray images. The three levels within which the metal spheres are embedded are made of perspex so as not to obstruct the view of the spheres in the images, as perspex is radiolucent. Clear perspex was used so as to allow the operator to orientate the object correctly prior to taking any images. The levels are spaced correctly, 80 mm apart, in the vertical direction by the metal dowel pins. The particular layout of the spheres on each level is significant as marker occlusion is highly undesirable. It is imperative that all markers are present and can be identified in each image so that the associated calibration algorithm can operate correctly. *Conradie* [17] used a similar calibration object for a C-arm fluoroscope and had success with the object and its sphere layout. The same layout of the spheres was used for the calibration object in this thesis. For the purpose of this thesis, however, a larger calibration object, approximately four times the volume of that made by *Conradie*, was developed. A total of 35 spheres were used, with 9, 16 and 10 spheres in the top, middle and bottom levels respectively. The spheres are arranged such that all are visible from

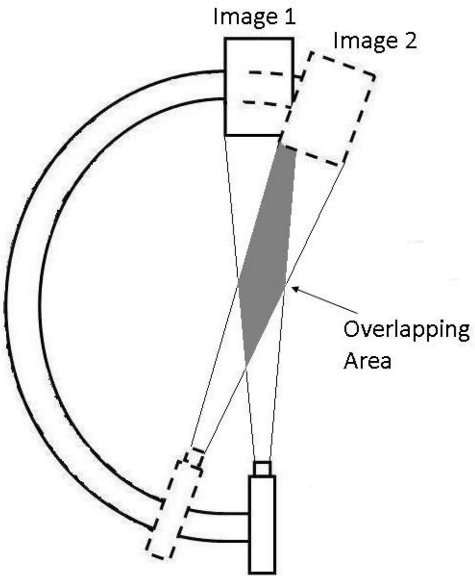

Figure 4.5: Schematic used to determine the overall dimensions of the calibration object

both C-arm positions and distinct lines are formed by the spheres when the object is viewed from the two C-arm positions (see Figure 4.7).

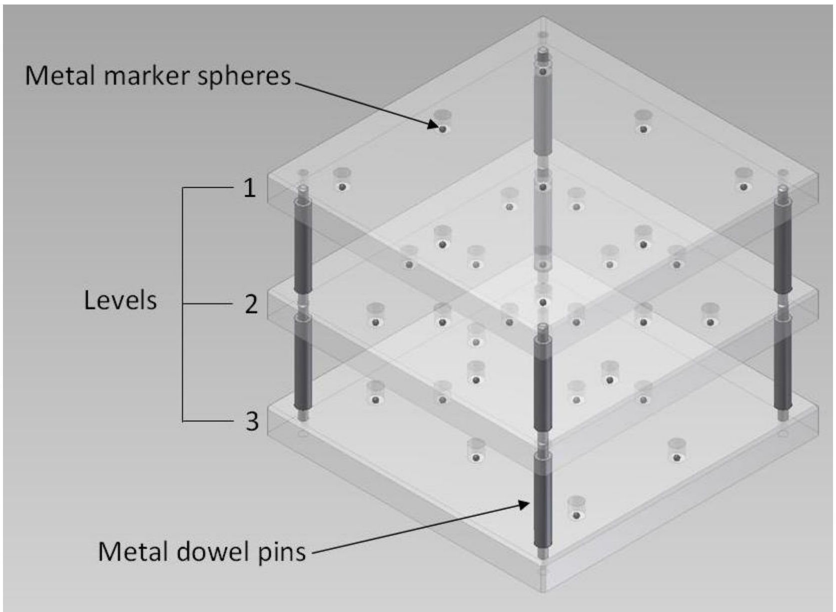

Figure 4.6: CAD model of the calibration object showing the three levels, metal markers and dowel pins

The position of each sphere needs to be known accurately such that the calibration algorithm results are accurate. The coordinates of each sphere were

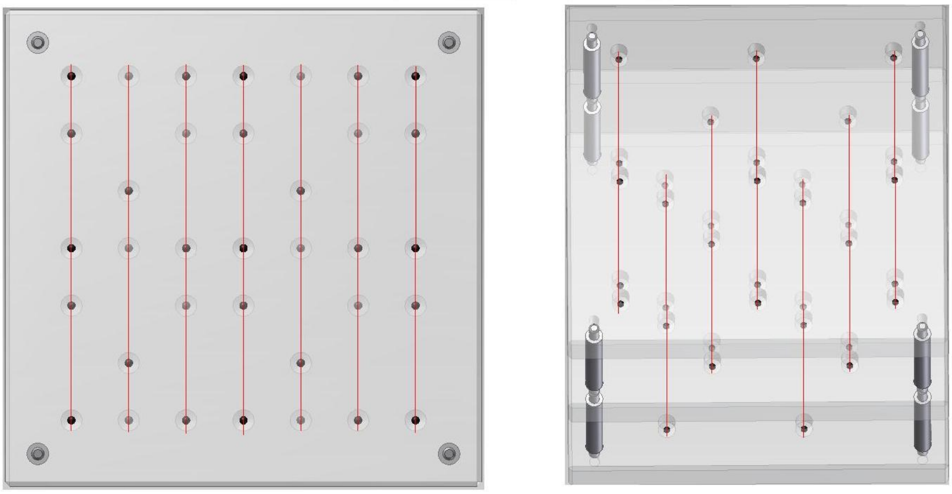

Figure 4.7: CAD model of the calibration object showing the distinct lines formed by the metallic markers, 0° position left, 20° position right

measured by a *Mitutoyo Bright* 710 coordinate measuring machine (CMM) with a reported volumetric accuracy of 3 μm. Figure 4.8 shows a photograph of the calibration object.

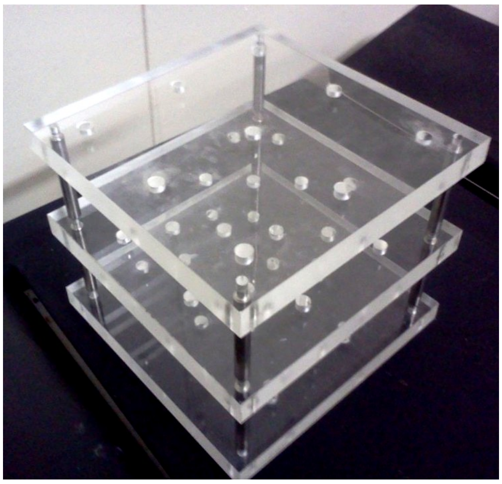

Figure 4.8: Photograph of the calibration object

4.3.3 Needle-positioning Device

The needle-positioning device is the mechanical instrument whose function is to position and orientate the needle. Specification 1.iii in Table 4.1, the needle-positioning device is to have at least five degrees-of-freedom, is a result of three degrees-of-freedom needed to position the needle and a further two degrees to orientate the needle. Many design configurations exist to achieve the required degrees-of-freedom. The following section discusses the configurations that were considered and the one ultimately chosen for the device.

Design Configuration

As the objective for the needle-positioning device was to not only position the needle in space but to also orientate it, it was decided that the last two degrees of freedom of the configuration be rotational joints. The needle can then be rotated about two axes passing through a fixed point, orientating the needle as desired. This greatly simplifies calculations as the problem of determining the parameters to position the needle, is separated from that of determining the parameters to orientate the needle (this inverse kinematics is discussed in detail in Chapter 5). What remains is to determine a kinematic arrangement for the first three degrees-of-freedom to position the needle's center of rotation, the intersection of the two afore mentioned axes, in space. Two configurations were considered, the *cartesian* manipulator and the *articulated* manipulator.

The concept of the cartesian manipulator is three links that move linearly along three independent and orthogonal axes respectively. Figure 4.9 illustrates this concept. This concept was used by *Conradie* [17] and the device they developed is shown in Figure 4.10. By having the needle, and the two rotational joints associated with it, at the end of link 3, the needle may be positioned in three-dimensional space by the three independent linear movements along each axis.

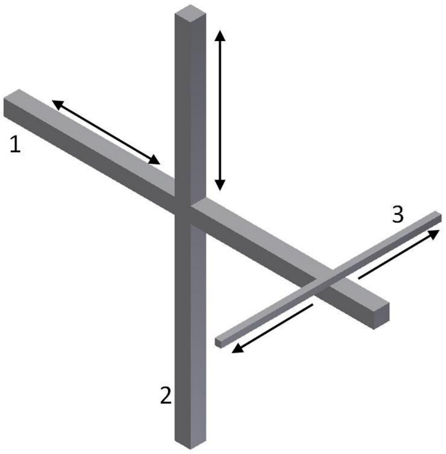

Figure 4.9: Schematic showing the concept of the cartesian manipulator

The articulated manipulator, also known as the elbow manipulator, consists of three links and three rotational joints. Figure 4.11 illustrates this concept.

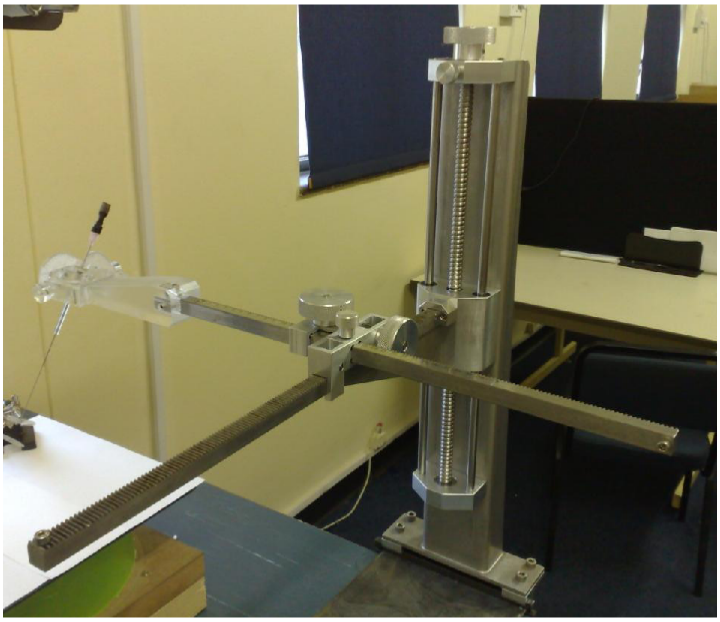

Figure 4.10: Photograph of the needle-positioning device developed by *Conradie* [17] which was based on the cartesian manipulator concept

The three links are connected by two rotational joints (B and C in Figure 4.11) with the first link connected to a base by the third rotational joint (A). As in the case with the cartesian manipulator, the needle may be positioned in space by these first three joints.

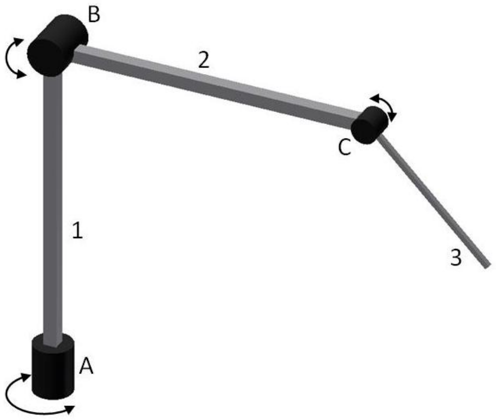

Figure 4.11: Schematic showing the concept of the articulated manipulator

Each configuration has its own characteristics and strengths. The configurations were compared by comparing characteristics relevant to achieving the specifications of the system. A list of these characteristics are compiled in Table 4.2. Each configuration is given a rating for that particular characteristics and by these ratings a comparison can be made. Whilst the ratings are not a precise measure, they are sufficient enough to make a comparison as it can be seen that one configuration performs better than the other for a particular characteristic.

Table 4.2: Comparison of cartesian and articulated manipulators.

Characteristic	**Cartesian**	**Articulated**	**Comments**
Work-volume to link length ratio	+	+++	Higher rating for higher ratio
Overall volume	+	+++	Higher rating for smaller volume
Dexterity	+	+++	
Accuracy	+++	++	
Encoders	+	+++	Regarding price and accuracy
Ratings	+ Bad	++ Good	+++ Excellent

A study of different manipulator designs was done by *Kucuk and Bingul* [52], in which they quantified various characteristics. The articulated manipulator is highly favoured as it maximises the work-volume to link length ratio. With this ratio maximised for the articulated manipulator, less material is needed and thus the overall mass and size of the device is reduced. Due to the arrangement of the links and joints, the overall volume taken up by the articulated design is also minimal. These two characteristic are highly desirable as space is very limited in operating theatres. Dexterity refers to the range of orientations possible for the tool at the end of the manipulator. High dexterity is desired as it allows the surgeon more options with regards to the angle of approach to the target.

The cartesian manipulator is considered more accurate as it is able to better support heavy loads without deforming, but this is only if there are two main supports (the vertical axis, link 2, in Figure 4.9). In both designs, errors in the encoders measuring angle or linear movement accumulate which lessens accuracy. However, in the case of the cartesian design, accuracy reduces further with any errors in orthogonality of the links. Manufacturing a cartesian manipulator such that the links are precisely orthogonal is difficult and costly. Finally, rotational encoders are cheaper, more accurate and easier to implement than the equivalent linear encoders for the cartesian system.

Based on the analysis above, it was decided to base the needle-positioning device on a articulated manipulator design.

Design Calculations

In designing an articulated manipulator, an important consideration is the size of the work-volume. The work-volume of the manipulator must at least cover a 300 mm radius half sphere, in accordance with specification 8.ii, Table 4.2. The work-volume is a function of the link lengths and the angular range of each joint, and these two entities must be determined to achieve the desired work-volume. Section B.1, Appendix B, discusses the analysis done to determine the ideal link lengths and joint angular ranges. The results are shown in Table 4.3.

Table 4.3: Link lengths and joint ranges of the final design

Link	**Length (mm)**	**Joint**	**Range** (°)
1	151	1	180
2	298	2	150
3	112	3	180
		4	360
		5	100

Components

The essential components comprising the assembly of the needle-positioning device, namely the base, links and wrist are discussed here (see Figure 4.12).

The functions of the base are to fix the device to the bed and to house the following components; the Liquid Crystal Display (LCD) for displaying the joint angles, *Arduino* microcontroller board and the first joint. The base and its associated components are shown in Figure 4.13.

The base was laser cut from 3 mm stainless steel, bent into shape and finally the side covers welded on. The *Arduino* microcontroller receives analogue signals from potentiometers positioned at each joint, converts these angles into degrees and sends these to the LCD to be displayed. The operator may then position the needle as desired by observing the angles on the LCD screen. Joint 1 consists of a shaft and bushing which is press fitted into a bracket. Joint 1 is able to be locked by turning the fixing shaft. Joint 1 turns the potentiometer so that the first angle may be measured. The two clamps fix the device to the operating bed.

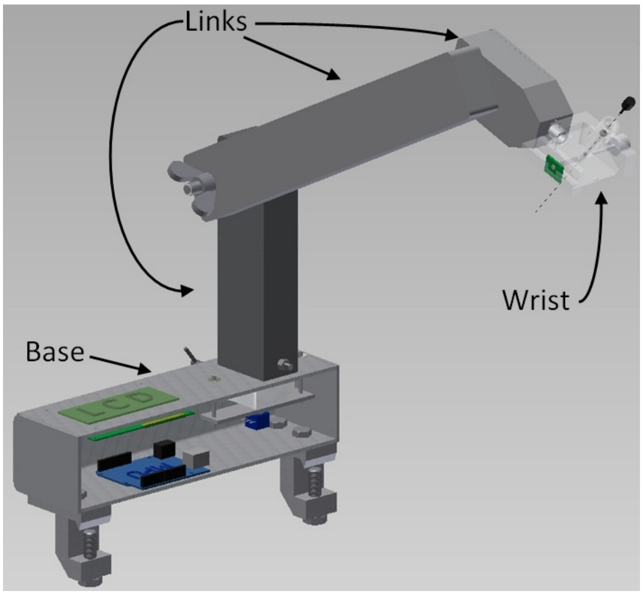

Figure 4.12: CAD model of the needle-positioning device showing the essential components

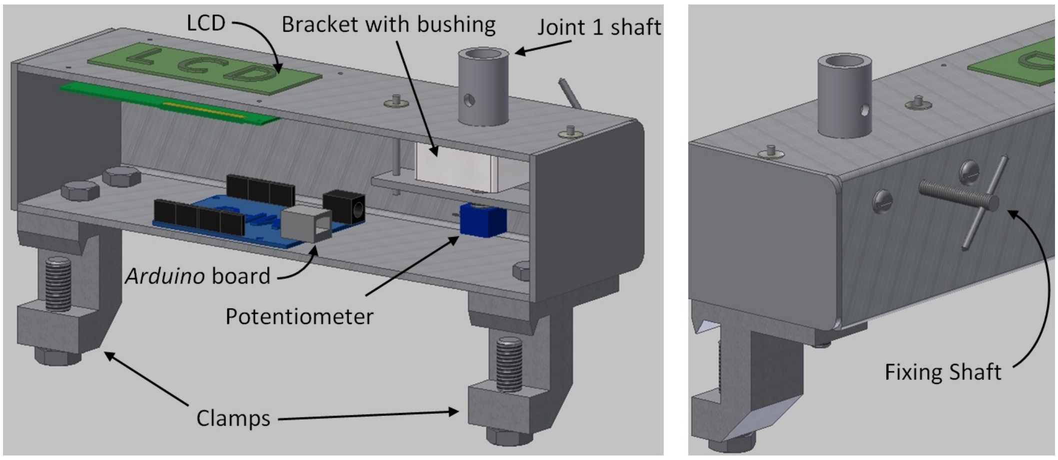

Figure 4.13: Two views of a CAD model of the base and its associated components

Whilst each link differed in length, the design was generally the same and thus only one link is shown here. Figure 4.14 shows a typical link, manufactured from polyvinyl chloride (PVC). This material was chosen so that it would not completely obstruct underlying structures in the X-ray images. The fixing shaft serves to fix the potentiometer and to provide a means to fix the succeeding link in place (Figure 4.14, right). The rotating shaft is tight-fitted onto the potentiometer shaft and rotates with the succeeding link via a grub screw. As in the case of joint 1, the potentiometer is used to measure the joint angle. The cover part has a round slot to allow the wires from the following potentiometer to pass through and not to become tangled with rotations. The wires are thus completely housed within the arms, eliminating the risk of a wire interfering with the operating process. The wing nut allows the operator to secure the link in place by hand without the need for additional tools. Appendix B, Section B.2 discusses bending moments of the links and the resulting deflection of the wrist. This was to determine how much the wrist deflects due to the deflections of the second and third arms under their own weight. This deflection varies with the pose of the arm and the maximum deflection only was computed. The maximum deflection was determined to be 0.11 mm and this is considered acceptable.

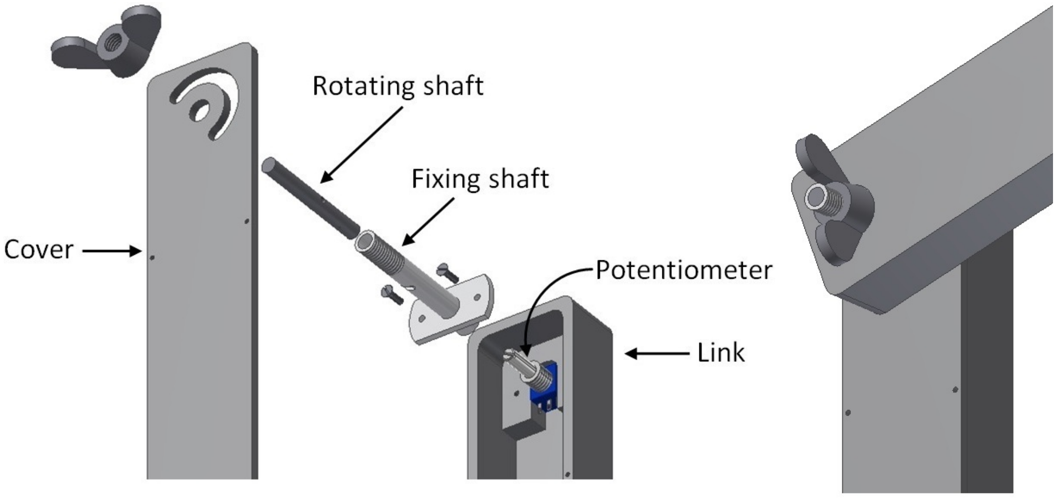

Figure 4.14: Exploded view of a link and its associated components (left) and assembled view (right) with the succeeding link included

Upon the end of the third link is the wrist component (see Figure 4.15). The wrist is connected to link 3 by shaft A, shown in Figure 4.15. This shaft rotates a potentiometer to record the angle of the fourth joint. The inner yoke rotates about a second shaft, the fifth joint (shaft B), and thus the needle is able to be rotated about two independent axes. This centre of rotation is known as the *gyro-centre*. The needle is aligned by a needle guide and when the needle cap is tightened, the rubber O-ring pushes onto the needle, holding it in place. Four metal spheres are embedded into the inner yoke (only two seen in the figure). These spheres are for the targeting algorithm and are discussed further in Chapters 5 and 6.

The fourth joint can rotate through a full 360°, whilst joint 5 is limited to 300° due to either the needle guide or the needle itself coming into contact with the outer yoke. The work-envelope for the wrist is thus a sphere with a 60° “slice” cut out.

A photograph of the complete assembly is shown in Figure 4.16.

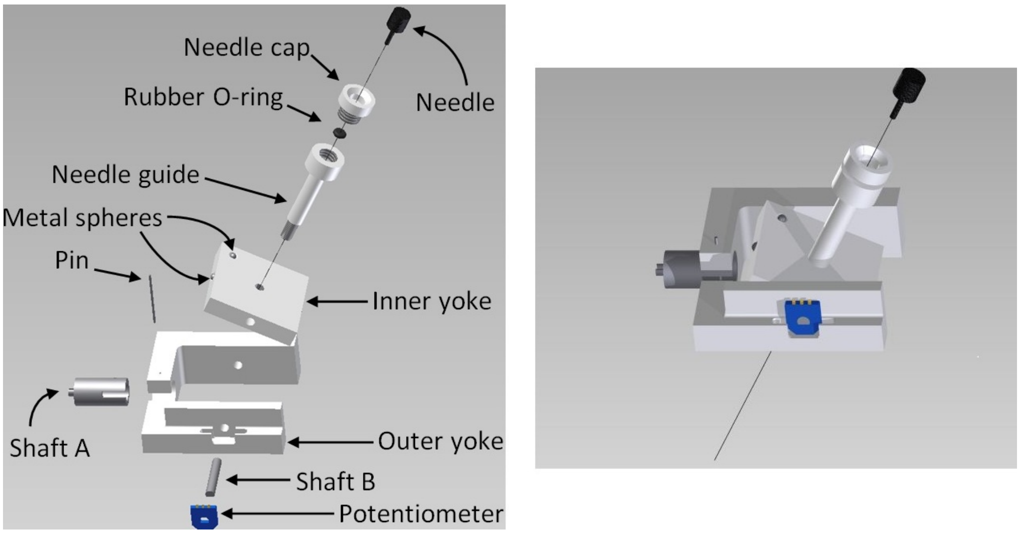

Figure 4.15: CAD model of the wrist and its associated components

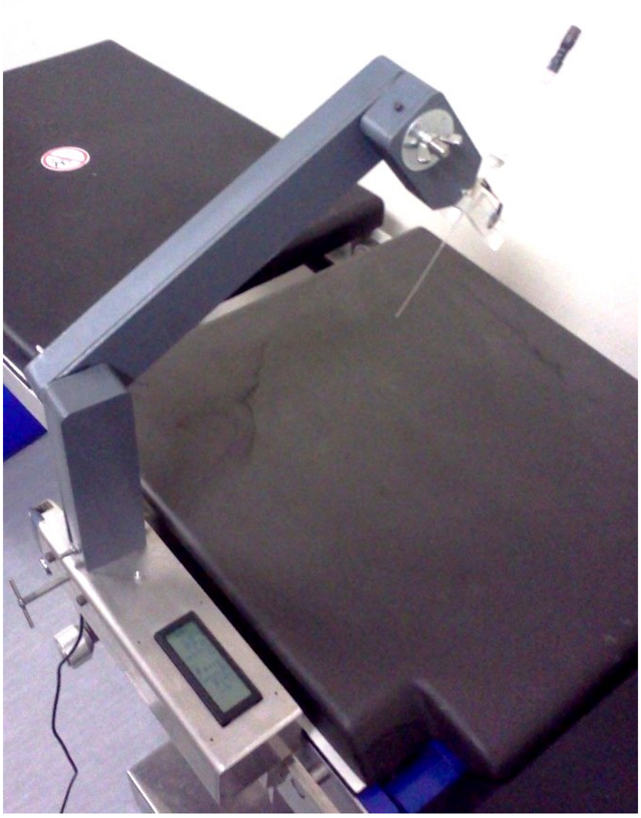

Figure 4.16: Photograph of the assembled needle-positioning device attached to a typical operating theatre bed

4.3.4 Software - Image Processing

The software subsystem is comprised of the algorithms to apply the theory discussed in Chapter 3, namely the calibration algorithm and the targeting algorithm. The final component of the software subsystem is the afore mentioned GUI. Due to the extent of this subsystem and also the necessary information of Chapter 5 to better present it, it is discussed in detail in Chapter 6. However, the image processing techniques used are discussed here.

Various image processing techniques were implemented on the C-arm fluoroscopy images. This was done prior to the application of the theory described in Chapter 3. The techniques were applied using *Python* and *OpenCV* and are briefly introduced here. The execution of these techniques and their corresponding effects on the images are also shown in Chapter 6.

Cropping

Images were firstly cropped so as to leave only parts of the image that were of interest and eliminate unnecessary data. This was performed using the *crop* function of the *Python Imaging Library*.

Spherical Marker Detection

The calibration object, mentioned briefly in Section 3.2.5 and discussed in detail in the following chapter, contains 35 spherical markers. The spherical markers had to be automatically detected. This was performed first using *cvCanny*, a built in function of *OpenCV*, to locate all contours in the image. Following this, another *OpenCV* function was used to fit a circle to each contour, *MinEnclosingCircle*. This function returns the centre of the circle and its radius. The function in general located the sphere centres precisely, but on occasion errors of up to 2 pixels were observed. A range of radii, within which the radii of the spherical markers fall, was used to delete any circles found whose radii was outside of this range.

Chapter 5

Needle Position and Orientation Computations

This chapter discusses the computations done to determine the five angles for the needle-positioning device such that it positions and orientates the needle as desired. A description of the target and how it is defined is introduced first, followed by the various coordinate systems that must be considered. The final section of the chapter reports the calculations done to determine the angles once the desired needle position and orientation is known.

5.1 Defining a Target

In defining a target, the surgeon is to indicate the desired orientation and position of the needle. In indicating the position of the needle, the surgeon is in fact indicating the desired position of the wrist gyro-centre, described in Section 4.3.3. To input the desired orientation, the surgeon selects two points on the images of the target through which the needle must traverse. This selection process is discussed in detail in Chapter 6. Figure 5.1 shows an example of 0° and 20° images of a test target object; two metal washers embedded in a sponge. The surgeon selects the centres of the two washers in each image to indicate the desired needle orientation. Finally, the surgeon inputs the distance, along the orientation vector, for the needle position.

Following the application of the triangulation algorithm on these two target images, the needle vector and position will be known in three-dimensional space. These are defined with respect to the calibration object's coordinate system, also known as the world coordinate system. There are various coordinates systems used in the process of determining the joint angles for the needle-positioning device such that the needle will be positioned and orientated as desired, and these are the topic of the next section.

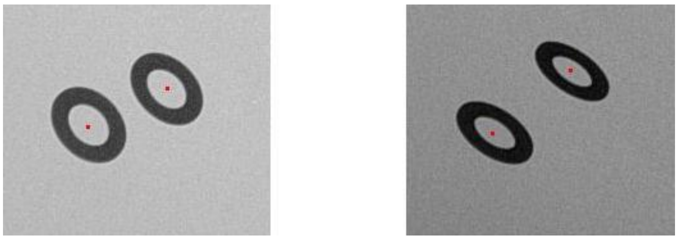

Figure 5.1: 0° (left) and 20° (right) C-arm fluoroscopy images of test target object, two metal washers, with operator's selection points

5.2 Coordinate Systems

Three coordinate systems are of relevance in the process of determining the parameters for the needle-positioning device; the world, wrist and base coordinate systems. The world system is derived from the calibration object, whilst the remaining two are connected to the wrist and base respectively. The needle position and orientation vector can be described in each of these systems, but it is necessary to have them described in the base coordinate system to determine the angles for the needle-positioning device.

5.2.1 World Coordinate System

The coordinates of the metal spheres of the calibration object are defined with respect to the coordinate system shown in Figure 5.2. Once the two images taken with the C-arm are calibrated and the calibration matrices are used for the triangulation algorithm, all points triangulated are described with respect to this coordinate system. This coordinate system is thus known as the *world coordinate system* (world CS). The origin is the centre sphere of the top level of the calibration object and the axes in the directions shown in Figure 5.2.

5.2.2 Wrist Coordinate System

The wrist coordinate system (wrist CS) is attached to the wrist and is shown in Figure 5.3. As discussed in Section 4.3.3, the wrist has metal spheres embedded in it (Figure 4.15) and these spheres are used to determine the wrist's orientation in the target images. There are four metal spheres and these can be seen in Figure 5.4, with dashed lines drawn between two pairs of spheres. The second set of images taken in the targeting process (Section 4.1), are used to find the wrist CS given with respect to the world CS.

Two lines ($l1$ and $l2$) are obtained by joining two pairs of metal spheres, as shown in Figure 5.4. The intersection of these two lines is the wrist gyrocentre and this is set as the origin of the wrist CS. The cross-product of vectors defining the direction of these two lines gives a new vector, $\overrightarrow{l1} \times \overrightarrow{l2} = x'$. This vector, x', is perpendicular to the plane formed by the two lines, however it

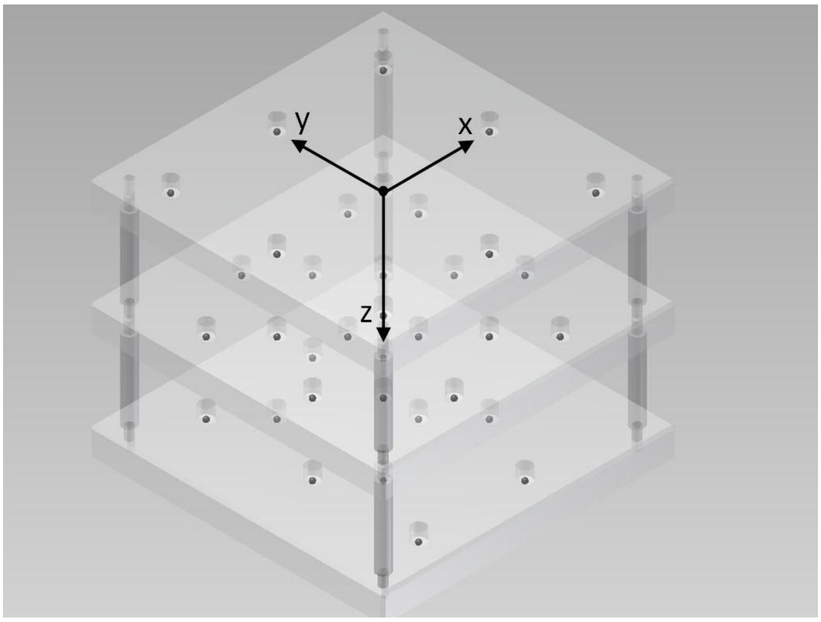

Figure 5.2: The world coordinate system, derived from the calibration object

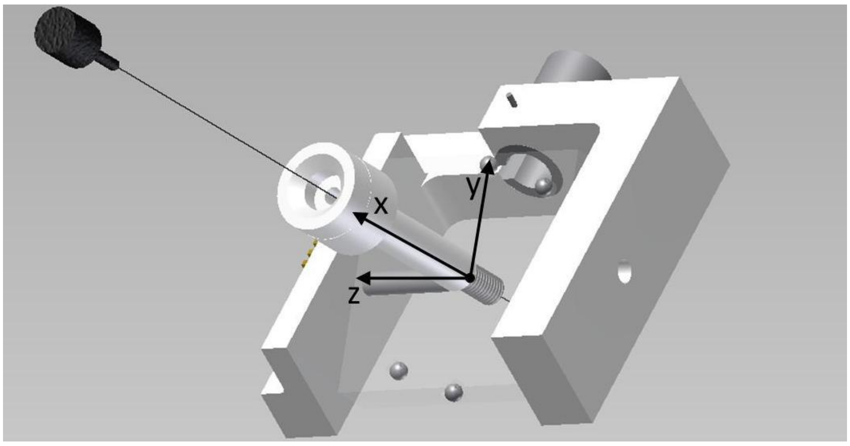

Figure 5.3: The wrist coordinate system, attached to the wrist

is not aligned with the x axis of the wrist coordinate system, x_{wrist}, due to a vertical offset of one pair of metal spheres from the other. This is shown in Figure 5.5, indicated by v. From measurements taken of the spheres by a *Mitutoyo Bright* 710 coordinate measuring machine (CMM), it was determined that x' needs to be rotated by 17° to be aligned as in Figure 5.3, opposite to the needle direction. This rotation is about the line $l2$ of Figure 5.4. With the x_{wrist} now known and y_{wrist} set to $\overrightarrow{l2}$, z_{wrist} can be found from $x_{wrist} \times y_{wrist} = z_{wrist}$.

With the wrist CS known with respect to the world CS, points defined in the world CS can be transformed to the wrist CS. This was done using the

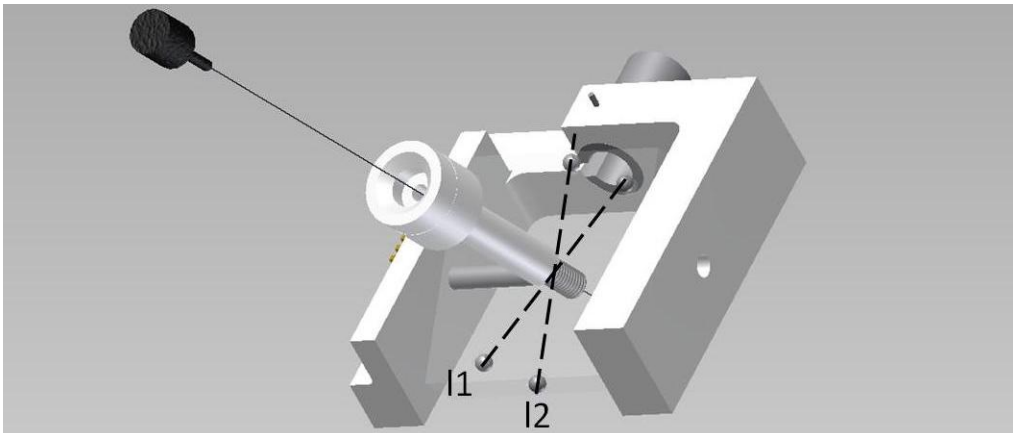

Figure 5.4: Lines formed from the two pairs of metal spheres, the intersection of the lines is the wrist gyro-centre

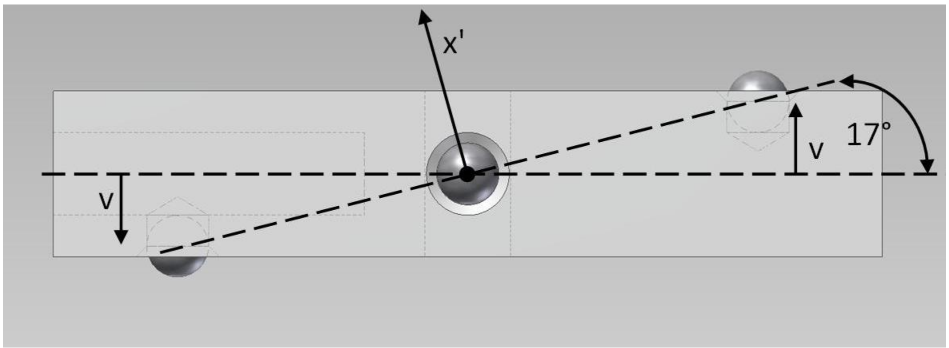

Figure 5.5: CAD model showing vertical offset (v) of one pair of metal spheres and the rotation necessary to align x' with the x axis of the wrist

following operation:

$$[H_{wrist}^{world}]^{-1}P^{world} = P^{wrist} \tag{5.1}$$

where

$$H_{wrist}^{world} = \begin{bmatrix} x_x & y_x & z_x & o_x \\ x_y & y_y & z_y & o_y \\ x_z & y_z & z_z & o_z \\ 0 & 0 & 0 & 1 \end{bmatrix} \tag{5.2}$$

and $[x_x, x_y, x_z]^T$ is a vector representing the direction of x_{wrist} in the world CS, $[y_x, y_y, y_z]^T$ the direction of y_{wrist}, and $[z_x, z_y, z_z]^T$ the direction of z_{wrist}. The vector $[o_x, o_y, o_z]^T$ is a vector from the world CS origin to the wrist CS origin. P^{world} and P^{wrist} are points defined in the world and wrist coordinate systems respectively. [53]

5.2.3 Base Coordinate System

As mentioned, the desired needle orientation and position need to be defined in the coordinate system attached to the base. This is in order to perform the calculations to determine the required joint angles. The coordinate frame attached to the base is shown in Figure 5.6.

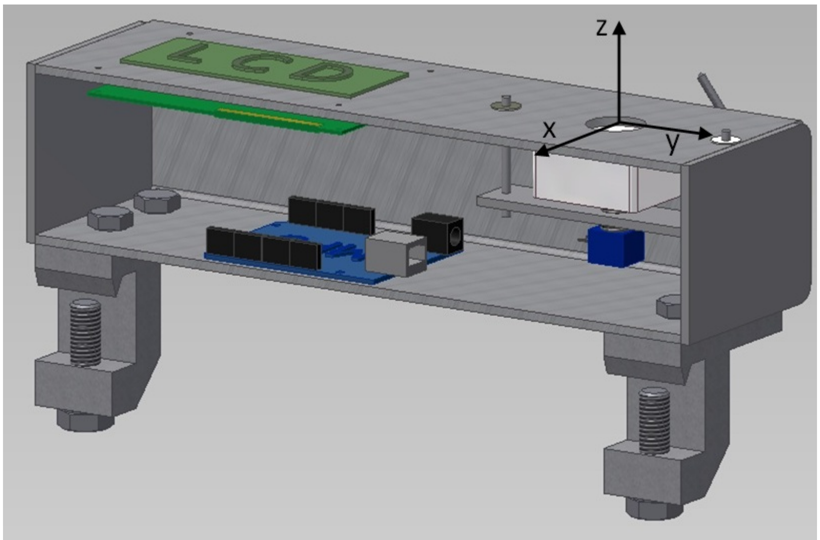

Figure 5.6: Base coordinate system

As discussed in detail in Appendix B, Section B.3, points in the wrist frame, P^{wrist}, can be transformed to the base frame, P^{base} by:

$$T^{base}_{wrist} P^{wrist} = P^{base} \tag{5.3}$$

where T^{base}_{wrist} is the transformation matrix describing the rotation and translation of the wrist frame with respect to the base frame. In Appendix B, Section B.3, the base frame and the wrist frame are referred to as frames 0 and 5 respectively. T^{base}_{wrist} can be determined from the wrist angles of the needle-positioning device for its position in the target images.

To summarise, following the application of the targeting algorithm, the desired needle position and orientation will be described with respect to the world coordinate system. These are then transformed to the wrist coordinate system using Equation 5.1. The position and orientation are then transformed to the base coordinate system using Equation 5.3.

5.3 Determining Needle-Positioning Device Angles

With the desired needle position and orientation known in the base coordinate system, the five angles to position and orientate the needle as such, may be determined.

As the x axis of the wrist coordinate frame, x_{wrist}, has been chosen to point in the opposite direction to the needle (see Figure 5.3), the desired direction of this axis, x^d_{wrist}, is known in the base frame. Also known in the base frame is the desired gyro-center, o^d_{wrist}. However, the directions of y^d_{wrist} and z^d_{wrist} are still unknown. The x axis of the base frame, x_{base}, is crossed with x^d_{wrist} to obtain $y^{d'}_{wrist}$, $y^{d'}_{wrist} = x^d_{wrist} \times x_{base}$ and $z^{d'}_{wrist}$ is obtained from $z^{d'}_{wrist} = x^d_{wrist} \times y^{d'}_{wrist}$. The vector x_{base} is chosen as it will not be parallel to x^d_{wrist}, except in very rare circumstances.

To continue, $z^{d'}_{wrist}$ and $y^{d'}_{wrist}$ are in the correct plane but are rotated by an arbitrary angle, θ_6, about x^d_{wrist} away from y^d_{wrist} and z^d_{wrist}. This is shown in Figure 5.7. It is not necessary to compute this angle, θ_6, as will be seen later in this section, as only θ_4 and θ_5 are required. With o^d_{wrist}, x^d_{wrist}, $y^{d'}_{wrist}$ and $z^{d'}_{wrist}$ known in the base frame, the computation of determining the joint angles from this information is known as inverse kinematics. This is the subject of the next section.

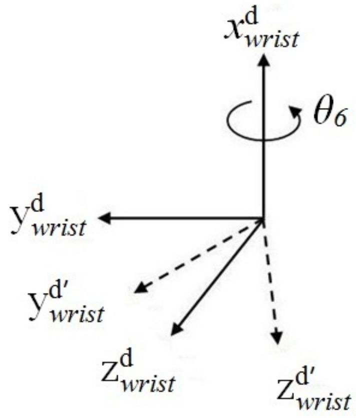

Figure 5.7: Diagram illustrating the extra rotation, θ_6, about the x^d_{wrist} axis

5.3.1 Inverse Kinematics[1]

Kinematic Decoupling

As stated in Section 4.3.3, having the wrist rotate about a fixed point, about two independent axes, greatly simplifies calculations. This is because the inverse kinematics problem may then be separated into two simpler problems: Inverse position kinematics and inverse orientation kinematics. As the wrist gyro-center, the intersection of the two wrist axes, is fixed with respect to the last two joint angles, only the first three joint angles determine its position. Determining these angles is the inverse position kinematics problem. For the inverse orientation kinematics, the first three of the five angles are now known and the problem is to determine the final two joint angles such that the wrist frame is orientated as desired.

Inverse Position Kinematics

Figure 5.8 shows a schematic of the manipulator arm viewed from above, with joints numbered 1 to 3.

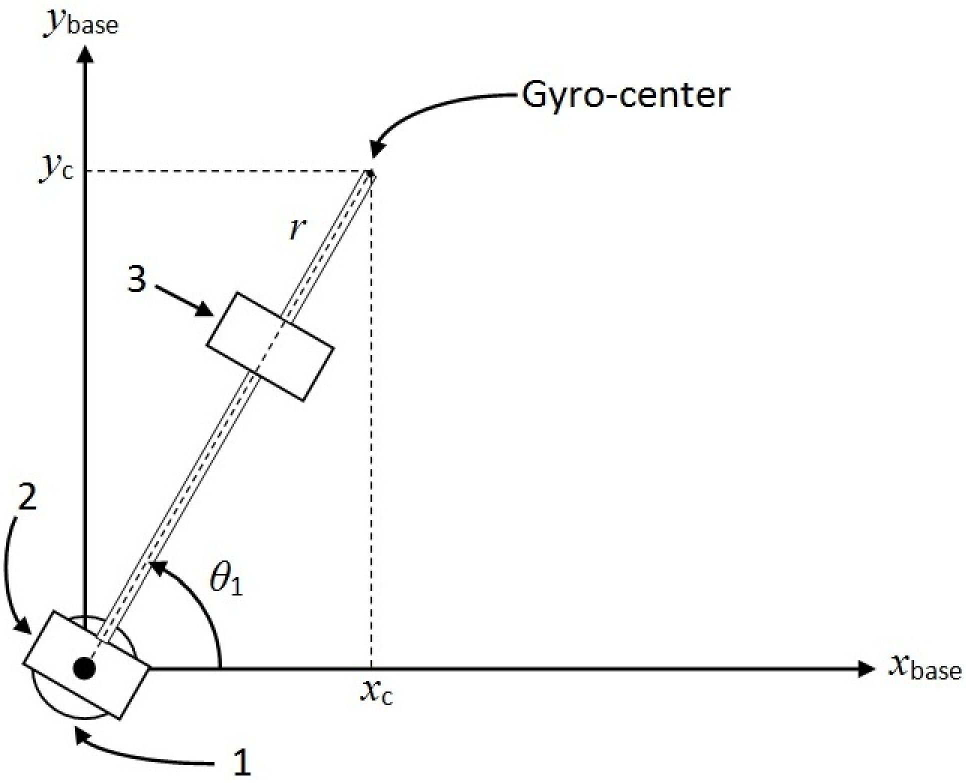

Figure 5.8: Projection of the gyro-center onto the x_{base}-y_{base} plane

---

[1] Much of the information here has been derived from *Spong* et al. [53].

With the gyro-center projected onto the x_{base}-y_{base} plane, the coordinates x_c and y_c can be used to find θ_1:

$$\theta_1 = \arctan\left(\frac{y}{x}\right)$$

In Figure 5.8, r is the line drawn from the origin to the projection of the gyro-center on the x_{base}-y_{base} plane. This line is used in determining θ_2 and θ_3. Figure 5.9 shows the plane formed by the second and third link, the plane r-z_{base}.

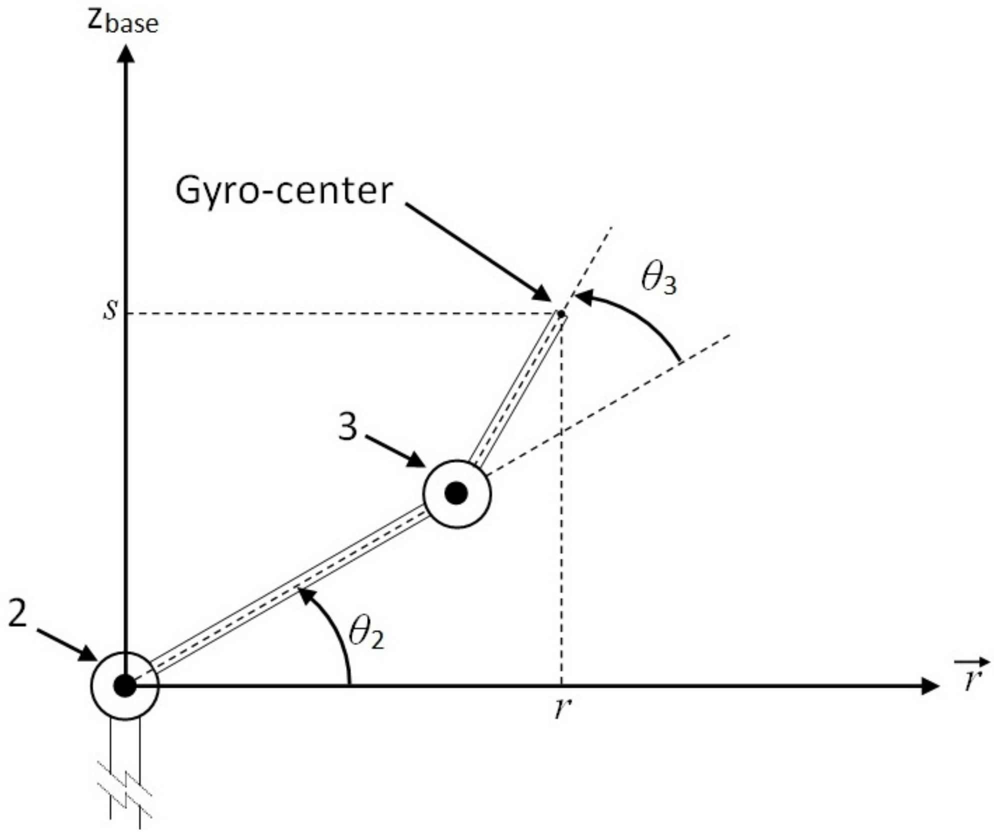

Figure 5.9: Projection of the gyro-center onto the x_{base}-y_{base} plane

From Figure 5.9, it can be seen that

$$\theta_3 = \arctan\left(\frac{\pm\sqrt{1-D^2}}{D}\right)$$

where,

$$D = \frac{r^2 + s^2 - l_2^2 - l_3^2}{2l_2l_3}$$

and l_2,l_3 are the lengths of links 2 and 3 respectively. Following this, θ_2 is obtained from θ_3 by:

$$\theta_2 = \arctan\left(\frac{s}{r}\right) - \arctan\left(\frac{l_3 \sin\theta_3}{l_2 + l_3\cos\theta_3}\right)$$

The two results for θ_3 and the corresponding two results for θ_2 are for the "elbow-up" and "elbow-down" positions [53]. For practical reasons, only solutions for the "elbow-up" position were considered, as joint 3 interfered with the target in the "elbow-down" position.

Inverse Orientation Kinematics

With the desired wrist frame, $o^d_{wrist}x^d_{wrist}y^{d'}_{wrist}z^{d'}_{wrist}$, known in the base frame the transformation matrix due to the six rotations (θ_6, discussed in the beginning of this section, taken into account) the transformation matrix T^0_6 may be formed (see Section B.3, Appendix B). With the first three joint angles solved above, the transformation matrix from the base frame to the third coordinate frame, T^0_3 can also be formed. As $T^0_6 = T^0_3T^3_6$, T^3_6, the matrix describing the transformation due to the final three angles can be found from

$$T^3_6 = \left(T^0_3\right)^{-1} T^0_6 \tag{5.4}$$

As for all such transformation matrices, T^3_6 is of the form

$$T^3_6 = \begin{bmatrix} R^3_6 & o^3_6 \\ 0 & 1 \end{bmatrix}. \tag{5.5}$$

It is the rotational matrix, R^3_6, that is needed to compute the two wrist angles θ_4 and θ_5. The Denavit-Hartenberg parameters of the needle-positioning device are discussed in Section B.3, Appendix B, and just the table of parameters is given here in Table 5.1.

Table 5.1: DH parameters of the needle-positioning device

Frame	d_i (mm)	a_i (mm)	$\alpha_i(°)$	$\theta_i(°)$
1	151	0	90	θ_1
2	0	298	0	θ_2
3	0	0	90	$90 + \theta_3$
4	112	0	-90	θ_4
5	0	0	0	θ_5

It can be seen from Table 5.1 that R_6^3 is formed by the following rotations: -90° about x_3, $-\theta_4$ about y_4, θ_5 about z_5 and finally the arbitrary angle θ_6 about x_5. This may be expressed as

$$R_6^3 = \mathrm{Rot}_{x_3,-90^\circ}\mathrm{Rot}_{y_4,-\theta_4^\circ}\mathrm{Rot}_{z_5,\theta_5^\circ}\mathrm{Rot}_{x_5,\theta_6^\circ} \tag{5.6}$$

where,

$$\begin{aligned} R_6^3 &= \begin{bmatrix} 1 & 0 & 0 \\ 0 & \cos(-90^\circ) & -\sin(-90^\circ) \\ 0 & \sin(-90^\circ) & \cos(-90^\circ) \end{bmatrix} \begin{bmatrix} \cos\theta_4 & 0 & -\sin\theta_4 \\ 0 & 1 & 0 \\ \sin\theta_4 & 0 & \cos\theta_4 \end{bmatrix} \\ &\times \begin{bmatrix} \cos\theta_5 & -\sin\theta_5 & 0 \\ \sin\theta_5 & \cos\theta_5 & 0 \\ 0 & 0 & 1 \end{bmatrix} \begin{bmatrix} 1 & 0 & 0 \\ 0 & \cos\theta_6 & \sin\theta_6 \\ 0 & \sin\theta_6 & \cos\theta_6 \end{bmatrix} \end{aligned} \tag{5.7}$$

so

$$R_6^3 = \begin{bmatrix} \mathrm{c}\theta_4\mathrm{c}\theta_5 & -\mathrm{c}\theta_4 - \mathrm{s}\theta_5\mathrm{c}\theta_6 - \mathrm{s}\theta_4\mathrm{s}\theta_6 & -\mathrm{c}\theta_4 - \mathrm{s}\theta_5\mathrm{s}\theta_6 - \mathrm{s}\theta_4\mathrm{c}\theta_6 \\ \mathrm{s}\theta_4\mathrm{c}\theta_5 & -\mathrm{s}\theta_4\mathrm{s}\theta_5\mathrm{c}\theta_6 + \mathrm{c}\theta_4\mathrm{s}\theta_6 & \mathrm{s}\theta_4\mathrm{s}\theta_5\mathrm{s}\theta_6 + \mathrm{c}\theta_4\mathrm{c}\theta_6 \\ -\mathrm{s}\theta_5 & -\mathrm{c}\theta_5\mathrm{c}\theta_6 & -\mathrm{c}\theta_5\mathrm{s}\theta_6 \end{bmatrix}, \tag{5.8}$$

where $\mathrm{s}\theta$ and $\mathrm{c}\theta$ are short-hand for $\sin\theta$ and $\cos\theta$ respectively. With R_6^3 known from Equation 5.4, the matrix in Equation 5.8 can be used to find the angles θ_4 and θ_5. This is done by

$$\theta_4 = \arctan\left(\frac{r_{21}}{r_{11}}\right)$$

$$\theta_5 = \arctan\left(\frac{-r_{31}}{\sqrt{1-r_{31}^2}}\right)$$

where r_{xy} is the element in the x-th row and y-th column of the matrix R_6^3.

The five angles for the five joints of the needle-positioning arm are now known and the needle can be positioned and orientated to align as desired with the target.

Chapter 6

Software: Vision Application

The computer vision theory discussed in Chapter 3 was applied in practice by computer code written in *Python*. This code, which comprises the software system of the thesis, was implemented on the images captured by the C-arm fluoroscopic imaging device. This software is the subject of the chapter.

This chapter is structured as per the processes that make up the operating of the system, namely the calibration and targeting processes (discussed in Section 4.1). As the operator of the system will be making use of a GUI to implement the software algorithms, the GUI is also discussed throughout. The algorithms are discussed in the order that they are invoked by the user, via the GUI.

6.1 Calibration Procedure

The software for this procedure uses the two images of the calibration object as input. These are the images taken with the C-arm at 0° and 20°. The user captures an image of the calibration object and observes the C-arm screen to see that, firstly, all the metal spheres appear in the image, and secondly, that the sides of the calibration object are approximately parallel to the adjacent sides of the screen. If the user is satisfied with the image, the image is saved to a USB memory stick. With the USB memory stick inserted into the computer running the software program, the user may open the calibration images via the GUI.

The user opens the images by clicking the “Choose Calibration Object Image” buttons and locating the required images on the memory stick. Following the selection of the images, the software crops the image to display only the C-arm viewing circle, as shown in Figure 6.1.

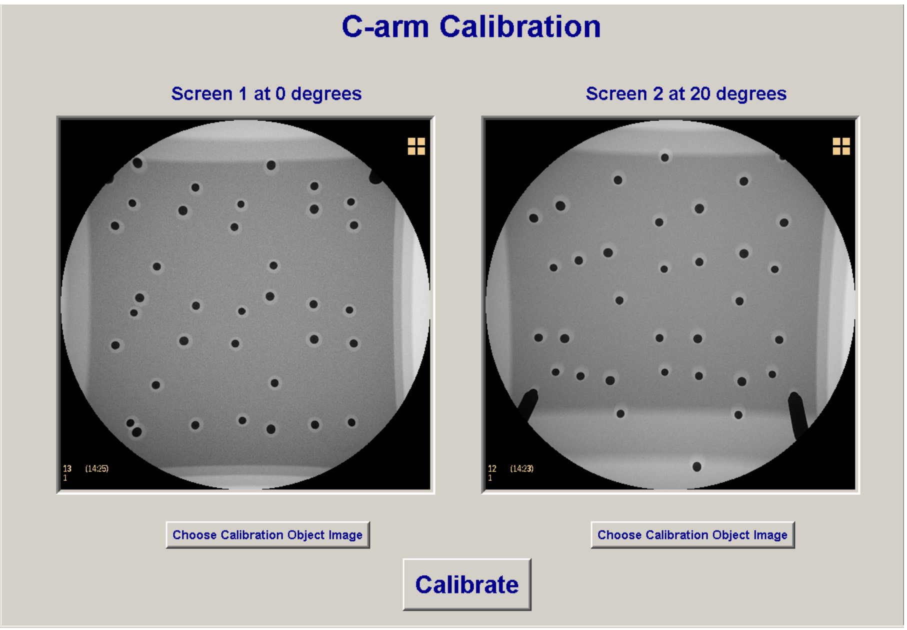

Figure 6.1: Screen shot of the GUI following the selection of the calibration object images

6.1.1 Metal Spheres Locating

By clicking the "Calibrate" button the user invokes the calibration algorithm, which will use the selected images. Firstly, the calibration object's metal spheres' pixel coordinates need to be located in each image. This was done by the following steps:

- Convert image to grayscale image
- Threshold image such that only metal spheres remain in black, with background white
- Apply *OpenCV* function *Canny* to locate all edges in the image
- Apply *OpenCV* function *FindContours* to locate all contours in the image
- Go through all contours fit a circle to each using *MinEnclosingCircle* function of *OpenCV*
- Ignore any circles found outside of viewing circle and with too large or small a radius

OpenCV is an open source computer vision library written in C/C++ and its functions can be called using *Python*. The threshold value is constant and was determined by experimenting with different values on the C-arm images.

Canny uses the Canny edge detection operator to detect all edges in the image. These edges are used by the *FindContours* function to locate all closed contours in the image and saves them as a vector of points. The *MinEnclosingCircle* function can then fit a circle to these points, by returning a list with all circle center coordinates and their corresponding radii. The center coordinates and radii can be checked and the circles filtered such that only the metal spheres remain. The steps of finding the circles are shown visually in Figure 6.2. The metal spheres located had an average radius of 12.17 pixels. A function written, called *FindCirclesCannyEdge* implements the above steps by calling the functions and setting their parameters correctly.

6.1.2 Circle Sorting

With the pixel coordinates known for each metal sphere centre, each centre is assigned a world coordinate. Figure 4.7 in Section 4.3.2, Chapter 4, showed the distinctive lines formed by the spheres of the calibration object. A matrix of the world coordinates is created in *Python*, with each row containing the world coordinates of the spheres which are in a line in the calibration object. The sphere centres found in the images are sorted into another matrix in the same order as the matrix with the world coordinates.

The algorithm for sorting the sphere pixel centres is as follows:

1. Go through all sphere centres and find the 5 spheres with the lowest x coordinates
2. Remove these centres and place them in a row in the sorted matrix
3. Sort this row according to the y coordinates from smallest to largest
4. Return to step (1) and repeat

6.1.3 Distortion Correction

As discussed in Section 3.2.4, images taken with the C-arm fluoroscope are subjected to radial distortion. Thus the center coordinates found for the metal spheres need to be corrected for this distortion, using the model introduced in Section 3.2.4. This model was implemented using existing code found in [54]. The results of the distortion correction algorithm is shown in Figure 6.3. Figure 6.3 shows both the original centre positions and the positions after distortion correction. Corrected distances of up to 24 pixels were found. It can be seen in Figure 6.3 that the distances of the corrected points are greatest towards the corners of the image as expected for pincushion type radial distortion.

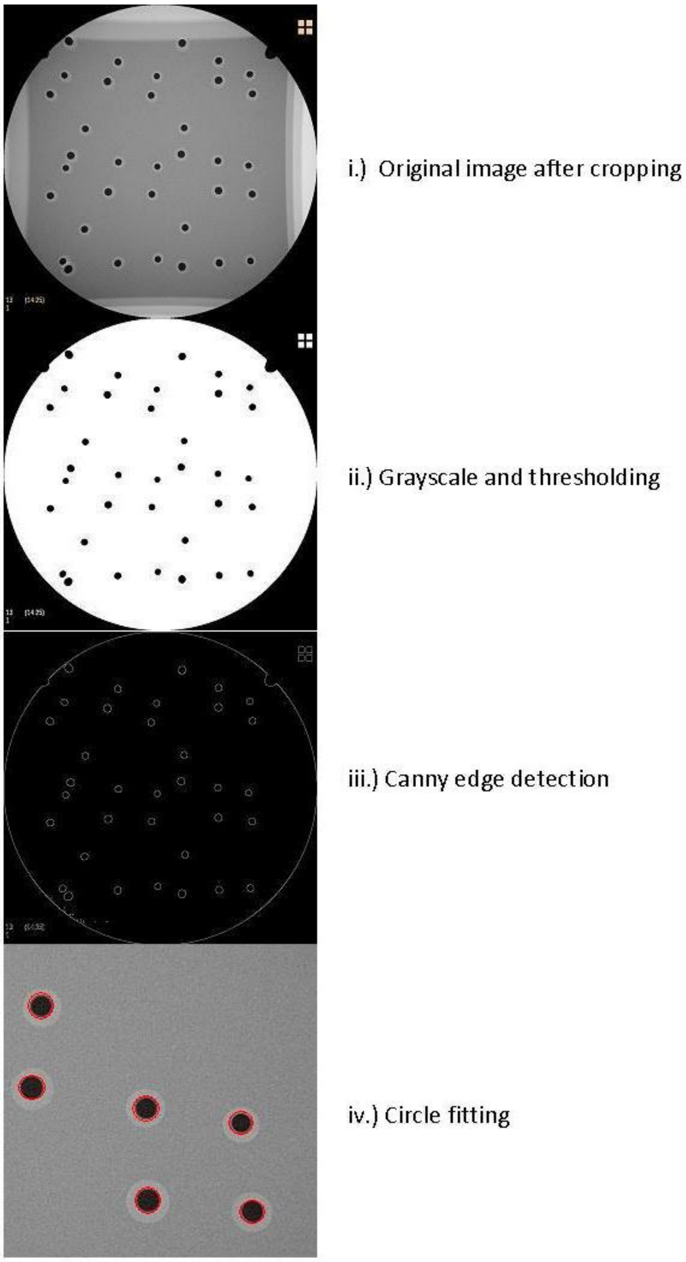
i.) Original image after cropping

ii.) Grayscale and thresholding

iii.) Canny edge detection

iv.) Circle fitting

Figure 6.2: Procedures for locating the metal sphere centres

6.1.4 Calibration

With the marker centres sorted in the same order as the world coordinates and corrected for distortion, the calibration matrices for the two images may be determined. This was done using the function *TriangulateDLT* from [54]. This calibration function is based on the DLT method discussed in Section 3.1.2 . Two functions are also run which check the calibration, namely *StereoCalError* and *TriangulationError*.

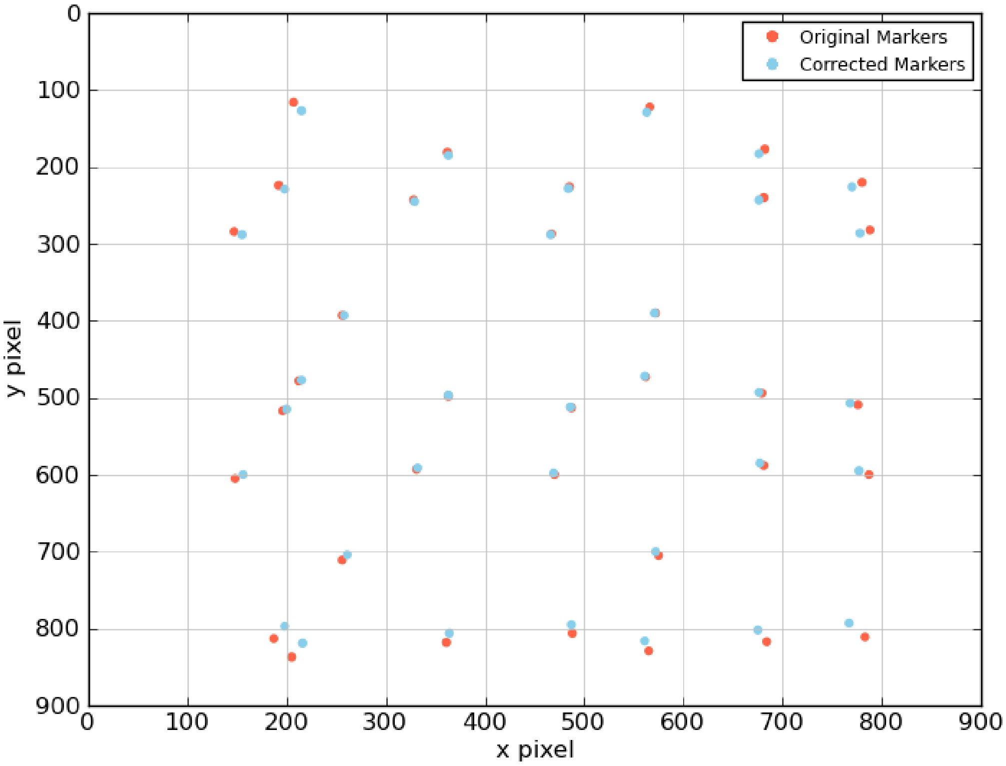

Figure 6.3: Plot showing the original markers and the corrected markers

StereoCalError returns three error measures:

1. Using the two sets of circle centres and calibration matrices, it triangulates the image points and compares these to the world coordinates. The average, maximum, minimum distances and standard deviation, in mm, are returned. These are known as "Ground Truth Errors".

2. The world coordinates are back projected onto the 0° image using the associated calibration matrix. The average, maximum, minimum distances and standard deviation in pixels, between these points and the circle centers for 0°, are returned. These are known as "Camera 1 Backprojection errors".

3. The world coordinates are back projected onto the 20° image using the associated calibration matrix. The average, maximum, minimum distances and standard deviation in pixels, between these points and the circle centers for 20°, are returned. These are known as "Camera 2 Backprojection errors".

If the standard deviation of the ground truth errors is above 2.5 mm, or if the standard deviation of errors (2) or (3) are above 2 pixels the calibration is deemed to be unsuccessful and the calibration process must be repeated.

TriangulationError uses the triangulated points of error 1 and back projects these onto each set of circle center points. The function returns the standard deviations firstly for each image, and secondly for the two images combined. These three errors, in pixels, are then also used to check the success of the calibration. If any of the standard deviations exceed 2 pixels the calibration is considered unsuccessful. Figure 6.4 shows a screenshot of the GUI after a successful calibration procedure. The user may then click “Proceed” to continue to the targeting procedure.

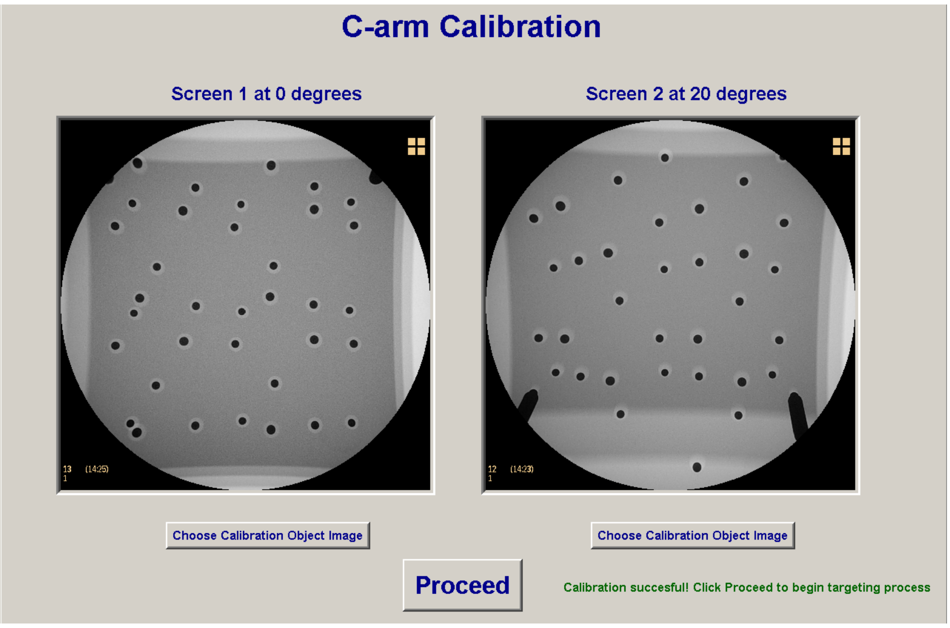

Calibration succesful! Click Proceed to begin targeting process

Figure 6.4: Screen shot of the GUI after a successful calibration

6.2 Targeting Procedure

Following a successful calibration procedure, the user clicks “Proceed” and is taken to the GUI “Targeting” window. Here the user clicks the “Choose Wrist-Target Image” buttons to select the two target images from the USB memory stick.

An algorithm similar to the circle finding algorithm discussed in Section 6.1.1, is applied to the two target images. This algorithm is different only in that it does not filter for circle size or position. Whilst the algorithm finds many circles, including those from noise, it also locates the metal spheres of the wrist. The user is asked by the GUI to click each of the wrist’s four metal spheres in the images. The coordinates of the user’s mouse click is compared with a stored array of all circle centres found in the image. Provided the user’s mouse click is within a 5 pixel radius of the stored circle centre, that stored centre is saved as a wrist marker centre. The user also clicks two points on the target of each image to indicate the desired orientation of the needle. If the spheres and target points are selected correctly, the appropriate messages are displayed to the user to indicate this, as shown in Figure 6.5.

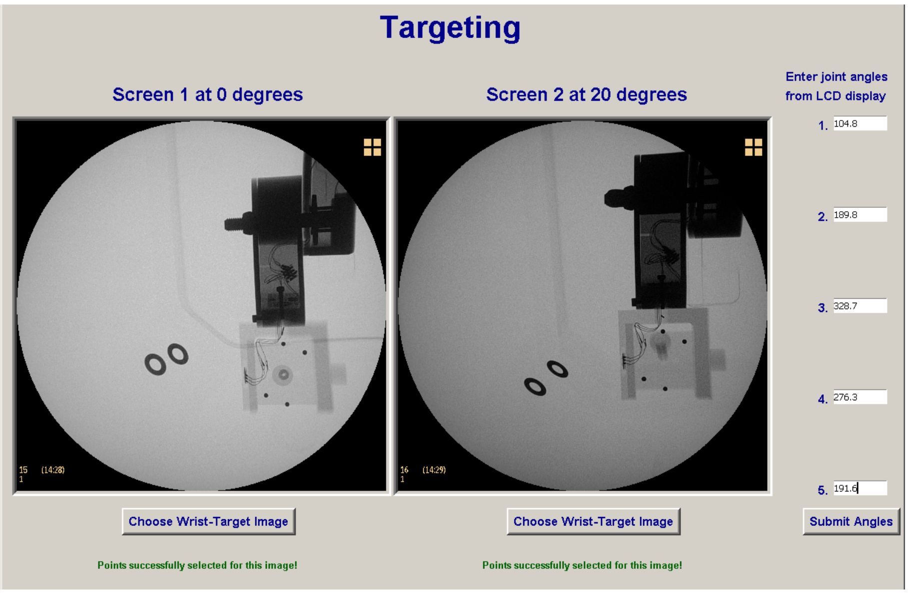
Targeting

Screen 1 at 0 degrees

Screen 2 at 20 degrees

Enter joint angles from LCD display

1. 104.8

2. 189.8

3. 328.7

4. 276.3

5. 191.6

Points successfully selected for this image!

Points successfully selected for this image!

Figure 6.5: GUI screen shot of the targeting procedure once the user has opened the target images and made the necessary selections

Once the user has selected the wrist markers, a function called *FindGyroCentre* locates the pixel coordinates of the wrist gyro-centre in each image. These centres and the marker centres located by the user, are undistorted and then triangulated using the *TriangulateDLT* function. With the positions of these coordinates now known in the world coordinate system (see Section 5.2), the axes of the wrist frame are computed with respect to this coordinate system. A function *GetWristFrameInCalibFrame* was written for this purpose. The points on the target selected by the user are also undistorted, triangulated and then transformed to the wrist coordinate frame, using a function *ChangeCoordSystem*. This is in accordance with the discussions in Section 5.2.2.

The next input required from the user following the selection of the markers and target, is the input of the needle positioning device joint angles. These are the angles that the device was set to for the target images. These angles are inputted in the GUI on the right of the GUI window, shown in Figure 6.5. The user then clicks the "Submit Angles" button and is taken to the screen shown in Figure 6.6.

By clicking "GET INSERTION ANGLES", a function called *GoToBaseFrame* computes the transformation matrix for the input angles, T_{wrist}^{base}, dis-

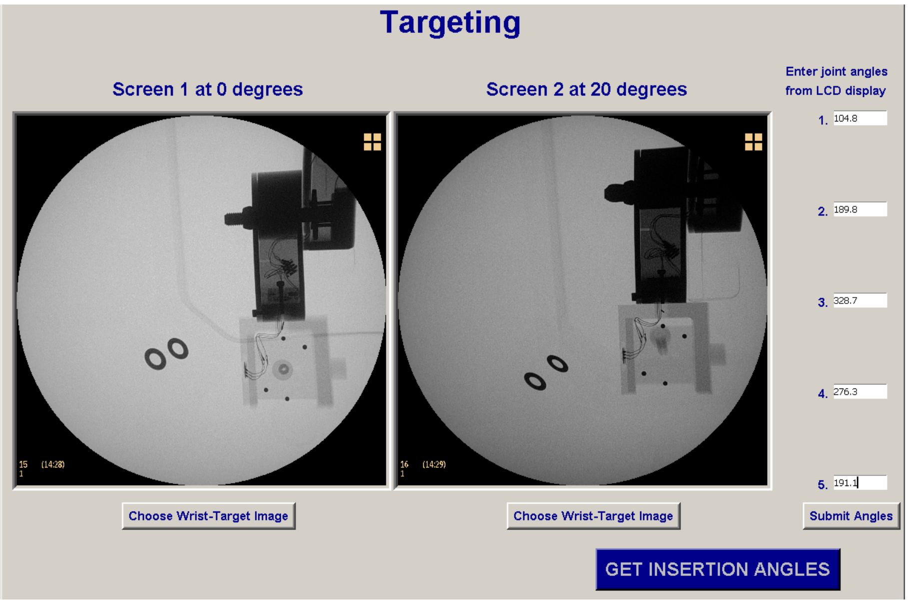

Enter joint angles from LCD display

1. 104.8
2. 189.8
3. 328.7
4. 276.3
5. 191.1

Figure 6.6: GUI screen shot of the targeting procedure once the user has entered and submitted the initial angles of the gantry

cussed in Section 5.2.3. This matrix is used to transform the points from the wrist frame to the base frame. Finally, the user clicks the "Get insertion angles" button and the target angles are returned as shown in the GUI screenshot of Figure 6.7. Functions called *GetArmAngles* and *GetWristAngles* compute the inverse position and orientation kinematics respectively.

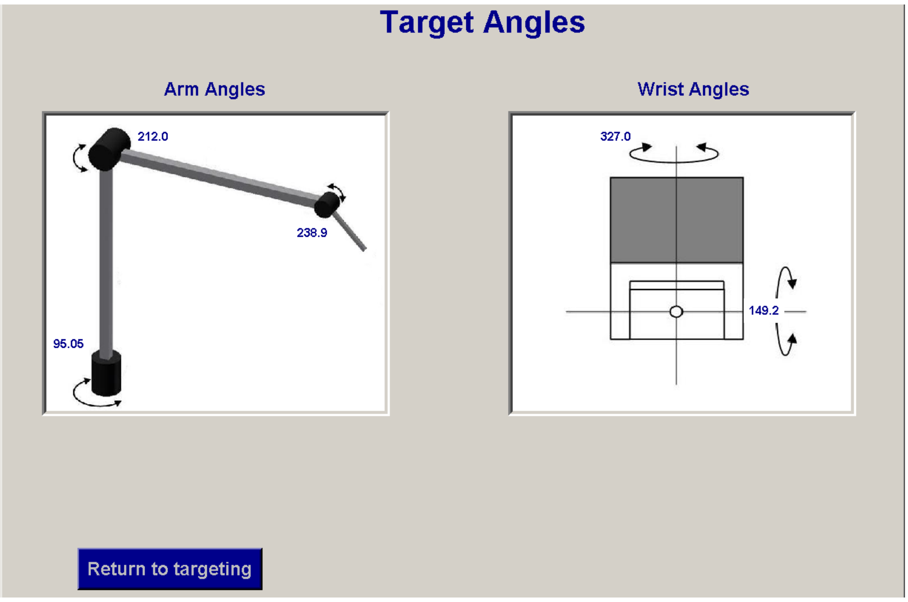

Figure 6.7: GUI screen shot of the targeting procedure displaying the target joint angles

Chapter 7

Testing and Results

This chapter discusses the test procedures performed and the subsequent results obtained. The testing consisted of firstly targeting phantom test objects and then a porcine kidney. Two different phantoms were used. Tests were performed on the first phantom for repeatability and accuracy. The second phantom represented a kidney more closely and was used to simulate a PCNL procedure. Finally, a porcine kidney was used to test the system with an anatomical target, again simulating a PCNL procedure. Due to limited access to the operating theatre and C-arm, a high number of tests was not possible. However, it is believed that the tests were sufficient to ascertain the functionality of the system.

All tests were performed in theatre using a *Philips BV Pulsera* C-arm fluoroscopy imager. The theatre room setup and testing procedure are introduced first followed by the tests and results. The chapter is concluded with a discussion of the sources of error.

7.1 Theatre Room Setup and Testing Procedure

The theatre room setup for the testing is best conveyed by the photograph in Figure 7.1. All the components used during the testing procedures are shown in this figure. The phantoms will be elaborated on in Sections 7.2.1 and 7.2.4.

The steps making up the testing procedure are shown in Figure 7.2. Precise locating of the needle-positioning device relative to the C-arm is not required, provided the device is close enough such that the calibration object falls within the device's work volume. During testing, the needle-positioning device was placed with its base in line with the calibration object. Once a successful calibration procedure was performed, yellow markers (stickers) were placed on the bed at the corners of the calibration object before removing it. This way, for any further imaging the position of the calibrated volume relative to

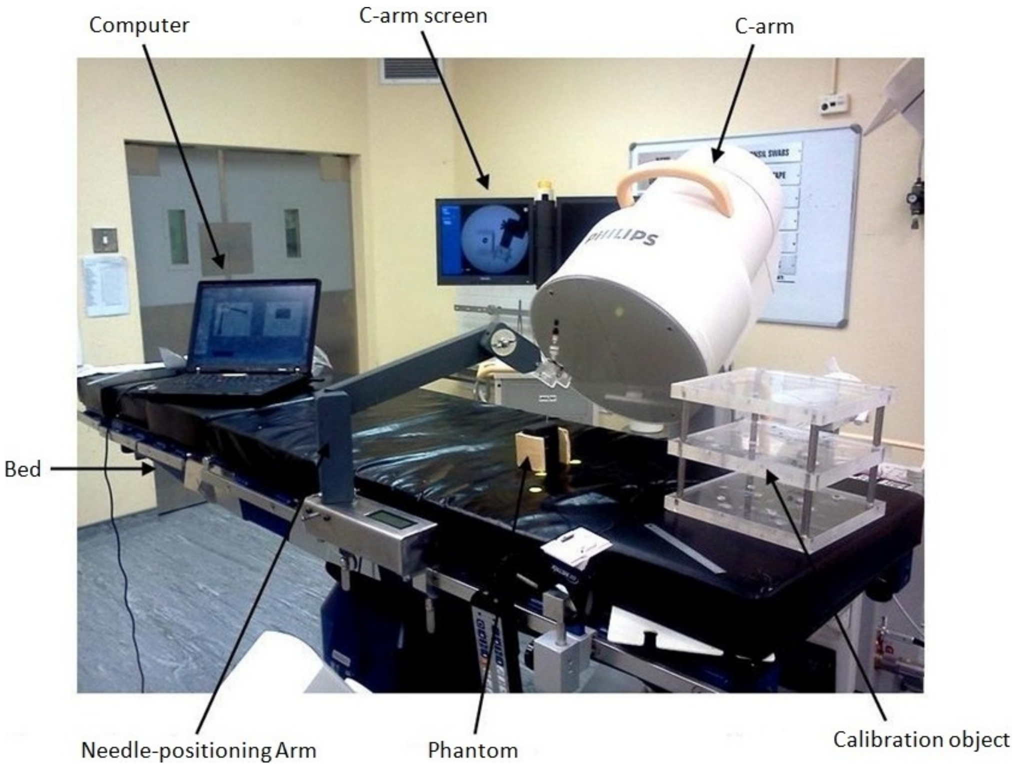

Figure 7.1: Photograph of the theatre room testing setup showing the essential components

the needle-positioning device is known. The surgeon operating decides if the insertion was successful or not, by further imaging for instance.

7.2 Phantom Tests

These tests were implemented, firstly, with a phantom (referred to as *phantom 1*) to test for accuracy and repeatability, and secondly using a phantom (referred to as *phantom 2*) to represent a PCNL procedure. Two kinds of repeatability tests were performed with phantom 1. The first, referred to as "Repeatability Tests 1", consisted of the entire operating process (see Figure 7.2) from calibration to targeting and insertion. The second, referred to as "Repeatability Tests 2", consisted of performing the calibration procedure only once, followed by a series of targeting tests. Accuracy tests were performed by calibrating once and then using a progressively smaller test object for each targeting procedure.

7.2.1 Phantom 1

This phantom consisted of a sponge, with two metal washers embedded in it, and a wooden frame. The centres of the washers create the target vector for

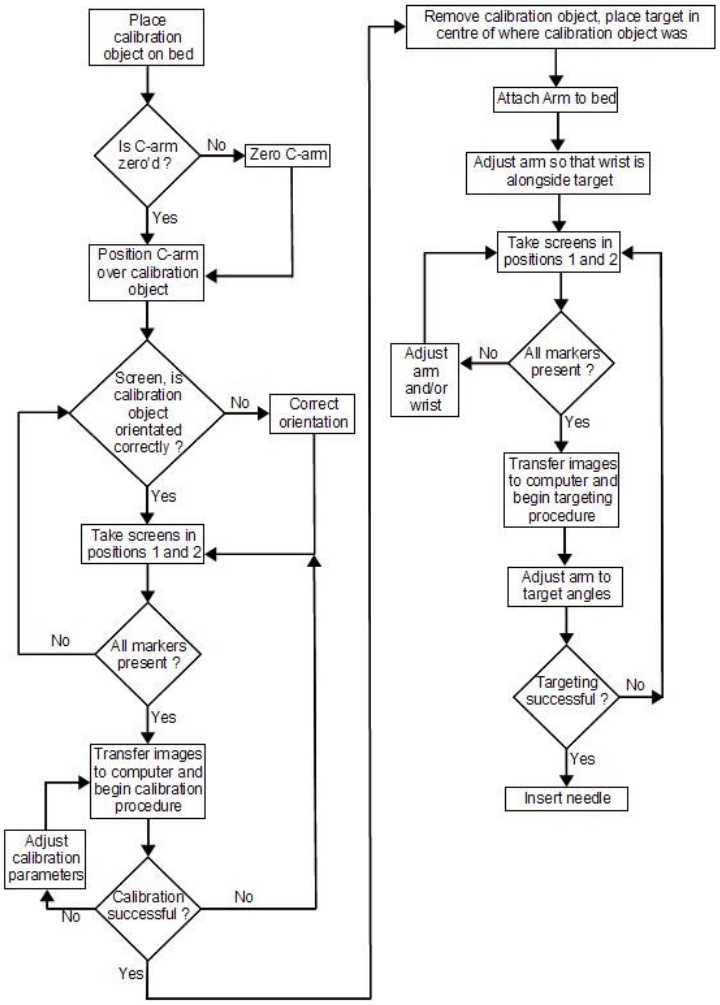

Figure 7.2: Operating process map

the needle, whilst the user sets the distance away from the first washer for the position of the wrist gyro-centre. This distance for the gyro-centre is along the target vector. The sponge was necessary to hold the washers, whilst also allowing the needle to pass through. The sponge is also translucent in the C-arm images as is necessary. Finally, the wooden frame is to support the sponge by keeping it in place and not allowing it to deform or shift when the needle is inserted. Wood was used as it too is translucent in the C-arm images. Figure 7.3 shows a photograph and a CAD model of the phantom.

As slices had to be cut into the sponge to place the washers, following an insertion the sponge could be opened at these slices to see if the needle had passed through both washers. This would deem a test successful.

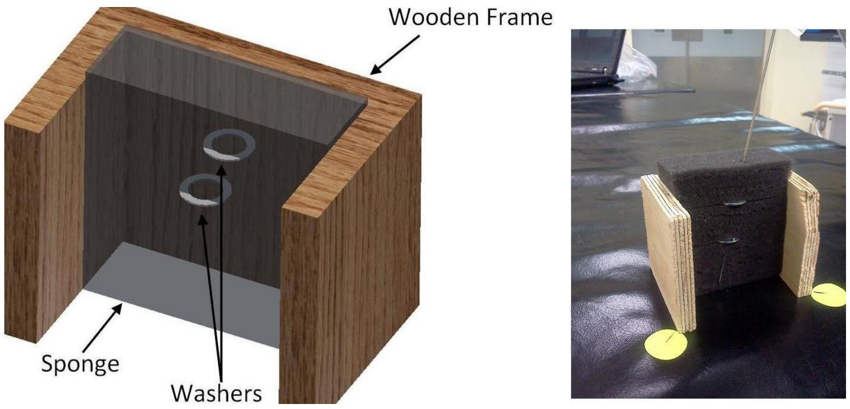

Figure 7.3: CAD model (left) and photograph of phantom 1 used as a test object

7.2.2 Repeatability Tests

The results of the two repeatability tests, introduced at the beginning of this section, are presented here.

Repeatability Tests 1

The entire operating process was performed three times with the target object unchanged in position. Washers with a 8 mm inner diameter were used. A 10 mm vertical and 3 mm horizontal offset was present between the washers. The results of each test is presented in Tables 7.1, 7.2 and 7.3. The errors listed here and in subsequent tables in this chapter were introduced in Section 6.1.4, Chapterchp:vision. Complete tables, including the minimum and maximum values can be found in Appendix D.

Table 7.1: Results of the first repeatability test

TEST 1	**Calibration Errors**		
	Camera 1 Back-projection (pixels)	Camera 2 Back-projection (pixels)	Ground Truth (mm)
Mean	1.2	1.5	0.9
Standard Deviation	0.6	0.9	0.6
	Triangulation Errors		
	Camera 1 Back-projection (pixels)	Camera 2 Back-projection (pixels)	Cameras Combined (pixels)
Mean	1.2	1.4	1.3
Standard Deviation	0.6	1.0	0.8
	Insertion		
Status	Successful		

Table 7.2: Results of the second repeatability test

TEST 2	**Calibration Errors**		
	Camera 1 Back-projection (pixels)	Camera 2 Back-projection (pixels)	Ground Truth (mm)
Mean	1.2	1.9	1.1
Standard Deviation	0.7	1.0	1.2
	Triangulation Errors		
	Camera 1 Back-projection (pixels)	Camera 2 Back-projection (pixels)	Cameras Combined (pixels)
Mean	1.2	1.2	1.2
Standard Deviation	0.7	0.6	0.7
	Insertion		
Status	Successful		

Table 7.3: Results of the third repeatability test

TEST 3	**Calibration Errors**		
	Camera 1 Back-projection (pixels)	Camera 2 Back-projection (pixels)	Ground Truth (mm)
Mean	1.2	2.8	1.0
Standard Deviation	0.7	1.7	0.7
	Triangulation Errors		
	Camera 1 Back-projection (pixels)	Camera 2 Back-projection (pixels)	Cameras Combined (pixels)
Mean	1.2	1.6	1.4
Standard Deviation	0.7	0.8	0.8
	Insertion		
Status	Successful		

As can be seen in the tables above, a successful needle insertion was performed in each test with the 8 mm diameter target. It can be seen, in general, the errors were greater in camera 2, where the C-arm was set to 20°. The average calibration and triangulation errors for the two cameras are shown in the charts in Figure 7.4. Whilst the averages for the set of values of the calibration and triangulation errors were within the same order of magnitude for cameras 1 and 2, the difference in standard deviations for the set of values was far more pronounced. For camera 1, the standard deviations in the set of calibration and triangulation errors were both 0.002 pixels. For camera 2, the standard deviations in the set of calibration and triangulation errors were 0.127 and 0.027 pixels, respectively.

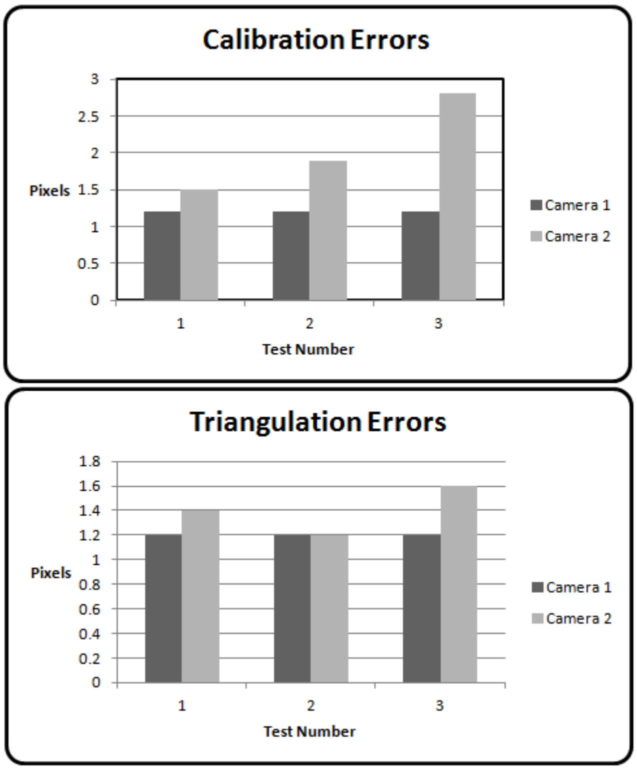

Figure 7.4: Bar charts showing the average calibration errors (top) and average triangulation errors (bottom) for cameras 1 and 2

The source of this greater variance of errors in camera 2 was believed to have resulted from a variation in the distortion of points depending on their distance from the C-arm lens. Points further away from the lens tended to distort more than those closer. In camera 1, with the lens directly above the object, calibration spheres on the same level are the same distance from the lens. However, in camera 2, as the C-arm is at an angle of 20°, points on the same level of the calibration object are not at equal distances from the C-arm. Hence, a greater variation in error values was observed.

Repeatability Tests 2

For this set of repeatability tests, only one calibration procedure was performed and the targeting process was repeated five times, once for each different position of the target. The five different positions of the target are shown in Figure

7.5, with respect to the position of the calibration object. As before, 8 mm washers were used in the phantom for these tests.

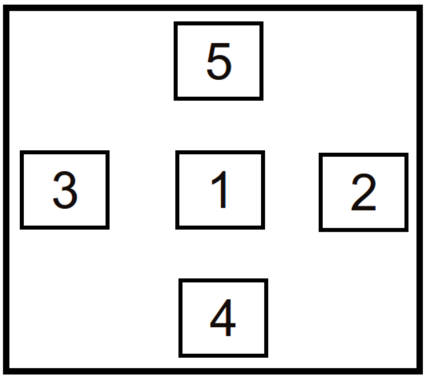

Figure 7.5: The five different phantom positions with respect to the calibration object (border shown)

The calibration errors, triangulation errors and insertion results are shown in Table 7.4.

Table 7.4: Results of the second set of repeatability tests

	Calibration Errors		
	Camera 1 Back-projection (pixels)	Camera 2 Back-projection (pixels)	Ground Truth (mm)
Mean Standard Deviation	1.7 0.9	1.9 0.8	1.0 0.7
	Triangulation Errors		
	Camera 1 Back-projection (pixels)	Camera 2 Back-projection (pixels)	Cameras Combined (pixels)
Mean Standard Deviation	1.7 0.9	1.8 0.7	1.7 0.8

Successful insertions were achieved for each of the five target positions shown in Figure 7.5. It was seen that for the tests where the phantom was positioned along the outside of the boundary of the calibration object (positions 2 to 5), two targeting procedures were necessary to align the needle accurately. This was unless the wrist was positioned directly above the target to begin with. This was believed to have been as a result of distortion in the images becoming increasingly pronounced towards the edges of the images.

7.2.3 Accuracy Tests

For these accuracy tests, a single calibration procedure was performed followed by targeting procedures using the phantom with progressively smaller washers present. Pairs of washers with inner diameters of 7, 5, 4 and 3 mm were used. The results are shown in Table 7.5

Table 7.5: Results of the accuracy tests

	Calibration Errors		
	Camera 1 Back-projection (pixels)	Camera 2 Back-projection (pixels)	Ground Truth (mm)
Mean Standard Deviation	1.7 0.9	1.9 0.8	1.0 0.7
	Triangulation Errors		
	Camera 1 Back-projection (pixels)	Camera 2 Back-projection (pixels)	Cameras Combined (pixels)
Mean Standard Deviation	1.7 0.9	1.8 0.7	1.7 0.8
Washer ⌀ mm	**Insertion**		
7	Successful		
5	Successful		
4	Successful		
3	Unsuccessful		

For each test, the phantom was placed in the centre of the space that was occupied by the calibration object, with the wrist above the phantom. For washers sizes 7 and 5 mm, the needle was inserted through the target on the first attempt. For the 4 mm washer pair, two targeting procedures were necessary as the first attempt did not align the needle correctly. In the case of the 3 mm washer pair, two targeting procedures were not enough to successfully align the needle as desired. For any size target, a series of targeting procedures will continue to align the needle more accurately. However, more than two insertion attempts is not ideal in the case of a real operation on a patient. Thus, after two unsuccessful targeting procedures, the needle insertion for the 3 mm washer pair was considered unsuccessful.

7.2.4 Phantom 2

The components making up this phantom are shown in Figure 7.6.

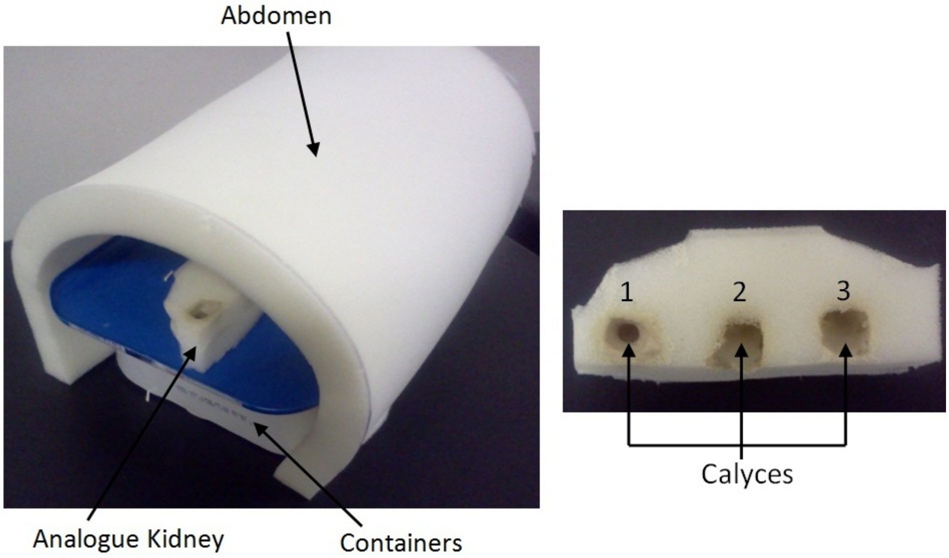

Figure 7.6: Photographs of phantom 2 (left) and the analogue kidney (right) showing the three calyces

The phantom was developed by the collaborating urologist. The abdomen is created by a bent piece of foam to approximate the size of an average patient's abdomen. The abdomen is fixed to two containers which also allow a realistic distance between the foam and the analogue kidney. The analogue kidney is also made from foam with three cavities to act as the kidney calyces. A putty was mixed with contrast fluid so that the calyces appear in the X-ray images. In relation to the hospital bed, calyces one, two and three were made vertical, approximately 45° and horizontal, respectively.

All three of the calyces were successfully targeted. An example of the needle entering a calyx, in this case calyx two, is shown in Figure 7.7

7.3 Porcine Kidney Tests

The test setup for the porcine kidney was the same as that shown in Figure 7.1 except that the phantom was replaced with the porcine kidney as the target. The phantom abdomen (see Figure 7.6) used in the phantom 2 tests was used again with the phantom kidney replaced with a porcine kidney, as can be seen in Figure 7.8.

The porcine kidney was filled with contrast fluid so that they calyces would be visible in the C-arm images. The 0° C-arm image used for the targeting is shown in Figure 7.9 as an example.

The target calyx (see Figure 7.9) was selected via the GUI and the needle successfully inserted into the desired calyx. The success of the insertion was confirmed by the discharge of contrast fluid and by the C-arm image shown in

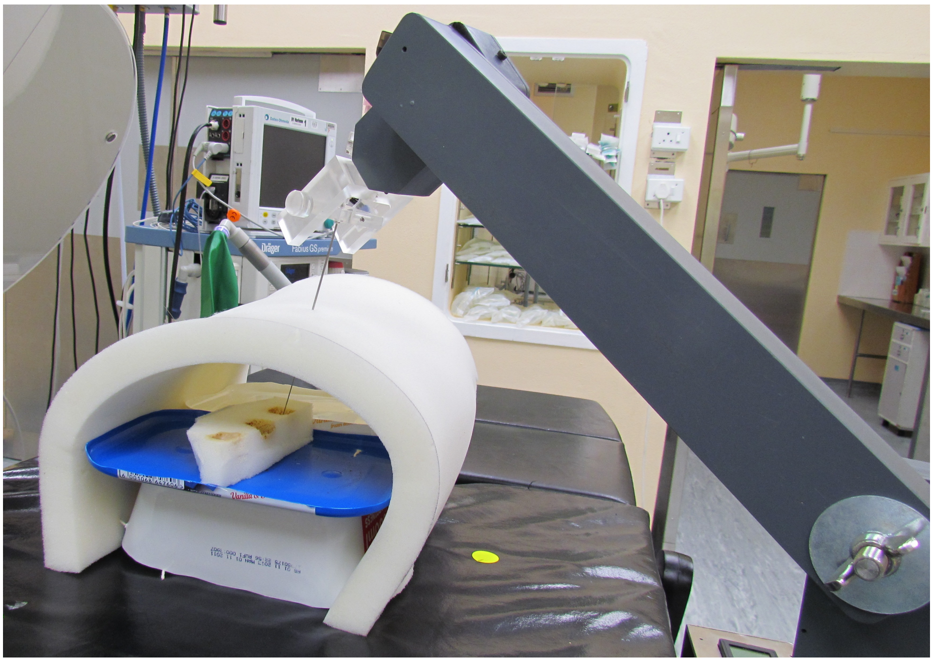

Figure 7.7: Photograph of a successful needle insertion in phantom 2

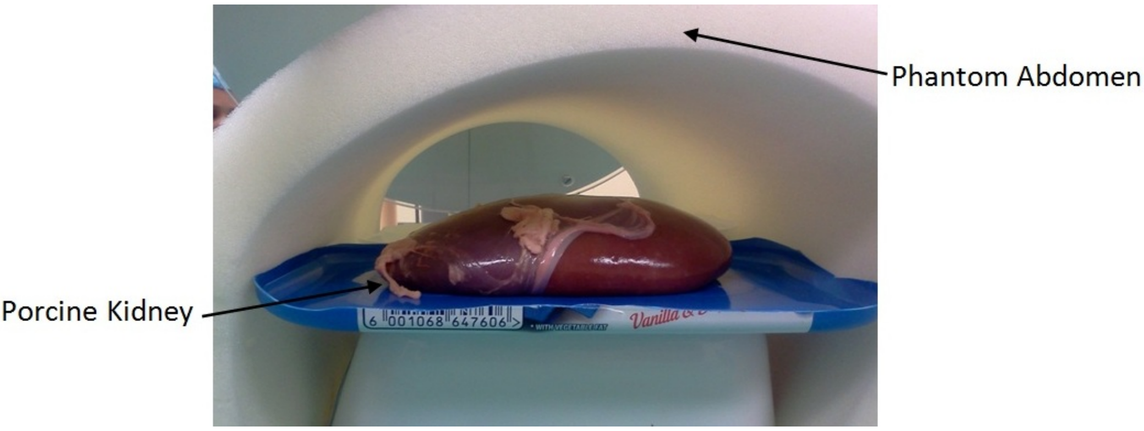

Figure 7.8: Photograph the porcine kidney inside the phantom abdomen

Figure 7.10. Finally, a photograph of the needle inserting the porcine kidney is shown in Figure 7.11.

7.4 Error Propagation

There are a number of different factors which create some error in the positioning of the needle. These errors tend to propagate as each of them contribute an amount of error. These factors are discussed here in this section.

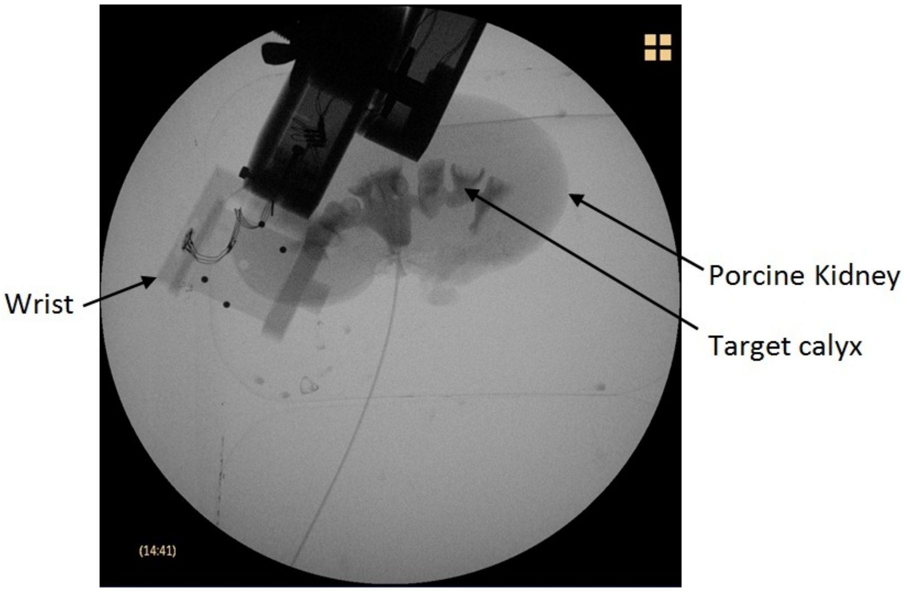

Figure 7.9: C-arm produced image of the porcine kidney and wrist with labels added

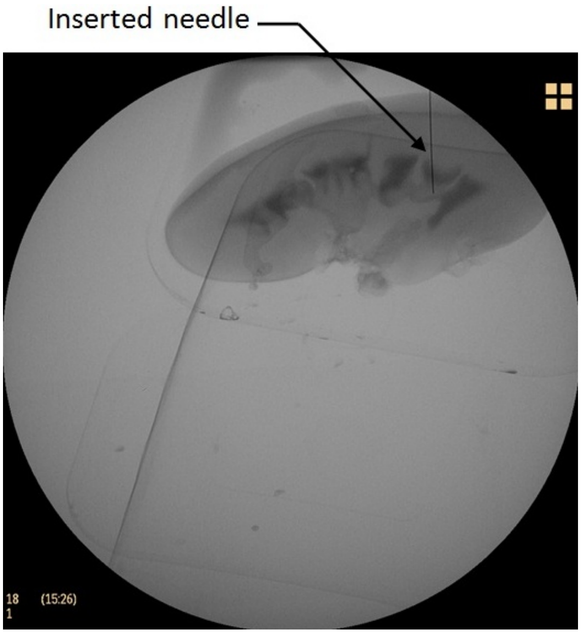

Figure 7.10: C-arm produced image showing the needle inserting the target calyx

7.4.1 C-arm Fluoroscope Movement

The degrees-of-freedom within which the C-arm may move were shown in Figure 4.4, Section 4.3.1. When moving the C-arm along one of these axes of freedom one has to rely on an analogue display of the displacement. Denoted lines on the C-arm every 5°, not unlike those on a ruler, must be aligned with

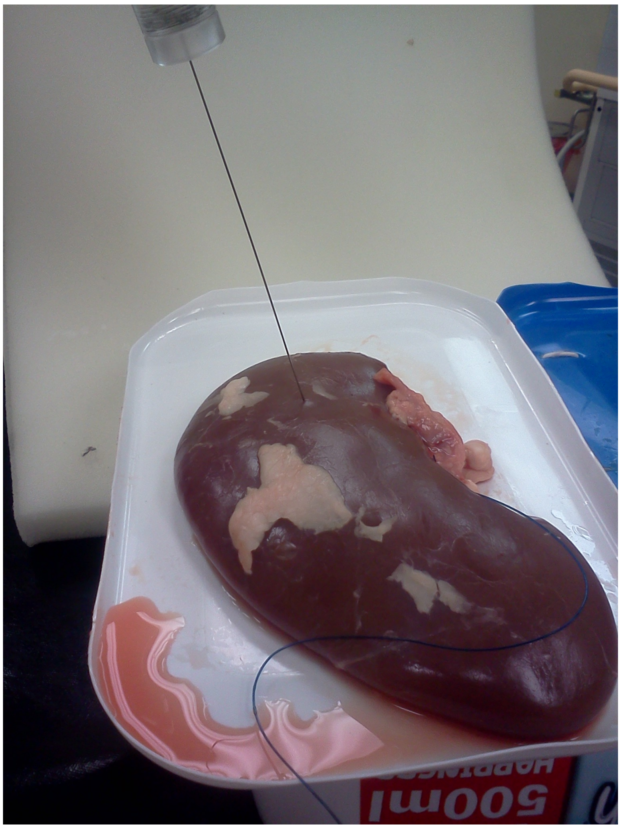

Figure 7.11: Photograph of the needle inserting the porcine kidney

a reference line when rotating the C-arm between the 0° and 20° positions. The denoted lines were a distance away from the reference line and thus could not be easily aligned merely by observation. A ruler was used to align the reference line with the displacement markers, however there is still some error with this alignment. That is, for a given pair of positions used to calibrate, one cannot precisely repeat these positions for the following targeting procedure. Thus there is some error present in the targeting as a result.

7.4.2 Calibration

Some error is introduced during the calibration procedure as a result of distortion in the images produced by the C-arm. The ground truth errors, derived from triangulating the two sets of circle centres found in each of the images and comparing these world points with the calibration object world points, were found to average 1 mm for all the tests done.

7.4.3 Target Selection

During the targeting process, the user makes two selections on each of the images to indicate the desired points through which the needle must traverse.

After making two selections in the 0° image, the user cannot be sure to select the corresponding points in the 20° image. Thus error is introduced during the target selection process.

7.4.4 Needle Positioning Device Joint Angles Resolution

Whilst each potentiometer measuring the corresponding joint angle is a mechanical part essentially with infinite resolution, the *Arduino* microprocessor unit used to measure and display the angles, is a 10-bit digital device. The device thus only measures the potentiometer resistances in integer values between 0 and 1023 ($2^{10} - 1$). The resolution of the angles displayed on the LCD is thus $\frac{270}{1023} = 0.26°$ for the arm joints and $\frac{360}{1023} = 0.35°$ for the wrist joints. The difference in resolution between these sets of joints is because the potentiometers used for the arm had a range of only 270°. These resolutions result in error in the final needle position.

Chapter 8

Conclusions and Recommendations

From the results obtained during the testing of the system, it is possible to conclude to what extent the system meets the objective of the thesis. Recommendations are also made here and finally the thesis is concluded.

8.1 Thesis Objective and Outcomes

The objective of the thesis was to develop a low cost system to aid surgeons in performing percutaneous procedures. Whilst there are many different percutaneous procedures in existence and they may vary largely in how they are performed, almost all involve the initial step of positioning and orientating a needle. This is such that, when inserted, the needle reaches the desired target. The surgeon will now have access to the target and can carry out the necessary steps specific to that procedure.

The system was designed to aid surgeons in this initial step so they may access the target at the first attempt. This will greatly reduce theatre time, patient haemorrhage and radiation exposure resulting from repeated imaging. The system is thus beneficial to the surgeon, patient and theatre staff.

The system was successfully implemented with a standard C-arm fluoroscopy imaging device. The C-arm was used to acquire a stereo pair of images of the target. Using vision theory principles, the necessary position and orientation of the needle was derived from the image pair.

A five degrees-of-freedom robotic arm was developed to orientate and position the needle, as desired by the surgeon. The surgeon operates the system, via a GUI, by inputting the raw C-arm images and selecting points on the images. These selections are used to indicate the target and required entry angle.

The results obtained through testing in theatre were acceptable, where a mean back-projection error of 1.46 pixels, a mean ground truth error of 1 mm and a needle insertion accuracy of 2 mm were recorded. The specifications listed in Section 4.2, Chapter 4 where all adhered to. The prototype system was thus considered to have met the objectives.

8.2 Recommendations

There are a number of areas of improvement for the system which will ultimately lead to a more accurate needle insertion. Beginning with the calibration process, the distortion correction procedure in particular can be further refined. Research into the polynomial used in the lens distortion model, discussed in Section 3.2.4, may lead to improved results. Higher degree polynomials have been discussed in the literature. *Broers* et al. investigated using a C-arm as a verification tool for orthopaedic navigation systems in [55]. *Broers* et al. made use of a six degree polynomial to correct the displacement of points of a phantom due to distortion. Whilst a more accurate distortion model is highly desirable, a more complex polynomial will increase computation time. *Chintalapani* et al. performed a statistical analysis of C-arm distortion and found that the distortion was dependent on the C-arm pose [50]. Thus it is recommended that a different distortion model is investigated for the 20° image. Also, as mentioned in the previous chapter, it was observed that markers in the calibration object on different levels were subjected to different amounts of distortion. Thus the distortion correction algorithm could be refined for each level of markers.

Selecting the target points during the targeting procedure was not an issue with the phantom tests, as the centres of the washers are easily visible. However for anatomical structures, once the target points have been selected in the first image, selecting the corresponding points in the second image is highly challenging. It is dependent on the experience of the surgeon, but even so, in some cases it may be very unclear which points in the second image are the corresponding points. A means to automatically detect the corresponding points could improve the system's accuracy.

As mentioned in the previous chapter, the resolution of the angles displayed on the LCD is 0.26° for the arm angles and 0.35° for the wrist angles. This is a result of the 10-bit *Arduino* microprocessor used to measure the resistance from the joint potentiometers. A finer angle resolution will improve accuracy, however if the resolution is too fine the user may have difficulty positioning the arm to the required angle. Using a 12-bit microprocessor is recommended.

A more ergonomic means of moving and securing arms two and three of the needle-positioning device should be investigated. It was found that when securing these arms in their desired angular position, they tended to move slightly when the wingnuts were fastened. This was evident when viewing the LCD screen whilst fastening the wingnuts. It required a certain amount of practice to secure the arms in the desired positions and this ultimately detracts from the user-friendliness of the system.

The process of transferring images from the C-arm computer to the computer running the GUI, via a USB stick, can be further streamlined. It is recommended a USB-to-USB connecter be used to transfer the images directly to the GUI computer.

8.3 Conclusions

The system required at most two targeting procedures to successfully target the 4 mm diameter pair of washers. This implies an accuracy of 2 mm. Existing systems, discussed in Section 2.4.2, such as TRUS [42] and that which was developed by *Corral* et al. [45], reported better accuracies. In tests performed with the TRUS, errors of 0.25 mm were observed. *Corral* et al reported errors of 1.21 mm. The MRI-compatible robot developed by *Hashizume* et al. [44] was only tested on a 2 cm diameter target, which it successfully punctured on all attempts. Whilst the accuracy achieved by the system developed in this thesis is less accurate than some of the systems discussed in Section 2.4.2, this accuracy still allows a range of percutaneous procedures to be implemented. Examples of procedures are needle biopsy, regional anaesthesia, brachytherapy and PCNL. Two pairs of screens will subject the patient and operating team to a minimal amount of radiation when compared to the other percutaneous procedures discussed in Chapter 2. The system was tested on a porcine kidney in addition to a phantom kidney to imitate a PCNL procedure and the results indicated that the system can potentially function in a real procedure, involving an anatomical target.

The time for each test procedure was not systematically recorded, however the time was considered, in general, to be less than traditional techniques. Such techniques in a procedure such as PCNL target access can take up to 40 minutes, depending on the surgeon's experience. The total cost to develop the prototype system was R15 000. This is far less than existing systems. The systems discussed in Section 2.4.2 consist of sophisticated sensors, state of the art actuators and high-end materials. This thesis has presented a system built from common materials, simple electronics and is actuated manually by the surgeon. The software application was developed in *Python* programming language and added no additional costs as this is an open source platform. The system received a positive review from the collaborating urologist and with the recommendations included to refine the prototype, the system will be at a stage where human testing may be confidently carried out.

Appendices

Appendix A

Singular Value Decomposition (SVD)

The SVD's most common application is in the solution of over-determined systems of equations [49], as is the case in this thesis. Given a set of equations such as $A\mathbf{x} = 0$, the set is said to be "over-determined" if there are more equations than unknowns. *Conradie* et al. [17] explain how, if $\mathbf{x}$ is a solution, so is $k\mathbf{x}$, for any non-zero scalar k. The solution can thus only be determined up to a scale. A constraint is placed on the norm of the solution $\mathbf{x}$, $||\mathbf{x}|| = 1$, so as to find this scale. One now would like to find the solution $\mathbf{x}$ that minimises $||A\mathbf{x}||$, subject to $||\mathbf{x}|| = 1$.

Conradie et al. describe the SVD as follows: Let $A = UDV^T$, where U and V are orthogonal matrices, and D is a diagonal matrix with non-negative entries. Now it is $||UDV^T\mathbf{x}||$ that needs to be minimized. As U and V^T are orthogonal, $||UDV^T\mathbf{x}|| = ||DV^T\mathbf{x}||$ and $||\mathbf{x}|| = ||V^T\mathbf{x}||$. Let $V^T\mathbf{x} = \mathbf{y}$, now it is $||Dy||$ that is to be minimised, subject to $||\mathbf{y}|| = 1$. The solution is thus $\mathbf{y} = (0\ ,\ \dots\ ,1)^T$. As $\mathbf{y}$ needs to have a non-zero entry in the last position, $\mathbf{x} = V\mathbf{y}$ is simply the last column of V. To complete, the solution $\mathbf{x}$ is the last column of V, where $A = UDV^T$ is the SVD of A.

Appendix B

Design Calculations

B.1 Link Lengths and Angle Ranges

B.1.1 Needle Position Error Due to Angle Error

Potentiometers are used to measure the angle of each joint of the articulated manipulator (see Section 4.3.3). These potentiometers are assumed to have some error in the value they return and thus there is some error in the position of the needle determined from the potentiometer readings. This section discusses the calculations done to determine the ideal ratio between links two and three to minimise this error. Whilst an error in the needle position also results from the potentiometer measuring the angle of link one, this is not a function of the link length itself, and so is not considered.

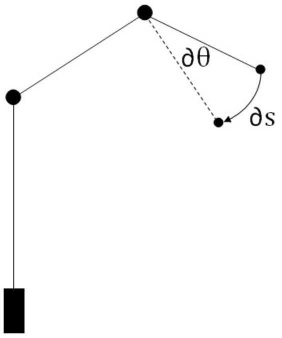

Figure B.1: A schematic showing the error in needle position resulting from an error in the potentiometer reading of joint 3

Figure B.1 shows an error in the measured angle of joint three, $\partial\theta$, and the resulting error in the position of the needle, ∂s. Here, $\partial s = l_3 \partial\theta$, where l_3 is the length of link three. To minimise the error ∂s, l_3 must be minimised.

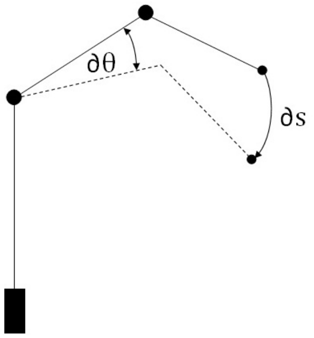

Figure B.2: A schematic showing the error in needle position resulting from an error in the potentiometer reading in joint 2

Figure B.2 shows an error in the measured angle of joint two, $\partial\theta$, and the resulting error in the position of the needle, ∂s. In this case, ∂s is proportional to the position of the needle, i.e. the further the needle is away from joint two, the greater the error in position ∂s.

Thus unlike errors in joint three, errors in the position of the needle from errors in joint two are dependent only on the position of the needle, not the length of link two. Thus the ratio of the length of link two to that of link three must be maximised.

B.1.2 Link Lengths and Angle Ranges

As per specification 8.ii in Table 4.1, the work-volume of the needle- positioning device must at least cover a 300 mm radius half sphere. This half sphere approximates a large patient's abdomen. The work-volume of an articulated manipulator is a function of the link lengths and the range of angles for each joint. Whilst it was determined in Section B.1.1 that the length of link three must be minimised, it must be taken into account that the work-volume of the needle-positioning device will decrease with the length of link three.

Using *Python* and its plotting function *matplotlib*, the work-volume for a given set of link lengths and angle ranges can be plotted. By beginning with a very short link 3, a number of plots were made with the ratio of link 2 to link 3 decreasing slightly for each plot. This process was repeated until the resulting work-volume was judged, visually, to be satisfactory. A work-volume plot done with *matplotlib* is shown in Figure B.3, with the final link lengths and angle ranges. The angle ranges where determined in a similar manner; by observing the plot of the work-volume.

In the plot in Figure B.3, the links are shown in red (position shown for arbitrary angles), the work-envelope by the black dots and the 300 mm radius half sphere in blue. For clarity, the plot was made with the first joint held still and thus the work-volume shown is only for movement of joints 2 and

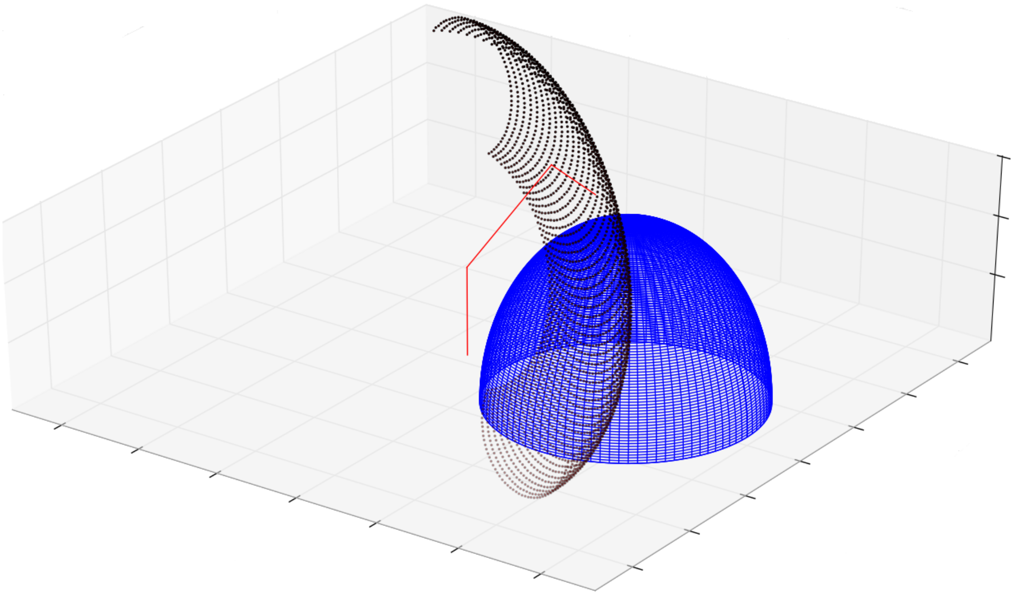

Figure B.3: A plot of the work-volume of the needle-positioning device (the first three arms shown in red), with the first joint held still. The work volume is shown in black whilst the desired volume is blue.

3. It can be seen that the work-volume only covers one half of the desired volume (in blue). This is adequate, however, as the surgeon is able to move the needle-positioning device to the other side of the bed. Also, some points at the edge of the half sphere can also not be reached. It was decided that this was not an issue as the patient can be moved slightly if need be.

The link lengths and angle ranges for the needle-positioning device are shown in Table B.1.

Table B.1: Link lengths and joint ranges of the final design

Link	**Length (mm)**	**Joint**	**Range** (°)
1	151	1	180
2	298	2	150
3	112	3	180
		4	360
		5	100

B.2 Bending Calculation

With the link lengths known, the design of the links could begin. Once the links were designed by CAD, the deflection of the end of link 3, due to the weight of the links, had to be determined to see if the design was stiff enough. Bending calculations were done for the extreme case of both the second and third link being extended outwards, parallel to the bed. For a beam, the following equation holds:

$$EI\frac{d^4w}{dx^4} = q$$

where w is the vertical displacement of the beam, x is the length along the beam and q is the load. The values and the boundary conditions used for this equation are shown in Tables B.2 and B.3.

Table B.2: Values used for the bending calculations

E ($\frac{MN}{m^2}$)	**I** (m^4)	**Link 1 (mm)**	**Link 2 (mm)**
3378.43	2.32×10^{-8}	0.298	0.112

For these calculations, the assumption is made that for each link, the mass is concentrated at the end of the link. E is the modulus of elasticity of PVC and I is second moment of area of a 30 mm square tube, with 3 mm wall thickness. The displacement of the end of the link is then determined.

Table B.3: Boundary conditions for link 2, $x = 0$

$w_{x=0}$	0
$\frac{dw}{dx}_{x=0}$	0
$\frac{d^2w}{dx^2}_{x=0}$	0
$-EI\frac{d^3w}{dx^3}_{x=0}$	F

Table B.3 shows the boundary conditions of link 2 used for the bending calculations. Here F is the weight of link. For link 3 there is a change only for the following condition $\frac{dw}{dx}_{x=0} = 3.587 \times 10^4$. This number is obtained by looking at the slope of link 2 at $x = L$, where the slope is given by $\frac{dw}{dx}$. The end of link 2 displaces vertically by 0.069 mm. For link 3, with its corresponding boundary conditions, it displaces 0.041 mm. Total displacement for the end-effector is the sum of these two displacements: 0.110 mm. This value is considered adequate.

B.3 Denavit-Hartenberg Convention

This section introduces the Denavit-Hartenberg convention, crucial to performing the necessary forward and inverse kinematic calculations for the needle-positioning device. The coordinate systems of the device and the relationships between these systems are discussed first, followed by the Denavit-Hartenberg convention. Much of the theory in this section has been extracted from the book *Robot Modeling and Control* by *Spong, Hutchinson* and *Vidyasagar* [53].

B.3.1 Coordinate Systems of the Needle-positioning Device

Each joint of the positioning device has its own coordinate system associated with it. These coordinate systems are attached to the device at various positions shown in Figure B.4, with joints numbered 1 to 5. When joint i is actuated, coordinate frame $o_i x_i y_i z_i$ experiences a resulting motion. This motion is a rotation about the axis of joint i.

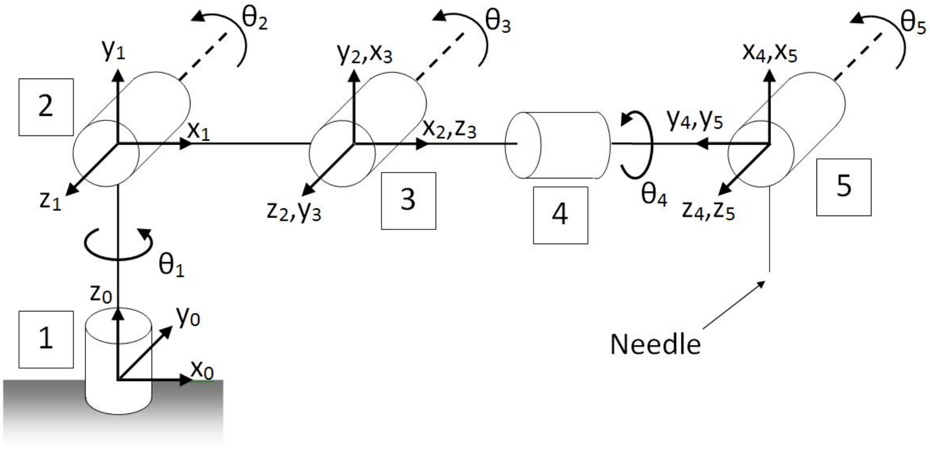

Figure B.4: Coordinate frames attached to the needle positioning-device

Let T_i be the transformation matrix that gives the position and orientation of $o_i x_i y_i z_i$ with respect to $o_{i-1} x_{i-1} y_{i-1} z_{i-1}$. The frame $o_0 x_0 y_0 z_0$, which is attached to the base of the device, is referred to as the inertial frame. The matrix T_i varies as a function of θ_i, the revolution of joint i, written as

$$T_i = T_i(\theta_i). \tag{B.1}$$

It can be observed that

$$T^i_{i+n} = T_{i+1}T_{i+2}...T_{i+n-1}T_{i+n}, \tag{B.2}$$

where T^i_{i+n} is the transformation matrix that gives the position and orientation of $o_{i+n}x_{i+n}y_{i+n}z_{i+n}$ with respect to $o_i x_i y_i z_i$. The matrix T^0_5 is thus the matrix that transforms points in the o_5 frame, P^5, to points in the o_0 frame, P^0, by $T^0_5 P^5 = P^0$. The matrix T^0_5 is composed of a rotation, R^0_5, and a translation o^0_5, shown as

$$T^0_5 = \begin{bmatrix} R^0_5 & o^0_5 \\ 0 & 1 \end{bmatrix}. \tag{B.3}$$

B.3.2 Denavit-Hartenberg Convention

The Denavit-Hartenberg convention, or DH convention, is a commonly used convention for selecting frames of reference for a robotic manipulator such as the needle-positioning device of this thesis. In this convention, each transformation matrix T_i is represented as a product of four basic transformations

$$T_i = \text{Rot}_{z,\theta_i}\text{Trans}_{z,d_i}\text{Trans}_{x,a_i}\text{Rot}_{x,\alpha_i} \tag{B.4}$$

where

$$\begin{aligned} T_i &= \begin{bmatrix} c_{\theta_i} & -s_{\theta_i} & 0 & 0 \\ s_{\theta_i} & c_{\theta_i} & 0 & 0 \\ 0 & 0 & 1 & 0 \\ 0 & 0 & 0 & 1 \end{bmatrix} \begin{bmatrix} 1 & 0 & 0 & 0 \\ 0 & 1 & 0 & 0 \\ 0 & 0 & 1 & d_i \\ 0 & 0 & 0 & 1 \end{bmatrix} \\ &\times \begin{bmatrix} 1 & 0 & 0 & a_i \\ 0 & 1 & 0 & 0 \\ 0 & 0 & 1 & 0 \\ 0 & 0 & 0 & 1 \end{bmatrix} \begin{bmatrix} 1 & 0 & 0 & 0 \\ 0 & c_{\alpha_i} & -s_{\alpha_i} & 0 \\ 0 & s_{\alpha_i} & c_{\alpha_i} & 0 \\ 0 & 0 & 0 & 1 \end{bmatrix} \end{aligned} \tag{B.5}$$

$$T_i = \begin{bmatrix} c_{\theta_i} & -s_{\theta_i}c_{\alpha_i} & s_{\theta_i}s_{\alpha_i} & a_i c_{\theta_i} \\ s_{\theta_i} & c_{\theta_i}c_{\alpha_i} & -c_{\theta_i}s_{\alpha_i} & a_i s_{\theta_i} \\ 0 & s_{\alpha_i} & c_{\alpha_i} & d_i \\ 0 & 0 & 0 & 1 \end{bmatrix} \tag{B.6}$$

where s and c are short-hand for sin and cos respectively. The four quantities θ_i, a_i, d_i, α_i are parameters associated with link i and joint i. These four parameters are known as joint angle, link length, link offset and link twist respectively. *Spong, Hutchinson* and *Vidyasagar* discuss these parameters, known as the DH parameters, in detail in [53]. As the needle-positioning device is made up of rotational joints only, θ_i is the only quantity that is a variable. The coordinate frames in Figure B.4 have been assigned in a manner such that each transformation is defined only by these four parameters. This is according to two criteria necessary for the DH convention:

- The axis x_i is perpendicular to the axis z_{i-1}
- The axis x_i intersects the axis z_{i-1}

The DH parameters for the needle-positioning device are shown in Table B.4. From these parameters any transformation matrix, T_i, can be determined.

Table B.4: DH parameters of the needle-positioning device

Frame	d_i (mm)	a_i (mm)	$\alpha_i(°)$	$\theta_i(°)$
1	151	0	90	θ_1
2	0	298	0	θ_2
3	0	0	90	$90 + \theta_3$
4	112	0	-90	θ_4
5	0	0	0	θ_5

Appendix C

Electronics

The electronics of the system is comprised of potentiometers, the *Arduino* microcontroller and the LCD. A schematic showing how these components are connected is shown in Figure C.1.

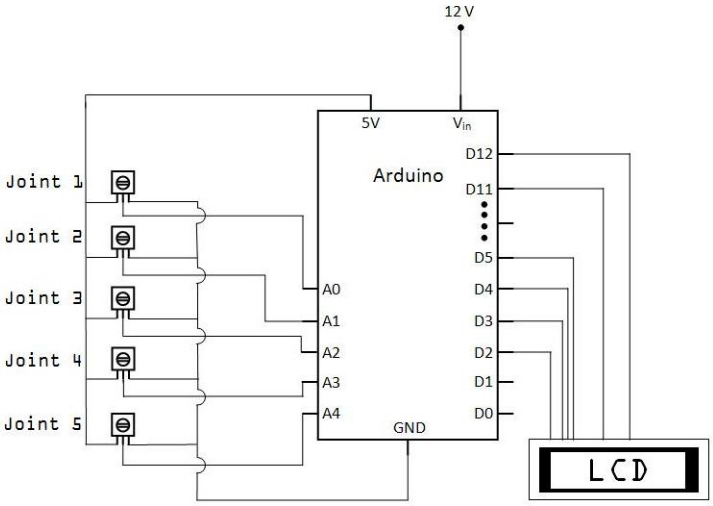

Figure C.1: A schematic of the components making up the electronics of the system

With a potentiometer at each of the five joints, the voltage on the wiper leads can be used to determine the angle of each joint. Each wiper lead is connected to the analogue input pins (A0 to A4) of the *Arduino* which measure the voltage as a value between 0 and 1023. The measured voltage is converted to an angle by multiplying it by $\frac{360}{1023}$.

The code on the *Arduino* performs this multiplication and also controls the display of the LCD screen using the output pins (D0 to D12). The *Arduino* sets the LCD to display each angle as shown in Figure C.2. All code for the *Arduino* is included on the accompanying DVD.

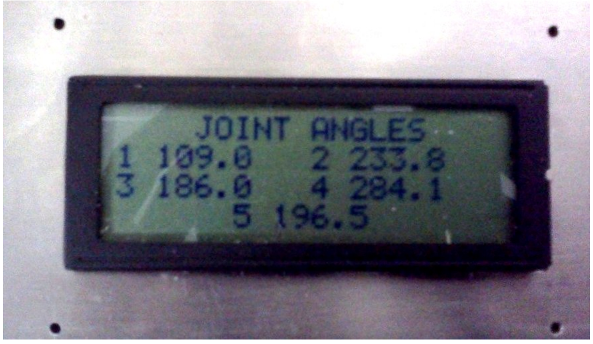

Figure C.2: Photograph of the LCD displaying the joint angles

Appendix D

Complete Results Tables

Table D.1: Results of the first repeatability test

TEST 1			
	Calibration Errors		
	Camera 1 Back-projection (pixels)	Camera 2 Back-projection (pixels)	Ground Truth (mm)
Minimum	0.1	0.4	0.2
Mean	1.2	1.5	0.9
Maximum	2.8	3.9	2.2
Standard Deviation	0.6	0.9	0.6
	Triangulation Errors		
	Camera 1 Back-projection (pixels)	Camera 2 Back-projection (pixels)	Cameras Combined (pixels)
Minimum	0.1	0.1	0.1
Mean	1.2	1.4	1.3
Maximum	2.8	3.9	3.9
Standard Deviation	0.6	1.0	0.8
	Insertion		
Status	Successful		

Table D.2: Results of the second repeatability test

TEST 2			
	Calibration Errors		
	Camera 1 Back-projection (pixels)	Camera 2 Back-projection (pixels)	Ground Truth (mm)
Minimum	0.2	0.3	0.2
Mean	1.2	1.9	1.1
Maximum	2.8	4.8	7.1
Standard Deviation	0.7	1.0	1.2
	Triangulation Errors		
	Camera 1 Back-projection (pixels)	Camera 2 Back-projection (pixels)	Cameras Combined (pixels)
Minimum	0.2	0.3	0.2
Mean	1.2	1.2	1.2
Maximum	2.8	2.8	2.8
Standard Deviation	0.7	0.6	0.7
	Insertion		
Status	Successful		

Table D.3: Results of the third repeatability test

TEST 3			
	Calibration Errors		
	Camera 1 Back-projection (pixels)	Camera 2 Back-projection (pixels)	Ground Truth (mm)
Minimum	0.4	0.6	0.2
Mean	1.2	2.8	1.0
Maximum	3.2	7.6	3.1
Standard Deviation	0.7	1.7	0.7
	Triangulation Errors		
	Camera 1 Back-projection (pixels)	Camera 2 Back-projection (pixels)	Cameras Combined (pixels)
Minimum	0.4	0.5	0.8
Mean	1.2	1.6	1.4
Maximum	3.2	3.4	3.4
Standard Deviation	0.7	0.8	0.8
	Insertion		
Status	Successful		

Table D.4: Results of the second set of repeatability tests

	Calibration Errors		
	Camera 1 Back-projection (pixels)	Camera 2 Back-projection (pixels)	Ground Truth (mm)
Minimum	0.1	0.6	0.2
Mean	1.7	1.9	1.0
Maximum	3.8	3.8	3.0
Standard Deviation	0.9	0.8	0.7
	Triangulation Errors		
	Camera 1 Back-projection (pixels)	Camera 2 Back-projection (pixels)	Cameras Combined (pixels)
Minimum	0.2	0.7	0.2
Mean	1.7	1.8	1.7
Maximum	3.8	3.3	3.8
Standard Deviation	0.9	0.7	0.8

Table D.5: Results of the accuracy tests

	Calibration Errors		
	Camera 1 Back-projection (pixels)	Camera 2 Back-projection (pixels)	Ground Truth (mm)
Minimum	0.2	0.6	0.2
Mean	1.7	1.9	1.0
Maximum	3.8	3.9	3.0
Standard Deviation	0.9	0.8	0.7
	Triangulation Errors		
	Camera 1 Back-projection (pixels)	Camera 2 Back-projection (pixels)	Cameras Combined (pixels)
Minimum	0.2	0.5	0.2
Mean	1.7	1.8	1.7
Maximum	3.8	3.3	3.8
Standard Deviation	0.9	0.7	0.8
Washer ⌀ mm	**Insertion**		
7	Successful		
5	Successful		

4	Successful
3	Unsuccessful

List of References

[1] Zarrabi, A.: Personal interview. September 2010. Tygerberg Hospital, Cape Town.

[2] Lee, S.-L., Lerotic, M., Vitiello, V., Giannarou, S., Kwok, K.-W., Visentini-Scarzanella, M. and Yang, G.-Z.: From medical images to minimally invasive intervention: Computer assistance for robotic surgery. *Computerized Medical Imaging and Graphics*, vol. 34, no. 1, pp. 33 – 45, 2010.

[3] Gupta, S. and Madoff, D.C.: Image-guided percutaneous needle biopsy in cancer diagnosis and staging. *Techniques in Vascular and Interventional Radiology*, vol. 10, no. 2, pp. 88 – 101, 2007.

[4] Jenssen, C. and Dietrich, C.F.: Endoscopic ultrasound-guided fine-needle aspiration biopsy and trucut biopsy in gastroenterology - an overview. *Best Practice and Research Clinical Gastroenterology*, vol. 23, no. 5, pp. 743 – 759, 2009.

[5] Tomiyama, N., Yasuhara, Y., Nakajima, Y., Adachi, S., Arai, Y., Kusumoto, M., Eguchi, K., Kuriyama, K., Sakai, F., Noguchi, M., Murata, K., Murayama, S., Mochizuki, T., Mori, K. and Yamada, K.: CT-guided needle biopsy of lung lesions: A survey of severe complication based on 9783 biopsies in Japan. *European Journal of Radiology*, vol. 59, no. 1, pp. 60 – 64, 2006.

[6] Quinn, S.F., Sheley, R.C., Nelson, H.A., Demlow, T.A., Wienstein, R.E. and Dunkley, B.L.: The role of percutaneous needle biopsies in the original diagnosis of lymphoma: A prospective evaluation. *Journal of Vascular and Interventional Radiology*, vol. 6, no. 6, pp. 947 – 952, 1995.

[7] Paoli, A., Pacelli, Q.F., Toniolo, L., Miotti, D. and Reggiani, C.: Latissimus dorsi fine needle muscle biopsy: A novel and efficient approach to study proximal muscles of upper limbs. *Journal of Surgical Research*, vol. 164, no. 2, pp. 257 – 263, 2010.

[8] Warman, P. and Nicholls, B.: Ultrasound-guided nerve blocks: efficacy and safety. *Best Practice and Research Clinical Anaesthesiology*, vol. 23, no. 3, pp. 313 – 326, 2009.

[9] Clark, L. and Varbanova, M.: Regional anesthesia in trauma. *Advances in Anesthesia*, vol. 27, no. 1, pp. 191 – 222, 2009.

[10] Van Limbergen, E. and Mazeron, J.: *Breast cancer.* The GEC ESTRO Handbook of Brachytherapy, 2002.

[11] Gerbaulet, A., Pötter, R. and Haie-Meder, C.: *Cervix cancer.* The GEC ESTRO Handbook of Brachytherapy, 2002.

[12] Ash, D.: *Prostate cancer.* The GEC ESTRO Handbook of Brachytherapy, 2002.

[13] van Limbergen, E. and Mazeron, J.: *Skin cancer.* The GEC ESTRO Handbook of Brachytherapy, 2002.

[14] Pötter, R.: *Modern Imaging in Brachytherapy.* The GEC ESTRO Handbook of Brachytherapy, 2002.

[15] Gerbaulet, A., Ash, D. and Meertans, H.: *General Aspects.* The GEC ESTRO Handbook of Brachytherapy, 2002.

[16] Miller, N.L., Matlaga, B.R. and Lingeman, J.E.: Techniques for fluoroscopic percutaneous renal access. *The Journal of Urology*, vol. 178, no. 1, pp. 15 – 23, 2007.

[17] Conradie, J.: *Fluoroscopy Based Needle-Positioning System for Percutaneous Nephrolithotomy Procedures.* Master's thesis, Stellenbosch University, 2008.

[18] Erinjeri, J.P. and Clark, T.W.: Cryoablation: Mechanism of action and devices. *Journal of Vascular and Interventional Radiology*, vol. 21, no. 8, Supplement 1, pp. S187 – S191, 2010.

[19] Goldberg, S.N., Grassi, C.J., Cardella, J.F., Charboneau, J.W., III, G.D.D., Dupuy, D.E., Gervais, D.A., Gillams, A.R., Kane, R.A., Jr, F.T.L., Livraghi, T., McGahan, J., Phillips, D.A., Rhim, H., Silverman, S.G., Solbiati, L., Vogl, T.J., Wood, B.J., Vedantham, S. and Sacks, D.: Image-guided tumor ablation: Standardization of terminology and reporting criteria. *Journal of Vascular and Interventional Radiology*, vol. 20, no. 7, Supplement 1, pp. S377 – S390, 2009.

[20] Emory Healthcare: www.emoryhealthcare.org. `http://www.emoryhealthcare.org/urology/oncology/prostate-cancer/cryoablation.html`, last visited 20 September 2010. Emory Healthcare.

[21] Eckel, T.S. and Olan, W.: Vertebroplasty and vertebral augmentation techniques. *Techniques in Vascular and Interventional Radiology*, vol. 12, no. 1, pp. 44 – 50, 2009.

[22] Burschka, D., Corso, J.J., Dewan, M., Lau, W., Li, M., Lin, H., Marayong, P., Ramey, N., Hager, G.D., Hoffman, B., Larkin, D. and Hasser, C.: Navigating inner space: 3-D assistance for minimally invasive surgery. *Robotics and Autonomous Systems*, vol. 52, no. 1, pp. 5 – 26, 2005.

[23] Chen, E.H. and Nemeth, A.: Complications of percutaneous procedures. *The American Journal of Emergency Medicine*, vol. 29, no. 7, pp. 802 – 810, 2010.

[24] Siemens Medical [Online]: www.medical.siemens.com. `"http://www.medical.siemens.com"`, last visited 20 September 2010. Siemens Medical.

[25] Perrin, D.P., Vasilyev, N.V., Novotny, P., Stoll, J., Howe, R.D., Dupont, P.E., Salgo, I.S. and del Nido, P.J.: Image guided surgical interventions. *Current Problems in Surgery*, vol. 46, no. 9, pp. 730 – 766, 2009.

[26] Oldman, M. and Nicholls, B.: Imaging techniques and regional anaesthesia. *Current Anaesthesia and Critical Care*, vol. 15, no. 4-5, pp. 255 – 261, 2004.

[27] Marcovich, R., S.A.: Percutaneous renal access: Tips and tricks. *BJU International, Supplement*, vol. 95, no. 2, pp. 78–84, 2005.

[28] Cheung, S. and Rohling, R.: Enhancement of needle visibility in ultrasound-guided percutaneous procedures. *Ultrasound in Medicine and Biology*, vol. 30, no. 5, pp. 617 – 624, 2004.

[29] Park, S. and Pearle, M.S.: Imaging for percutaneous renal access and management of renal calculi. *Urologic Clinics of North America*, vol. 33, no. 3, pp. 353 – 364, 2006.

[30] Ko, R., Soucy, F., Denstedt, J.D. and Razvi, H.: Percutaneous nephrolithotomy made easier: a practical guide, tips and tricks. *British Journal of Urology*, vol. 101, no. 5, pp. 535 – 539, 2008.

[31] Glossop, N., Clearly, K. and Banovac, F.: Needle tracking using the aurora magnetic position sensor. *Proc COAS*, pp. 90 – 92, 2002.

[32] Chan, C., Lam, F. and Rohling, R.: A needle tracking device for ultrasound guided percutaneous procedures. *Ultrasound in Medicine and Biology*, vol. 31, no. 11, pp. 1469 – 1483, 2005.

[33] Howard, M., Nelson, R., Paulson, E., Kliewer, M. and Sheafor, D.: An electronic device for needle placement during sonographically guided percutaneous intervention. *Radiology*, vol. 218, no. 3, pp. 905 – 911, 2001.

[34] Kim, C.W., Lee, Y.-P., Taylor, W., Oygar, A. and Kim, W.K.: Use of navigation-assisted fluoroscopy to decrease radiation exposure during minimally invasive spine surgery. *The Spine Journal*, vol. 8, no. 4, pp. 584 – 590, 2008.

[35] Gomes, P.: Surgical robotics: Reviewing the past, analysing the present, imagining the future. *Robotics and Computer-Integrated Manufacturing*, vol. 27, no. 2, pp. 261 – 266, 2010.

[36] Korb, W., Marmulla, R., Raczkowsky, J., Mhling, J. and Hassfeld, S.: Robots in the operating theatre–chances and challenges. *International Journal of Oral and Maxillofacial Surgery*, vol. 33, no. 8, pp. 721 – 732, 2004.

[37] Systems, I.S.: www.intuitivesurgical.com. Intuitive Surgical, Da Vinci System. Available at: `www.intuitivesurgical.com`

[38] Mohr, F.W., Falk, V., Diegeler, A., Walther, T., Gummert, J.F., Bucerius, J., Jacobs, S. and Autschbach, R.: Computer-enhanced robotic cardiac surgery: Experience in 148 patients. *Journal of Thoracic and Cardiovascular Surgery*, vol. 121, no. 5, pp. 842 – 853, 2001.

[39] Hagn, U., Nickl, M., Jörg, S., Passig, G., Bahls, T., Nothhelfer, A., Hacker, F., Le-Tien, L., Albu-Schffer, A., Konietschke, R., Grebenstein, M., Warpup, R., Haslinger, R., Frommberger, M. and Hirzinger, G.: The DLR MIRO: a versatile lightweight robot for surgical applications. *Industrial Robot: An International Journal*, vol. 35, no. 4, pp. 324 – 336, 2008.

[40] Shoham, M., Burman, M., Zehavi, E., Joskowicz, L., Batkilin, E. and Kunicher, Y.: Bone-mounted miniature robot for surgical procedures: Concept and clinical applications. *IEEE Transactions on Robotics and Automation*, vol. 19, no. 5, pp. 893 – 901, 2003.

[41] Liao, H., Ishihara, H., Tran, H.H., Masamune, K., Sakuma, I. and Dohi, T.: Precision-guided surgical navigation system using laser guidance and 3D autostereoscopic image overlay. *Computerized Medical Imaging and Graphics*, vol. 34, no. 1, pp. 46 – 54, 2010.

[42] Fichtinger, G., Fiene, J.P., Kennedy, C.W., Kronreif, G., Iordachita, I., Song, D.Y., Burdette, E.C. and Kazanzides, P.: Robotic assistance for ultrasound-guided prostate brachytherapy. *Medical Image Analysis*, vol. 12, no. 5, pp. 535 – 545, 2008.

[43] Kobayashi, Y., Onishi, A., Watanabe, H., Hoshi, T., Kawamura, K., Hashizume, M. and Fujie, M.G.: Development of an integrated needle insertion system with image guidance and deformation simulation. *Computerized Medical Imaging and Graphics*, vol. 34, no. 1, pp. 9 – 18, 2010.

[44] Hashizume, M., Yasunaga, T., Tanoue, K., Ieiri, S., Konishi, K., Kishi, K., Nakamoto, H., Ikeda, D., Sakuma, I., Fujie, M. and Dohi, T.: New real-time MR image-guided surgical robotic system for minimally invasive precision surgery. *International Journal of Computer Assisted Radiology and Surgery*, vol. 2, pp. 317–325, 2008.

[45] Corral, G., Ibáñez, L., Nguyen, C., Stoianovici, D., Navab, N. and Cleary, K.R.: Robot control by fluoroscopic guidance for minimally invasive spine procedures. *International Congress Series*, vol. 1268, pp. 509 – 514, 2004.

[46] Cadeddu, J., Stoianovici, D., Chen, R., Moore, R. and Kavoussi, L.: Stereotactic mechanical percutaneous renal access. *Journal of Endourology*, vol. 12, no. 2, pp. 121 – 125, 1998.

[47] Vikal, S., U-Thainual, P., Carrino, J.A., Iordachita, I., Fischer, G.S. and Fichtinger, G.: Percutaneous surgery training and performance measurement platform. *Computerized Medical Imaging and Graphics*, vol. 34, no. 1, pp. 19 – 32, 2010.

[48] Wood, N.A., Shahrour, K., Ost, M.C. and Riviere, C.N.: Needle steering system using duty-cycled rotation for percutaneous kidney access. *The Journal of Urology*, vol. 185, no. 4, p. 376, 2010.

[49] Hartley, R. and Zisserman, A.: *Multiple View Geometry in Computer Vision, second edition.* Cambridge University Press, 2003.

[50] Chintalapani, G., Jain, A. and Taylor, R.: Statistical characterization of C-arm distortion with application to intra-operative distortion correction. *Medical Imaging 2007: Visualization and Image-Guided Procedures*, vol. 6509, 2007.

[51] Van der Merwe, W.: *Rapid 3D Measurement Using Digital Video Cameras.* Master's thesis, Stellenbosch University.

[52] Kucuk, S. and Bingul, Z.: Comparative study of performance indices for fundamental robot manipulators. *Robotics and Autonomous Systems*, vol. 54, no. 7, pp. 567 – 573, 2006.

[53] M.W. Spong, S. Hutchinson, M.V.: *Robot Modeling and Control.* John Wiley and Sons, Inc, 2006.

[54] Schreve, K.: *pyMulticam User Guide.* Stellenbosch University, 2011. Internal Report.

[55] Broers, H., Hemken, H., Luhmann, T. and Ritschl, P.: Photogrammetric calibration of a C-arm X-ray system as a verification tool for orthopaedic navigation systems. *ISPRS Journal of Photogrammetry and Remote Sensing*, vol. 56, 2002.